Demagnifying X-Ray Lithography

Von der Fakultät für Mathematik, Informatik und Naturwissenschaften der Rheinisch-Westfälischen Technischen Hochschule Aachen zur Erlangung des akademischen Grades einer Doktorin der Naturwissenschaften genehmigte Dissertation

vorgelegt von

Diplom-Physikerin Christiane Zimprich
aus Schwalmstadt.

Berichter: Universitätsprofessor Dr. B. Lengeler
Universitätsprofessor Dr. H. Lüth

Tag der mündlichen Prüfung: 25. April 2003

Contents

Chapter 1

Introduction

In the past decades, a rapidly proceeding miniaturization and integration of electronic circuits has accompanied the spreading of computers and electronic control systems in our world. In the course of this development, the interest in the fabrication of mechanical and optical devices in the micrometer-range, so-called MOEMS (microoptoelectromechanical systems), has also been growing in recent years. The sensors for air bags and antilock braking systems are only two of many examples that illustrate the importance of these systems in the modern world.

The ongoing miniaturization demands a decrease in the minimum feature sizes that can be fabricated. Figure 1.1 shows a roadmap for the development of the transistor gate lengths in microelectronics. With this decrease of the feature size, the demand grows for further developments in lithography. In optical lithography, this development is leading to a decrease in the wavelength from around 400 nm over 193 nm nowadays to the extreme ultraviolet with 13.4 nm in the future to provide a resolution that is high enough to image the decreasing features. The wavelengths can also be reduced even further to soft x-rays with about 1 nm and below. The use of harder x-rays is of interest especially for micromachining applications, since the long absorption lengths at these energies allows the structuring of very thick resist layers with thicknesses up to 1 mm.

A critical point in lithography is the fabrication of masks, since the features on the mask have to shrink in accordance with the features on the final sample. The use of demagnifying lens systems has been a standard tool for optical lithography for several years. This is an advantage for the mask productions, since the mask features are allowed to be larger than the resulting features on the specimen.

With decreasing wavelength of the light, however, the standard optical systems for the visible and ultraviolet regime cease to function. Equivalent optics for x-rays, however, have not been available for a long time, and it has been common knowledge since the times of W. C. Röntgen that refractive lenses do not work

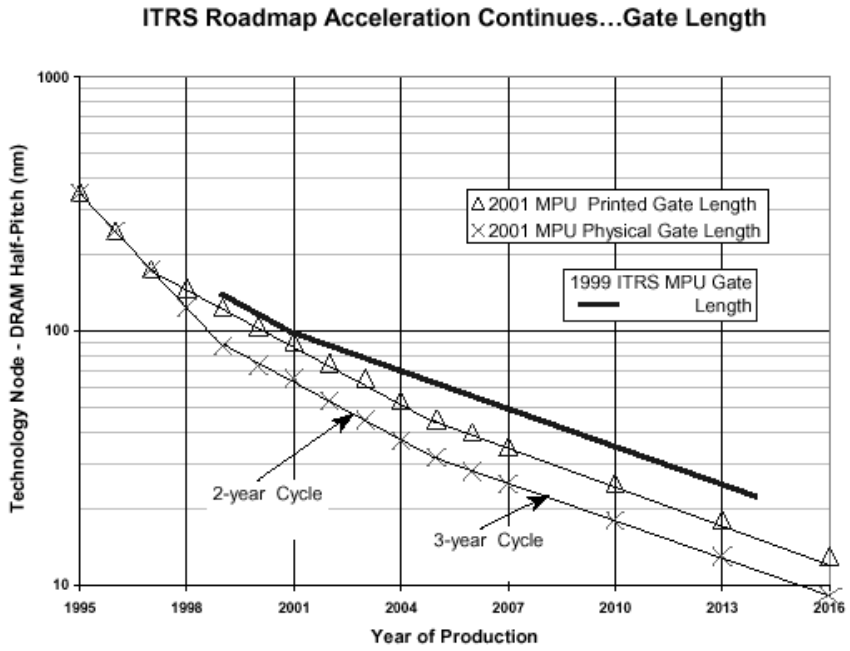

Figure 1.1: Development of the printed gate lengths for transistors from the 2001 international roadmap for semiconductors [1].

for x-rays [2]. Indeed, the refraction of x-rays in matter is a very weak effect. Nevertheless, A. Snigirev et al. [3] could demonstrate in 1996 the working of the first refractive lenses for hard x-rays. The lenses consisting of aligned and crossed drill holes are able to focus x-rays, but due to their cylindrical shape they have a strong spherical aberration, which limits their use for imaging applications. This problem can be overcome with parabolic refractive x-ray lenses (PRXL), which were first used in 1998 [4]. These lenses have since been used as optics for a wide variety of tasks in microscopy and microtomography [4–10] for hard x-rays between 8 and 100 keV.

The aim of this thesis is to show that the PRXL can be used as a demagnification tool in lithography with hard x-rays. In chapter 2, the generation of synchrotron radiation will be discussed briefly together with the basic concepts of its interaction with matter. A description of PRXL and their imaging characteristics follows in chapter 3. Chapter 4 gives a short introduction into lithography. This chapter will not only deal with x-ray but also with optical and electron-beam lithography. Another focus will be the resist technology, which is similar for all lithographic processes. The fabrication of the masks that are used in the x-ray lithography experiments will be described in chapter 5. In chapter 6, the experimental setup and the results of the demagnifying x-ray lithography experiments

are presented. The difficulties that arise in these experiments due to secondary electrons are further investigated by means of Monte Carlo simulations in chapter 7. Some improvements for the demagnifying x-ray lithography will be discussed in chapter 8.

Chapter 2

Synchrotron Radiation: Generation and Interaction with Matter

The basic concept of a synchrotron was developed to accelerate charged particles such as electrons. A magnetic field keeps the particles on a circular orbit during the acceleration process. This field is changed synchronously with the increasing particle energy so that the radius of the orbit is kept constant. A drawback of these accelerators is, however, that electrons with high energies lose a large amount of their energy in form of radiation when moving on a circular path. This effect limits the maximum energy that can be attained. But the radiation has been used for various experiments since shortly after its discovery. These synchrotron radiation sources of the first generation were mainly dedicated to high energy physics and only partially used for experiments with synchrotron radiation. The sources of the second generation were accelerators, which were exclusively used for the generation of x-rays, since they were no longer needed for high energy physics. Modern synchrotron radiation sources of the third generation, which are optimized in design for the generation of x-rays, however, are storage rings for highly relativistic electrons, which are accelerated in separate booster synchrotrons. These electrons emit x-rays due to their circular motion in the bending magnets and due to their oscillating path in the insertion devices, which are used for a wide variety of tasks, e.g. in material analysis.

In the first part of this chapter, the generation of x-rays at a synchrotron radiation source is described. The second part deals with the interactions of x-rays with matter.

Figure 2.1: Overview of the ESRF in Grenoble, France: The beamlines marked with BM are bending magnets; the ones labeled ID are insertion devices like undulators [11].

2.1 Generation of X-Rays

The experiments described in the later chapters were performed at the European Synchrotron Radiation Facility (ESRF) in Grenoble, France. This is a third generation synchrotron radiation source that provides hard x-rays with high intensity.

Figure 2.1 shows an overview over the accelerators and the storage ring at the ESRF. The electrons are injected from a linear accelerator into the booster syn-

chrotron with an energy of about 200 MeV. Within the booster synchrotron, they are further accelerated, until they reach their final energy of 6 GeV, before they are injected into the storage ring. Additional acceleration within the storage ring is used only to keep the electrons at a constant energy over several hours.

The storage ring is a polygon, which, at the ESRF, consists of 32 segments and has a circumference of 845 meters. At the corners of the polygon are the so-called bending magnets. They provide a homogenous magnetic dipole field perpendicular to the path of the electrons, which results in a change of the direction of this path. Additional magnets with more complicated forms are used to keep the electron beam focused. Due to the acceleration that accompanies their change in direction, the electrons emit radiation, which is used in experiments. In figure 2.1, the beamlines that are located directly at the bending magnets are marked BM.

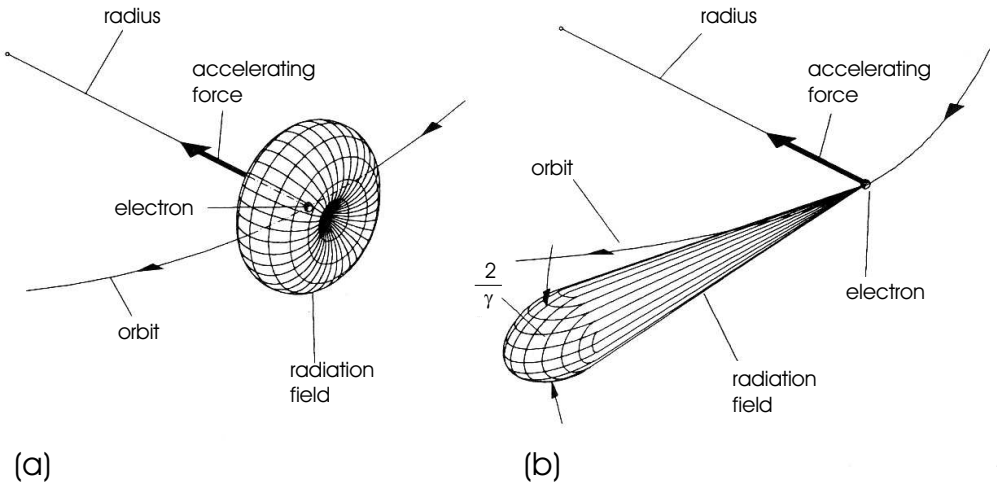

Figure 2.2: The radiation field of an electron on a circular orbit: (a) slow electron ($v \ll c$) and (b) relativistic electron [12]

In general, the radiation of an electron on a circular orbit is the same as the one of the Hertz dipole (cf. figure 2.2(a)). However, since the electrons in a synchrotron are highly relativistic, i. e., their velocity is very close to the speed of light, the radiation appears as a sharply collimated beam tangential to the electron path, as can be seen in figure 2.2(b). The beam divergence angle is proportional to $\frac{1}{\gamma}$ with $\gamma = \sqrt{1-\beta^2}^{-1}$ and $\beta = \frac{v}{c}$. For the ESRF the corresponding values are $\beta = 1 - 7.11 \cdot 10^{-9}$ and $\gamma = 11859$.

The straight segments between the bending magnets are used for insertion de-

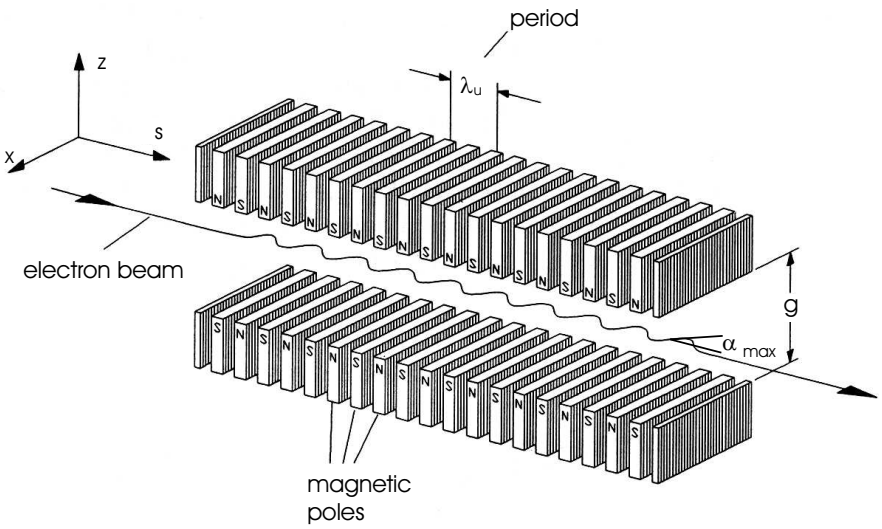

Figure 2.3: Schematic drawing of an undulator [12]

vices, i. e. wigglers or undulators. In figure 2.1, the beamlines which apply insertion devices are labeled ID. Figure 2.3 shows the concept of an undulator: It consists of two rows of magnets facing each other, which create a periodic magnetic field and force the electrons onto an oscillating path. Wigglers are built in the same manner. The difference between these two devices is that for the undulator the angle of the electron path ($\alpha_{\max}$ in figure 2.3) is smaller than $1/\gamma$, while for the wiggler it is larger than $1/\gamma$. This leads to fundamental differences in the emission between wiggler and undulator: The wiggler, like the bending magnet, has a continuous spectrum. The undulator, on the other hand, has a discrete spectrum. The reason for this is the fact that the different cones of radiation, which result from each oscillation of the electron's path, overlap and superpose coherently. The energies of the undulator spectrum are integer multiples of a basic energy, which depends on the period and the strength of the magnetic field, and are called the harmonics of the undulator. To tune the undulator, the gap between the magnetic poles and, thus, the strength of the magnetic field is changed. The emission of a highly collimated beam with a very small energy band and a high intensity is the main advantage of an undulator.

One parameter that describes an x-ray source is the photon flux F, i. e. the number of photons per second in a given bandwidth of 0.1%. Another one is the brilliance, which further takes into account the horizontal and vertical beam sizes σ_x, σ_y and beam divergences σ'_x,σ'_z:

$$B = \frac{F}{4\pi^2 \sigma_x \sigma_z \sigma'_x \sigma'_z} = \frac{\text{photons}}{\text{s } 0.1\%\text{BW mm}^2 \text{ mrad}^2} \tag{2.1}$$

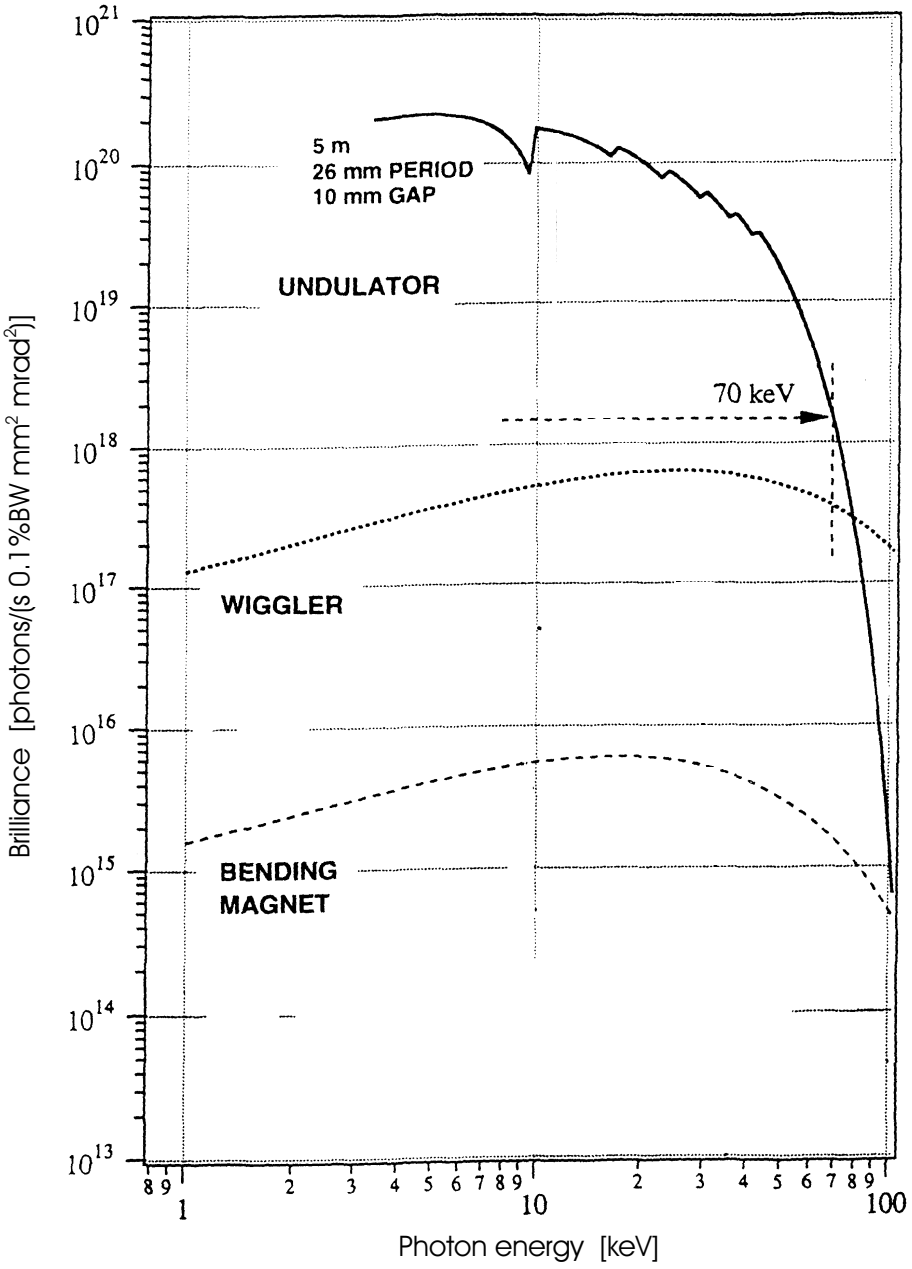

Figure 2.4: Brilliance of bending magnets, wigglers, and undulators at the ESRF [13]

Figure 2.4 shows a comparison of the brilliances for the different x-ray sources described above. The brilliance of an undulator is several orders of magnitude higher than that of a wiggler or of a bending magnet.

In general, not the full undulator spectrum (the so-called white beam) is used for experiments but a setup, where mirrors and absorbers are used to cut off the lower and higher harmonics of the spectrum, respectively (the so-called pink beam), or a monochromator is used to single out one narrow energy band by means of Bragg reflection on crystals.

In the experiments described later on, a palladium-coated silicon mirror and a palladium filter were used to generate a pink beam. Alternatively, a double-crystal fixed-exit Si-111 monochromator was applied. The pink beam setup has a broader energy band ($\Delta E/E \sim 10^{-2}$) than the monochromator ($\Delta E/E \sim 10^{-4}$) and a higher flux ($I_{pink} \sim 10 - 100 \times I_{mono}$) [14]. Thus, a pink beam is of interest for applications that require a high photon flux but can do without a high energy resolution, while a monochromatic beam has a high resolution at the cost of a reduction of the flux.

2.2 Interaction with Matter

The interactions of x-rays with matter are important for the understanding of the x-ray lithographic process as well as of functionality of the parabolic refractive x-ray lenses.

2.2.1 Absorption

When x-rays pass through matter, they are attenuated. This behavior is described by Lambert-Beer's law:

$$I(x) = I_0 \exp(-\mu x) \tag{2.2}$$

Here, I_0 is the intensity before the sample, and $I(x)$ is the remaining intensity after a homogeneous slice of material of the thickness x.

The linear absorption coefficient μ contains contributions from photoabsorption (τ), elastic scattering (σ_R, Raleigh scattering), inelastic scattering (σ_C, Compton scattering), and pair production (σ_{pair}) for x-rays above 1.022 MeV:

$$\mu = \tau + \sigma_R + \sigma_C(+\sigma_{pair}) \tag{2.3}$$

Values for the mass absorption coefficient μ/ρ, where ρ is the density, can be found in the literature for almost all elements and for a wide range of x-ray energies [15].

For compound materials, the mass absorption coefficients of the elements are weighted with the relative density

$$\rho_i = \rho \cdot \frac{\nu_i A_i}{\sum_j \nu_j A_j}, \tag{2.4}$$

where ν_i is the number of atoms and A_i the atomic weight of the component i. Thus, the linear absorption coefficient of a compound is

$$\mu = \sum_i \left(\frac{\mu}{\rho}\right)_i \rho_i. \tag{2.5}$$

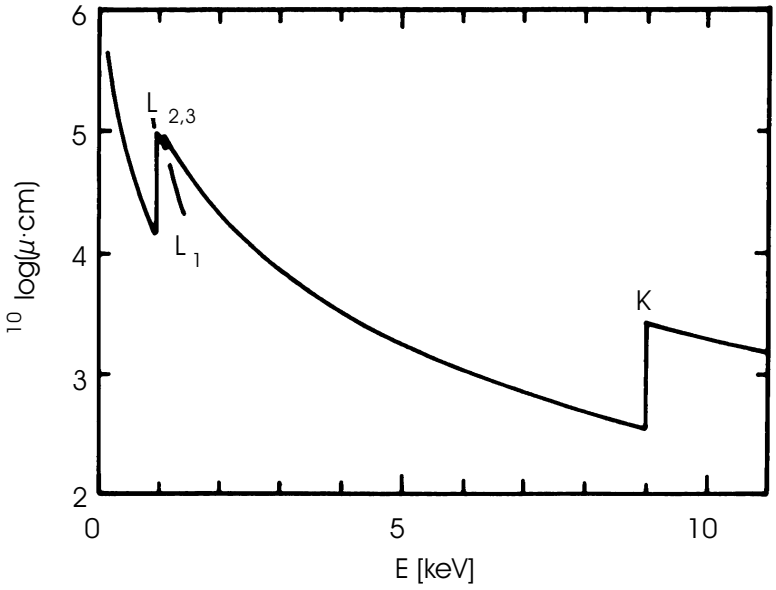

Figure 2.5: Linear absorption coefficient of copper versus photon energy, by courtesy of B. Lengeler

The absorption coefficient changes with the photon energy. In general, the attenuation decreases with increasing energy. However, at the binding energies of the electrons a jump, a so-called absorption edge, appears due to the onset of

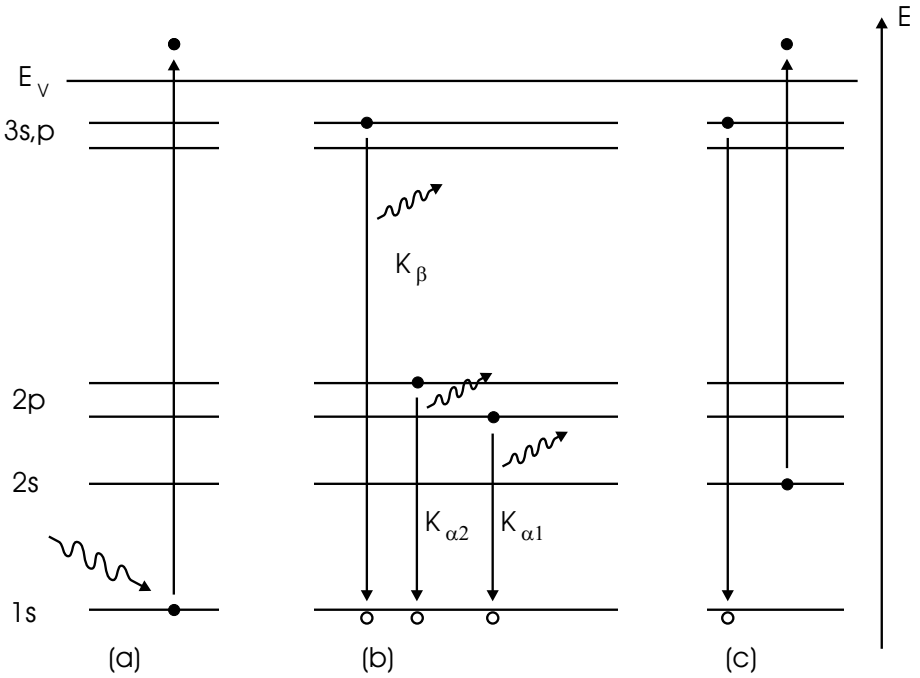

Figure 2.6: X-ray absorption with the creation of a photoelectron (a) and the two possible secondary processes: fluorescence (b) and emission of an Auger electron (c)

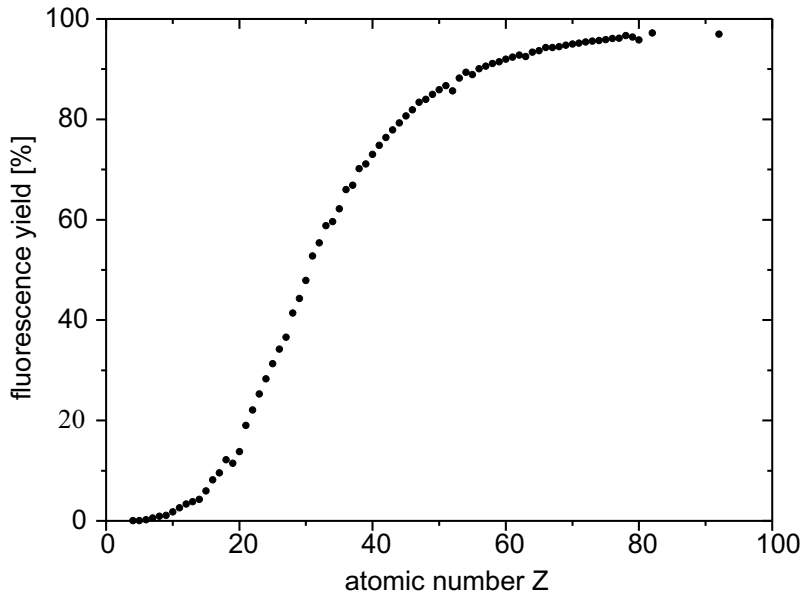

Figure 2.7: Fluorescence yield for the K_α-line versus the atomic number Z [16]

photoabsorption of the respective atomic shell. In figure 2.5, these absorption edges are depicted for the copper K and L shells.

In the absorption process, an electron is released from the atom as photoelectron (cf. fig. 2.6(a)). Photoabsorption is strongest for tightly bound inner electrons. On the other hand, absorption by the outer shell electrons is weak, since they are not bound strongly enough to the nucleus for it to take on the surplus momentum of the photon.The kinetic energy of the photoelectron is the difference between the incident photon energy and the binding energy of the atom's shell.

The hole in the inner shell is then filled by an electron from an outer shell. The surplus energy of this process is either transferred to a fluorescence photon (cf. fig. 2.6(b)) or to an Auger electron (cf. fig. 2.6(c)). The probability of the two competing processes depends on the element in which it occurs. Figure 2.7 shows the yield for the K_α fluorescence versus the atomic number Z. The fluorescence yield increases with increasing atomic number, while the yield for Auger electrons decreases accordingly.

2.2.2 Refractive Index

The refractive index for x-rays can be written as [17]

$$n = 1 - \delta + i\beta, \tag{2.6}$$

where δ describes the refraction; the imaginary part β describes the absorption and is connected to the photoabsorption τ via $\tau = \frac{4\pi}{\lambda}\beta$, where λ is the wavelength of the photons.

Both δ and β can be calculated from the atomic scattering factor $f(\vec{K} = 0) = Z + f' + if''$ in forward direction, where Z is the atomic number and $f' + if''$ is the dispersion correction:

$$\delta = C \cdot (Z + f') \tag{2.7}$$

$$\beta = C \cdot f'' \tag{2.8}$$

$$\text{with} \quad C = \frac{N_a}{2\pi} r_0 \lambda^2 \rho \frac{1}{A} \tag{2.9}$$

For compound materials, δ and β are also calculated via the relative density (eq. 2.4). Thus, δ can be written as

$$\begin{aligned} \delta &= \sum_i \frac{N_A r_0 \lambda^2}{2\pi} \frac{Z_i}{A_i} \rho_i \\ &= \frac{N_A r_0 \lambda^2 \rho}{2\pi} \frac{\sum_i \nu_i Z_i}{\sum_j \nu_j A_j} \end{aligned} \tag{2.10}$$

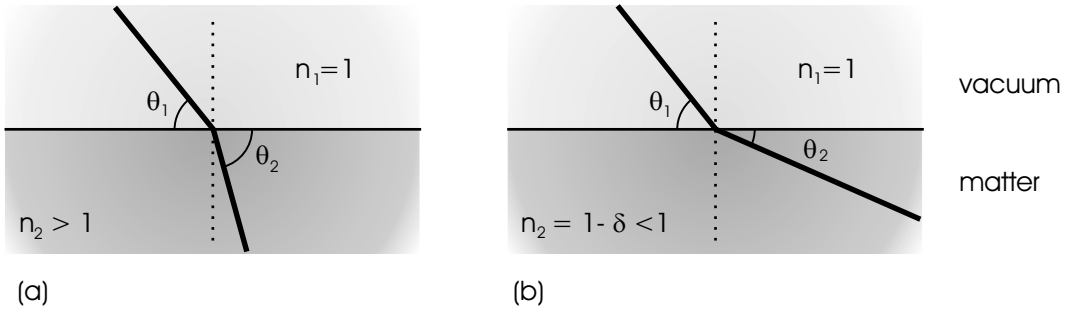

Figure 2.8: Refraction for (a) visible light and for (b) x-rays. The angle difference $(\theta_1 - \theta_2)$ in (b) is highly exaggerated [18].

away from the absorption edges. Similarly, β or τ can be written as

$$\begin{aligned} \tau = \frac{4\pi}{\lambda}\beta &= \frac{4\pi}{\lambda}\sum_i \frac{N_A r_0 \lambda^2}{2\pi}\frac{f_i''}{A_i}\rho_i \\ &= \sum_i \left(\frac{\tau}{\rho}\right)_i \rho_i. \end{aligned} \tag{2.11}$$

The refractive index for x-rays deviates only very little from 1, since both δ and β are very small. δ is of the order of 10^{-6} for most materials at photon energies around 10 keV; β is even smaller by two or three orders of magnitude. Hence, the refraction is only very small. Since δ is positive, the real part of the refractive index n is smaller than 1. Thus, according to Snell's law [19]

$$n_1 \cos(\theta_1) = n_2 \cos(\theta_2), \tag{2.12}$$

the x-rays that pass from vacuum (or air) into matter are refracted away from the surface normal (cf. fig. 2.8(b)). For visible light, the refraction is towards the surface normal (cf. fig. 2.8(a)), since n_2 is larger than 1.

For angles θ_1 in figure 2.8(b), which are smaller than a certain critical angle θ_c, the x-rays are reflected completely from the sample surface. According to equation 2.12, the critical angle θ_c can be calculated from

$$\begin{aligned} \cos(\theta_c) = n_2 &\rightarrow 1 - \frac{\theta_c^2}{2} \cong 1 - \delta \\ &\rightarrow \theta_c^2 \cong \sqrt{2\delta}. \end{aligned} \tag{2.13}$$

Above the critical angle θ_c, a part of the radiation is transmitted. For increasing angles θ_1, the part of the incoming x-rays that is reflected diminishes rapidly. Due to this external total reflection, mirror for x-rays work with grazing incidence. As δ decreases with increasing energy, the reflection can serve as a low-pass filter.

Chapter 3

Imaging with Parabolic Refractive X-Ray Lenses

The refraction of x-rays in matter has already been discussed in section 2.2.2. On this basis, refractive lenses for x-rays can be constructed in an analogous manner to the well-known glass lenses for visible light. The focal length f for both cases can be described by the lens maker's formula

$$\frac{1}{f} = \frac{2(n-1)}{R}, \tag{3.1}$$

where n is the real part of the refractive index and R is the radius of curvature of the lens. However, some differences have to be noticed:

First, the refractive index for x-rays in matter is smaller than 1, as can be seen from equation 2.6. Thus, a focussing lens has to be concave for x-rays, while it is convex for visible light.

Second, since δ in equation 2.6 is very small, the refractive index is close to 1. Thus, as can be seen from equation 3.1, the radius of curvature of an x-ray lens has to be very small to achieve a manageable focal length. The radius of curvature, however, can not be reduced to any size, since this means also a reduction of the aperture of the lens. As a solution, the focal length can be reduced by using a system of several lenses with the individual focal lengths f_i. As long as the focal length of such a system is still long compared to the thickness of the stack, the system can be treated as a thin lens and the focal length can be calculated as

$$\frac{1}{f} = \sum_i \frac{1}{f_i}. \tag{3.2}$$

Thus, for N identical lenses, where each has two surfaces with radius R, the focal length is

$$f = \frac{R}{2N\delta}, \tag{3.3}$$

where δ is the refractive index decrement (cf. eq. 2.6).

Third, the absorption of x-rays is significant in all materials. To reduce attenuation in the lens to a minimum, materials with a low atomic number Z are necessary [20]. Further criteria for the choice of the lens material are its machinability, a low small angle scattering and its stability in an x-ray beam of high energy and intensity.

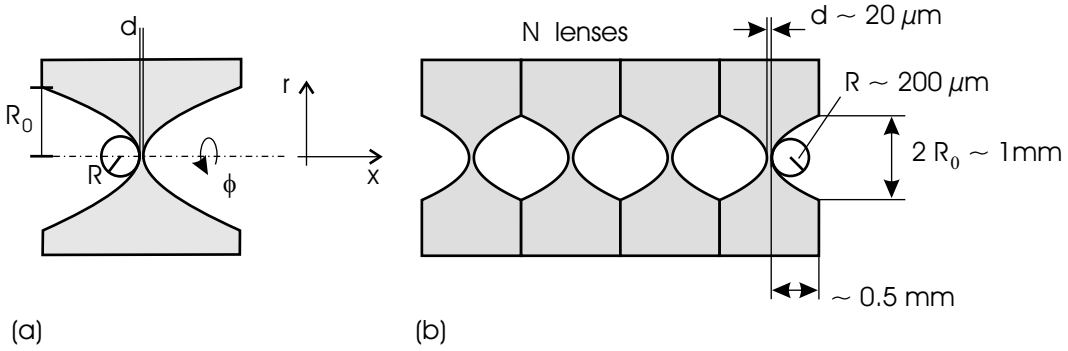

Figure 3.1: Sketches of a single parabolic refractive x-ray lens (a) and a stack of lenses (b) [6]

Fourth, due to the strong curvature of the lenses, i. e., the radius of curvature R is small compared to the geometrical aperture $2R_0$, the spherical aberration of an x-ray lens is rather high. This effect can be avoided by giving the lenses a parabolic shape [4, 6], as is shown in figure 3.1(a). In the notation of this figure, the shape of the lens can be written as

$$x = \frac{r^2}{2R}. \tag{3.4}$$

The first working parabolic refractive x-ray lenses (PRXL) were made from aluminium [4–6]. They are made of thin aluminium slices with 1 mm diameter in a bronze ring with an outer diameter of 12 mm. The aluminium is coined into a concave parabolic shape from both sides. The single lenses are then aligned by stacking the coins behind each other on two polished shafts and fixed in their position with a spring sheet. The precision of the shafts is essential for the alignment of the the single lenses and, thus, for the quality of the PRXL. A complete PRXL can be seen in figure 3.2.

These lenses work well for imaging applications [4, 5, 7, 8]. Some of the imaging characteristics of the PRXL will be described in the following.

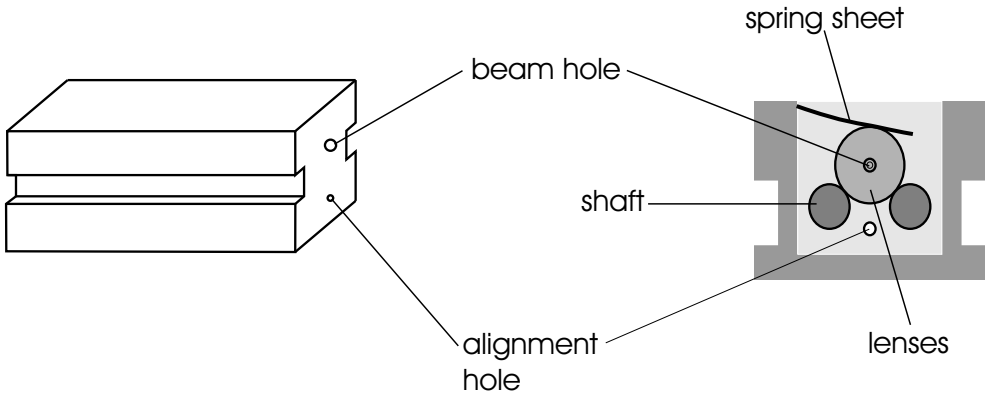

Figure 3.2: Picture of a complete PRXL (left) and its cross-section(right) [21]

3.1 Imaging Geometry

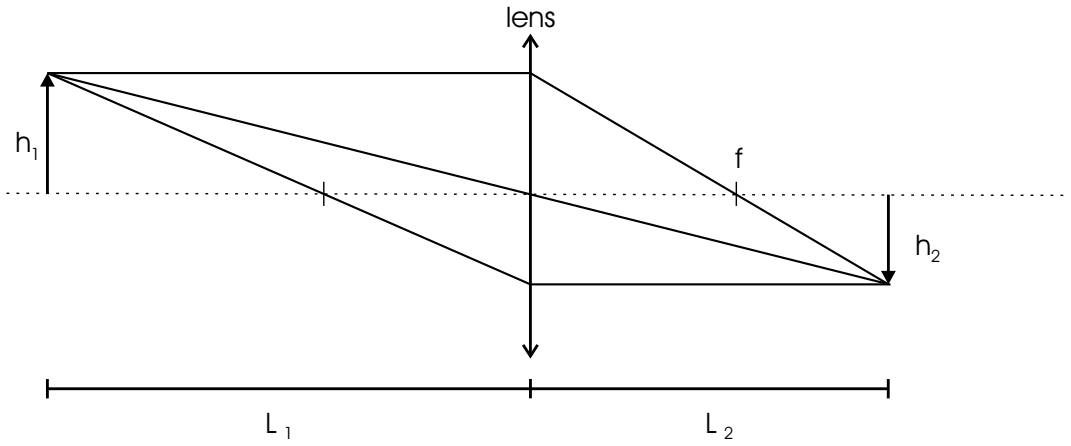

Figure 3.3: Imaging with a PRXL with a demagnifying geometry

The imaging of objects with the PRXL follows the rules of geometrical optics, as they are known for visible light, as it is depicted in figure 3.3. It is described with the Gaussian lens formula

$$\frac{1}{f} = \frac{1}{L_1} + \frac{1}{L_2}, \tag{3.5}$$

where f is the focal distance, L_1 the object distance, and L_2 the image distance.

With given f and L_1 the distance L_2, at which the sharp image appears, can be calculated from equation 3.5 to

$$L_2 = \frac{fL_1}{L_1 - f}. \tag{3.6}$$

The magnification or demagnification factor of the lens can be written as

$$m = \frac{L_2}{L_1} = \frac{h_2}{h_1}, \tag{3.7}$$

where h_1 and h_2 are the object and the image size, respectively. Thus, the size of the image is

$$h_2 = \frac{L_2}{L_1} h_1. \tag{3.8}$$

By a proper choice of L_1 with respect to the focal length f, the lens can be used to magnify or to demagnify.

3.2 Effective Aperture

The aperture of a glass lens for visible light is only limited by its size, since almost no light is absorbed in the lens. However, as has been discussed in chapter 2, the absorption of x-rays in matter can not be neglected, and thus, the transmission of an x-ray lens decreases for rays away from the optical axis, since it is concave and the thickness of the lens material that these rays have to pass through increases rapidly due to the very small radius of curvature.

For a PRXL with N single lenses, the effective aperture can be written as [6]

$$D_{\text{eff}} = 2\sqrt{\frac{2R}{\mu N}}, \tag{3.9}$$

provided that the geometric aperture is so large that the attenuation of the lens material dominates D_{eff}. This is the case for the aluminium lenses that are used in all experiments. Here, R is the radius of curvature of the parabola, and μ is the linear absorption coefficient of the lens material.

The effective aperture D_{eff} is usually smaller than the size of the lens. At a photon energy of 25 keV, for example, an aluminium PRXL with $N = 120$ single lenses and a parabola radius of 200 μm has an effective aperture of 164.5 μm, even though it has a diameter of 1 mm.

3.3 Numerical Aperture

Connected with the effective aperture D_{eff} is the concept of the numerical aperture $N.A.$. Photons that come from an object can only contribute to an image, if they pass through the effective aperture D_{eff} of the lens. As can be seen from figure

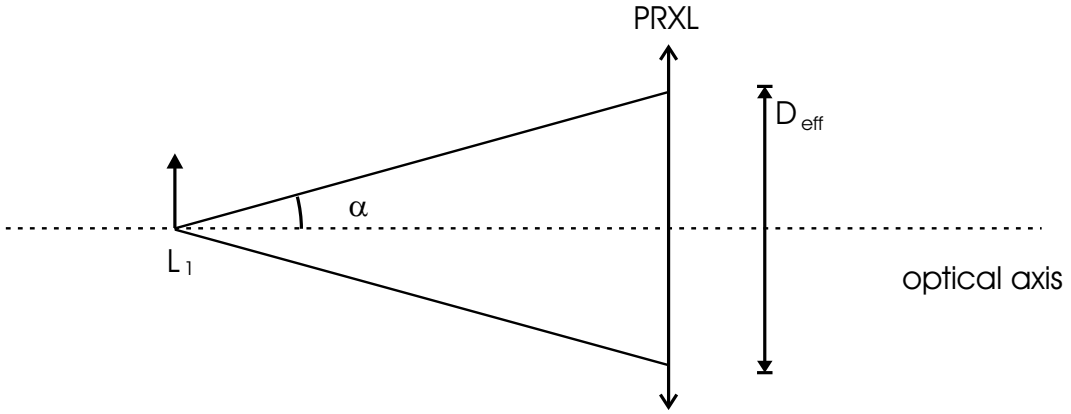

Figure 3.4: Definition of the numerical aperture of a lens

3.4, there is a maximum effective angle α that rays coming from the object at L_1 can have with the optical axis, so that they can still pass through the effective aperture of the lens. Rays with a larger angle would most likely be absorbed in the lens material. The numerical aperture $N.A.$ is defined as the sine of that maximum effective angle and can be written as

$$N.A. = \sin\alpha \approx \frac{D_{\text{eff}}}{2L_1} \text{ , for small angles } \alpha. \tag{3.10}$$

Since D_{eff} is of the order of about 100 μm for PRXL's and L_1 is in the meter range, the numerical aperture is very small ($\sim 10^{-4}$).

3.4 Diffraction Limited Spot Size

The small aperture of the x-ray lenses results in a widening of the focal spot due to diffraction, as it is depicted in figure 3.5. The full width at half maximum (FWHM) of the diffraction pattern can be written as [6]

$$B_{\text{diff}} = 2\sqrt{2\ln(2)}\frac{2L_2}{D_{\text{eff}}}\frac{1}{k}. \tag{3.11}$$

L_2 is the distance between lens and image, and $k = 2\pi/\lambda$ is the wave number of the x-rays. When the lens is used for focusing, the spot size can not become smaller than B_{diff}.

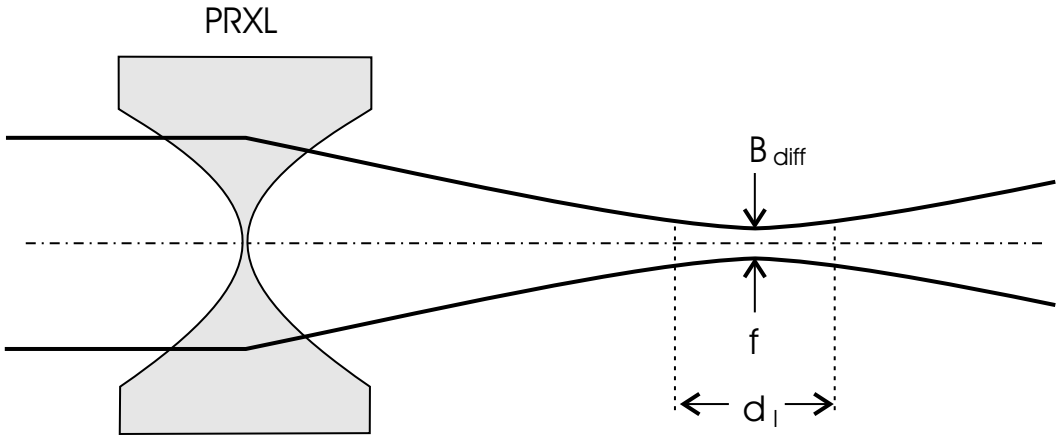

Figure 3.5: Diffraction limited spot size and depth of field [6]

3.4.1 Resolution

When the PRXL is used as an imaging device, the effective aperture D_{eff} of the lens limits the (transversal) resolution d_t, which can be described as the distance between two points of the imaged object, whose pictures are the FWHM B_{diff} of their diffraction patterns away from each other. According to equations 3.11 and 3.8, the resolution is [6]

$$d_t = 2\sqrt{2\ln(2)}\frac{2L_1}{kD_{\text{eff}}} = 2\sqrt{2\ln(2)}\frac{1}{k}\frac{1}{N.A.}. \tag{3.12}$$

The typical resolution of an aluminium PRXL is in the range of a few 100 nm.

3.4.2 Depth of Field

The depth of field d_l is defined as the distance along the optical axis, within which all objects are sharply imaged on the image plane L_2 behind the lens. It can be written as

$$d_l = \frac{8}{\pi}\lambda\frac{L_1^2}{D_{\text{eff}}^2} = 4\frac{1}{k}\frac{1}{(N.A.)^2}. \tag{3.13}$$

The typical depth of field of an aluminium PRXL is in the range of a couple of millimeters up to a few centimeters. Thus, a resist of corresponding thickness can be exposed, since the width of the features does not change between the top and the bottom of the resist.

3.5 Chromatic Aberration

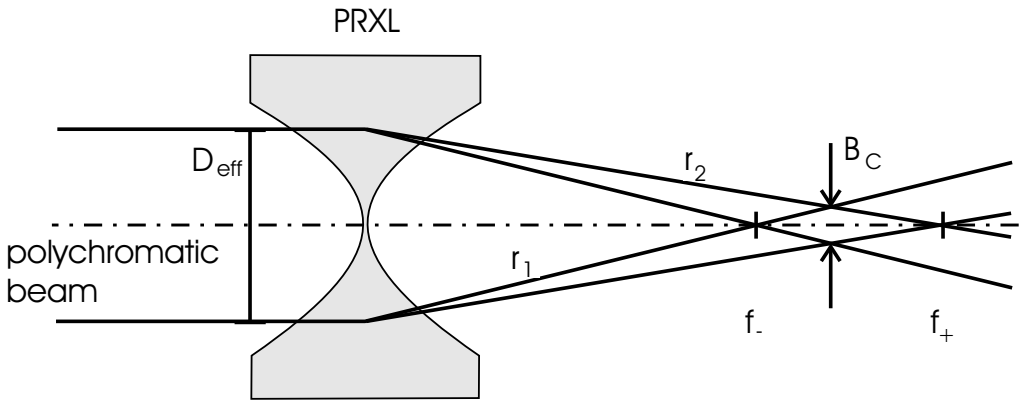

Figure 3.6: Chromatic aberration [6]

Since the focal length of a lens depends on the refractive index decrement δ (cf. eq. 3.3), which is energy dependent ($\delta \sim E^{-2}$), equation 3.5 is only fulfilled for one photon energy at given distances L_1 and L_2. This behavior is depicted in figure 3.6 for a parallel polychromatic beam, whose components focus in different points on the optical axis. The picture shows the rays for the minimum energy of the beam with the focus f_- and the maximum energy with the focus f_+, respectively.

The widening of the picture B_C can be determined geometrically from the intersection of the two lines r_1 and r_2 in figure 3.6, which correspond to the the energies $E + \Delta E$ and $E - \Delta E$, respectively. The result is:

$$B_C = D_{\text{eff}} - \frac{2D_{\text{eff}}}{f_-}\frac{f_- f_+}{f_- + f_+} \tag{3.14}$$

with $f_\pm = f \pm \Delta f$. Δf results from the energy dependence of the focal length ($f \sim E^2$ with $\Delta f/\Delta E = 2f/E$. With this equation 3.14 transforms into

$$B_C = D_{\text{eff}}\frac{\Delta E}{E}. \tag{3.15}$$

As was mentioned before, the energy bandwidth of monochromatic x-rays is $\Delta E/E \sim 10^{-4}$. For an effective aperture D_{eff} of 100 μm, this results in a chromatic aberration of about 0.01 μm, which can be neglected in comparison to other effects discussed here. For a pink beam with $\Delta E/E \sim 10^{-2}$, however, the chromatic aberration is about 1 μm and can influence the imaging behavior of the setup significantly.

Chapter 4

Lithography

A wide variety of lithographic techniques is used in modern microtechnology to create structures in the micrometer and sub-micrometer range. In this chapter, the basics of lithography and of the typical resists will be discussed together with some of the techniques. Apart from x-ray lithography — the technique this work is mainly focused on — optical and electron-beam lithography were used in the production of the x-ray masks.

4.1 Typical Process Outline

Independent of the specific technique, a lithographic process contains a number of typical steps, which will be outlined here.

In a first step, the sample is coated with a resist that is sensitive to the radiation used in the lithography. A dehydration bake of the sample on a hotplate prior to the coating enhances the adhesion of the resist on the substrate. After this, the sample is transferred to a spin-coater, where the liquid resist is spread homogeneously onto the surface. The thickness of the layer depends on the viscosity of the liquid and on the rotary frequency of the sample. Some substrate materials require an additional coating step with an adhesion promoting substance like hexamethyldisilazane (HMDS) prior to the actual resist coating. This layer of only a few nanometers thickness ensures a homogeneous resist layer with good adhesion on oxide layers. The resist is finally baked on a hotplate or in an oven to drive out all remaining solvent.

It is common to remove the resist on the rim of the substrate, since the coating is very sensitive to mechanical forces, e. g. due to wafer handling. Thus, fragments of the resist that break away under the substrate holders bear a risk of sticking

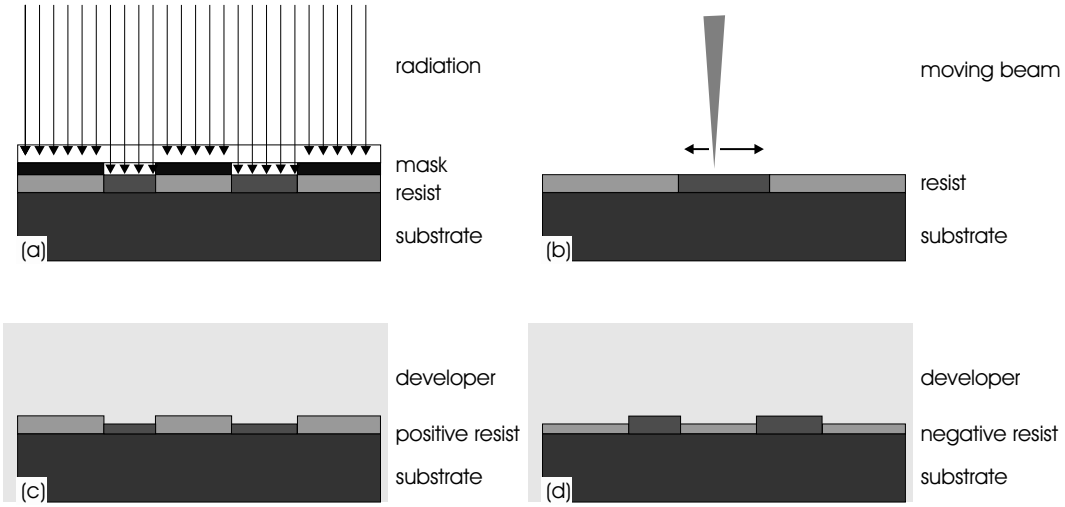

Figure 4.1: (a) Exposure with mask and UV light for example, (b) lithographic exposure by a moving beam, e. g. of electrons, (c) development of a positive tone resist, and (d) development of a negative tone resist

to the sample surface and, thus, impairing the quality of the features during the following processing steps.

The second step is the exposure of the resist (the actual lithographic step). Here, the structure is defined in the resist. This can be done either by a mask shadowing some areas of the resist from the radiation (cf. fig. 4.1(a)) or by a beam moving only over selected parts of the resist (cf. fig. 4.1(b)). Great care has to be put into the adjustment of the features in respect to structures already processed on the sample and into the choice of the proper exposure dose.

Radiation is able to change the state of the polymers forming the resist and by this changes the solubility of it in some organic solvents [22]. The reactions appearing in the exposure are mainly chain-scission, cross-linking or the modification of side-groups. Chain-scission, the cutting of polymer chains into shorter pieces, increases the solubility so that a diluted solvent, which would hardly attack the uncut polymers, can wash away the fragments and by this develop a positive structure. Cross-linking on the other hand leads to the building of larger and entangled polymer structures that are more resistant to a solvent and, thus, form a negative mask.

Development in a suitable solvent is the third and final step in creating the resist patterns. For a positive tone resist, this means that the exposed areas of the resist are washed away, while in a negative process the unexposed areas are taken away. Especially negative tone resists often require a post-exposure bake prior to the development, which enhances the cross-linking process. A last baking step

may sometimes be necessary to enhance the robustness of the resist mask against further processing steps.

4.2 Lithographic Resists

Lithographic resists are polymers, whose parameters can be altered by radiation in such a way that their solubility is either increased or decreased. The exact procedure depends on the specific polymers and on the radiation.

4.2.1 Sensitivity and Contrast

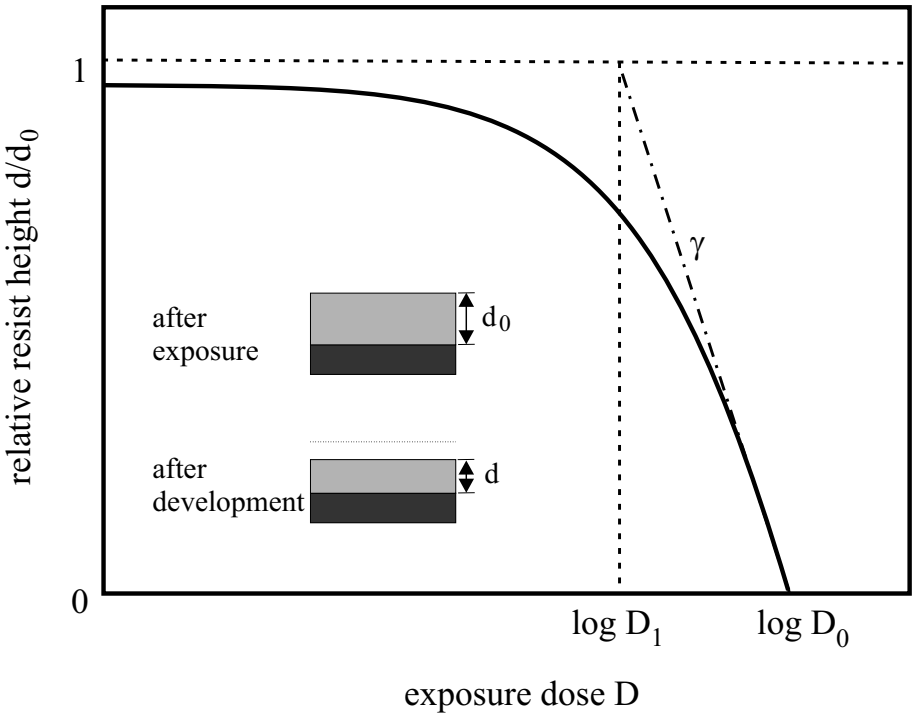

Figure 4.2: Resist height after development versus exposure dose for a positive tone resist. The exposure dose is plotted on a logarithmic scale. The dose D_0 describes the resist sensitivity; the slope γ is the contrast [23].

Two parameters that describe the behavior of a resist are the sensitivity and the contrast. Their meaning is shown in figure 4.2 for a positive tone resist. Here, the resist height that remains after development is plotted in dependence of the dose, which was used to expose the resist. For very low doses, the resist is hardly attacked by the developer. However, since the typical developer is a diluted

solvent for the resist, the unexposed areas are not completely untouched. With increasing dose, the amount of resist removed during the development grows, since the solubility of the resist is increased, too. In an idealized resist, the dose for which this behavior starts to occur would be D_1. Finally, for doses higher than D_0, the resist is completely removed. The characteristics of this curve are very sensitive to the various parameters of the development process, which therefore have to be controlled very carefully.

The resist sensitivity is the minimum dose D_0, which is needed to fully expose the resist so that it is removed completely in the developer. The higher the sensitivity is, i. e. the lower the dose D_0, the shorter is the time that it takes to expose a given structure. Thus, a high sensitivity resist is important to achieve a high throughput.

The contrast is defined as the slope γ of the curve near the dose D_0 (the dash-dotted line in figure 4.2). It can be written in the form [23]

$$\gamma = [\log(D_0/D_1)]^{-1}. \tag{4.1}$$

The contrast describes the ability of a resist-developer system to distinguish between small differences in the exposure dose at adjacent points on a sample. A high contrast offers a higher range in the process parameters and leads to steeper edges in the resist structures. This is especially important for dense patterns and small features.

For a negative resist, the resist height increases with increasing dose between D_1 and D_0, since the unexposed resist is removed in the developer, but contrast and sensitivity are defined in a similar manner.

Both sensitivity and contrast vary with the different parameters of the development process, like temperature, concentration of the developer, or the temperature of the pre- and post-exposure bakes. However, a change in one of these parameters will not necessarily be beneficial for both of them [23].

4.2.2 Polymers

A lithographic resist typically is a polymer, whose solubility in a specific solvent can be altered by radiation. According to what was discussed before, a lithographic resist should offer both a high sensitivity and a high contrast. It also should be easy in handling and robust against further processing like dry etching.

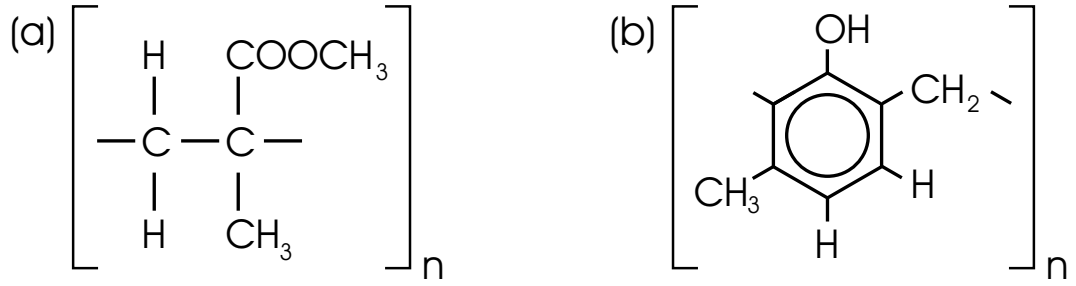

Figure 4.3: Examples of polymers commonly used as resists: (a) repeat unit of poly(methyl methacrylate) (PMMA), (b) repeat unit of a novolac-resin with a benzene ring

PMMA

A typical example for a polymer, which is often used in electron-beam or x-ray lithography, is poly(methyl methacrylate) (PMMA), whose repeat unit is shown in figure 4.3(a). Even though the sensitivity is rather poor, PMMA is in use in a wide range of applications, since it shows the highest resolution among organic resists with a linewidth down to somewhere between 5 and 7 nm [24].

The exposure of PMMA is a positive process, where electrons induce a scission of the molecular chains. This leads to a higher solubility of the resist pattern in some organic solvents. A very common developer is methyl isobutyl ketone. To control the development speed it is usually diluted in isopropyl alcohol, which does not noticeably attack PMMA.

To achieve a high uniformity in the resist performance, only polymers of specific average molecular weight are used in a resist layer, since chains of approximately the same length need similar doses to be exposed completely. The molecular weight has great influence on the performance of the resist, its sensitivity and contrast. A high molecular weight typically leads to a low sensitivity but also to an increase in contrast and resolution [25].

PMMA is also used in the fabrication of very thick lithographic structures up to several millimeters in height, which are usually made with x-ray lithography.

Novolac

Other polymers which are used very often are novolac-resins. An example of this group of polymers is shown in figure 4.3(b).

Novolac-based resists are usually multi-component. A concept that is common in optical lithography is the use of novolac as the layer forming component in combination with a photoactive substance like diazonaphthoquinone. The exposure with ultraviolet light converts the diazonaphthoquinone into a carboxyl acid, which can react with an alkaline developer. This reaction is the reason for the solving of the exposed resist during the development.

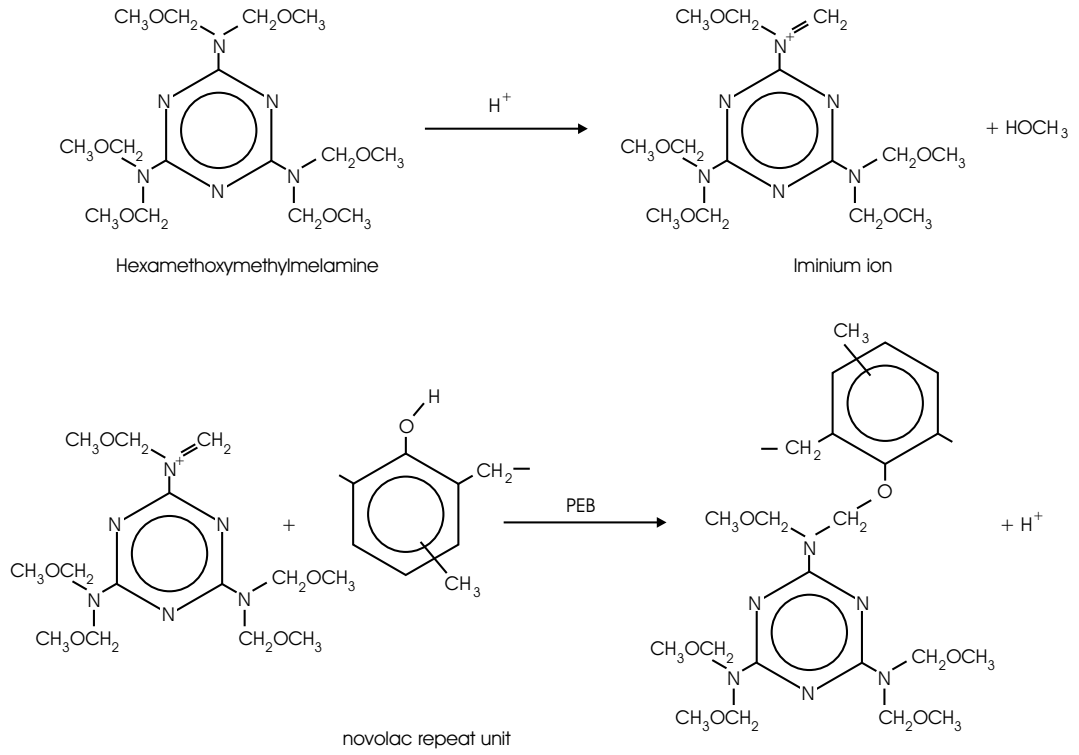

Figure 4.4: Reaction scheme for a negative, novolac-based resist. PEB means post-exposure bake [26].

When a novolac-based resist is used as a negative tone resist, a cross-linking agent is added. An example for this class of resists is the negative electron-beam resist AR-N 7700.18, which is used in the x-ray lithography experiments described later on. In addition to the novolac basis, this resist contains a modified novolac-resin, which acts as acid generator, and a cross-linking agent based on melamine.

The exposure creates a Brønsted acid, which is necessary to activate the cross-linking agent, so that it can react with the novolac during the post-exposure bake. P. M. Dentinger and J. W. Tayler [26] describe the reactions in a similar kind of resist in detail: The proton from the acid attacks one of the oxygens in the functional groups of the hexa(methoxymethyl)melamine (HMMM), producing methyl alcohol and leaving a iminium ion behind, as is shown in the upper part of figure 4.4. Since HMMM has six functional groups, it has a potential to link

several novolac polymers. During the post-exposure bake, this iminium ion reacts with the phenol group of a novolac unit creating a link. At the end of the reaction, another proton is released, which can induce another reaction. Thus, only a small amount of acid needs to be created by the exposure to induce a sufficient amount of cross-links in the resist. This explains the low doses needed for a full exposure in comparison to other resist families.

4.2.3 Handling

The most common method to apply a resist layer onto a substrate is by dissolving the polymers in an organic solvent and spreading them uniformly onto the substrate by means of a spin-coater. The thickness of the resist layer created that way depends on the rotary speed of the spin-coater and the solution rate of the polymers in the liquid. For standard layer thicknesses of up to a few micrometers, about 30 seconds are enough to let the resist dry to such an extent that the thickness remains stable when the spinning stops. Afterwards, the resist is baked on a hotplate or in an oven to drive out all the solvent left in the layer. Thick resist layers are often made of foils, which are glued onto the substrate. A third way to create a resist layer is to let the polymerization happen directly on the substrate. Development is typically done either by dipping the sample into the liquid developer or by continuously spraying it over the sample. Sometimes it is also done by using a plasma.

4.2.4 Proximity Effect

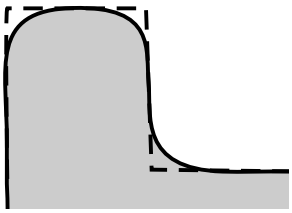

Figure 4.5: Sketch of the resist features (solid line) resulting from a uniformly exposed pattern (dashed line) due to proximity effect

The so-called proximity effect describes the observation that the dose deposited at a given point of the resist depends not only on the direct exposure there but also on the exposure of the neighboring areas. This results in the underexposure of outgoing corners and the overexposure of ingoing corners, respectively, as is drawn in figure 4.5. The influence is not only within the same structure but also between different structures with short distances in-between.

In electron-beam lithography, the reason for this effect mainly is the back-scattering of electrons from the substrate. To avoid it, the exposure dose is varied over the structure so that the resulting dose leads to the desired resist pattern [27].

In optical lithography, the proximity effect occurs due to diffraction. Here, the correction is usually done by changing the mask form [28], since the dose is uniform over the whole exposure area.

4.3 Lithographic Methods

A wide variety of types of radiation is in use for lithographic structuring. The method of choice for a given application depends on factors such as minimum feature size or resist thickness.

In order to fit into a process in microelectronics or micromachining, a method must meet a list of demands not only in respect of feature size and reproducibility. It must also be possible to align structures in respect to previous process steps with high accuracy. Further conditions for the application of a method in the industry are low cost and a high throughput, i. e., a large number of samples should be processed in a short time.

4.3.1 Optical Lithography

The term "optical lithography" is typically used for lithography with ultra-violet light. Depending on the wavelength a further separation is made into ultra-violet (UV, $\lambda \sim 300 - 450$ nm), deep ultra-violet (DUV, $\lambda \sim 153 - 250$ nm), and extreme UV (EUV, $\lambda \sim 13.4$ nm). The typical wavelength, which is used in the semiconductor industry nowadays, is 193 nm.

Optical lithography is a very fast and, for this reason, a rather cost-effective method. It is possible to expose a full 300 mm wafer in about 10 seconds. This allows a throughput of about 100 wafers in an hour [29].

Optical lithography systems use a mask, which is imaged onto the resist, as is depicted in figure 4.1(a). The so-called contact mode that is shown in this picture is very common due to its resolution, but bears the risk of contaminating or even damaging the mask due to the contact between mask and resist. The minimum feature size (MFS) in this method is given by

$$MFS = \sqrt{d \cdot \lambda}, \tag{4.2}$$

where d is the resist thickness and λ is the wavelength.

To avoid the problems described above, a small gap is often left between the mask and the resist. This mode is called the proximity mode. However, the resolution

is not as good as in the contact mode, since it is given by

$$MFS = \sqrt{(d+g)\cdot\lambda} \tag{4.3}$$

with g being the size of the gap between mask and resist.

A third option is the use of an imaging optic between mask and resist (projection mode). Since the shadow of the mask is no longer directly transferred into the resist, this method has a higher resolution than the proximity lithography by avoiding contact between mask and resist. This method can also create a reduced image of the mask so that patterns on the mask are allowed to be bigger than the feature size on the sample. In this mode, a wafer is typically not exposed in one step but with a so-called stepper system, which moves the wafer underneath the mask for successive exposure.

The minimum feature size in this last case follows from the "Rayleigh criterion", which considers two object points as distinguishable, if the central maximum of the diffraction pattern of one image is outside the first minimum of the other image's diffraction pattern. It can be written as [30]

$$MFS = k_1 \cdot \frac{\lambda}{N.A.}, \tag{4.4}$$

where $N.A.$ is the numerical aperture of the optical system and k_1 is a constant, which takes into account not only the imaging optics but also the behavior of the resist.

4.3.2 Electron-Beam Lithography

Electrons can be focused and deflected by electric and magnetic fields. This concept is used to expose resist by scanning the areas of interest with a fine beam, as is shown in figure 4.1(b). The result are very fine lines down to 7 or 5 nm [24], but this method is rather time-consuming.

4.3.3 X-Ray Lithography

X-ray lithography is a kind of optical lithography using very high energetic photons with very short wavelengths. A feature size of 20 nm can be generated with 1.1 nm photons [31] in thin resist layers.

Another advantage of the use of x-rays is that the long absorption length allows an almost uniform exposure of thick resist structures. In the so-called "Deep X-Ray Lithography" structures up to several millimeters high have been exposed successfully [32, 33]. This is the basic step in the so-called LiGA technique [34].

LiGA is the acronym for the german *Lithograpie, Galvanoformung, Abformung* (lithography, electroplating, moulding) and was invented at the Institut für Microstrukturtechnologie (IMT) at the Forschungszentrum Karlsruhe (Karlsruhe, Germany) in the early 1980's. The high aspect ratio structures created with the x-ray lithography are filled with a metal, and this metal form is then used as a mould for plastics.

The resists used in x-ray lithography are typically resists for DUV lithography, which are also sensitive to these very short wavelengths, or electron-beam resists. In the latter case, photoelectrons that are generated by the incident x-rays are responsible for the actual exposure of the resist.

Chapter 5

X-Ray Masks

As described before, x-ray lithography is based on the concept that some parts of the resist are exposed by x-rays while others, which are covered by an absorber, remain unexposed.

The demands on both the mask absorber and the substrate of the mask, which follow from this concept, are easily seen: The substrate should be as transparent as possible for x-rays of the energy used, while it should still be rather stable to allow a good handling. The absorber, however, should be opaque to block as much of the x-ray beam as possible.

The most common absorbers are gold [35–38] and tungsten [39–41]. The individual absorber thickness depends on the photon energies, which are intended to be used. The mask substrates are usually thin membranes, e. g. of silicon nitride [36, 38, 40, 41] or polyimide [35, 37, 39]. For the use with higher photon energies, thick substrates like silicon wafers are also used [42].

In this chapter, the fabrication of the x-ray masks, which were made for the experiments described later on, is depicted as well as the masks, which were kindly made available in a collaboration with Dr. S. Achenbach of the Forschungszentrum Karlsruhe.

5.1 Gold Masks on Silicon

The x-ray masks that are described in this section are designed for the use with photon energies up to 25 keV. At this energy, the absorption length of silicon, which was chosen as substrate material, is about 1.9 mm. Thus, a silicon wafer of 375 μm thickness has a transmission of 0.82, which allows the use of thick wafers as substrate for test masks. The absorption length of gold, on the other hand, is

only about 12 μm. An absorber thickness of about 20 μm would, thus, result in a transmission of 0.19. This value corresponds to a resist contrast of about 1.4 — a value that is not so uncommon for modern resists.

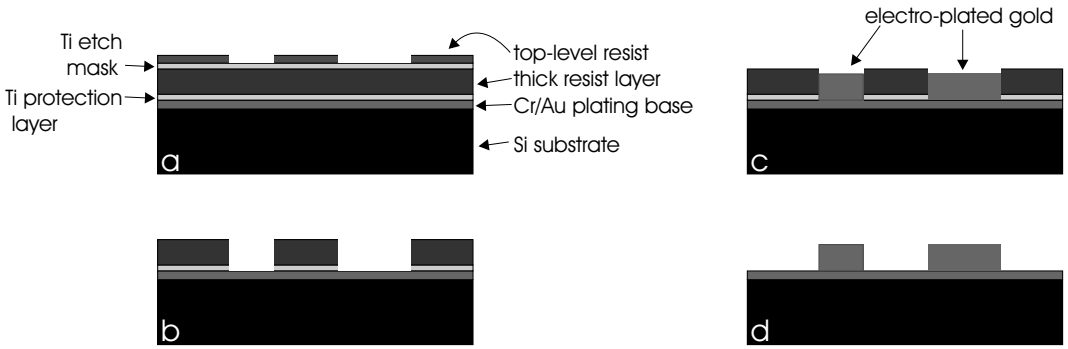

Figure 5.1: Process steps of mask fabrication: (a) wafer with plating base and tri-level resist with structured top-level resist, (b) resist structure after RIE, (c) gold structure after electro-plating, and (d) finished mask after resist removal.

The different processing steps of the mask fabrication are depicted in figure 5.1. They will be described in greater detail in the following.

5.1.1 Substrate

The substrate used for the x-ray masks is a silicon wafer polished on both sides to minimize x-ray scattering. The wafer thickness is 375 μm. Though a thick wafer means a higher absorption than a thin membrane, the handling of the mask becomes considerably easier, in particular at this early stage of the development.

To give an example, the transmissions of a silicon wafer at photon energies of 20 and 25 keV are 0.69 and 0.82, respectively. When compared with glass in visible light, where a sheet of the same thickness would have a transmission of almost 1, these values are still rather poor. But together with the high flux of a synchrotron source, they are acceptable for the demonstration of the principle.

On one side of the wafer, a plating base of 30 nm chrome, which serves as adhesive layer, and 100 nm gold is deposited. On top of this, 30 nm titanium are deposited to protect the gold against the reactive ion etching.

5.1.2 Tri-Level Resist

The negative for the electroplated gold is a thick layer of resist, either PMMA or polyimide, that is spin-coated on top of the plating base with layer thicknesses

between 20 and 50 μm. The chosen resist thickness depends on the wanted absorber thickness and has to be greater than that to ensure an accurate shape of the gold structures.

Since it is difficult to structure resist layers of this thickness directly without x-rays, a so-called tri-level resist [37] is used. On top of the resist, a layer of 150 nm titanium is deposited with another thin layer of resist on it. This last layer is then structured with electron-beam or optical lithography and serves as etch mask for the structuring of the titanium, which in turn is used to structure the thick resist layer via reactive ion etching.

Thick Resists

The PMMA is spin-coated onto the substrate at 4000 rounds per minute (rpm) and then baked on a hotplate at 175 °C for 7 hours to drive out the solvent. To minimize stress in this thick layers, the temperature is ramped at 4 ° per minute.

The second kind of polymer that is used as thick resist layer is an aromatic polyimide. An polyimide precursor (Probimide 7510 by Olin Microelectronic Materials) is spin-coated onto the substrate at 2000 rpm and then baked at 100 °C to drive out the solvent. This step can be repeated several times to create thicker layers. The actual polyimide is formed by exposing the precursor to UV light in an optical lithography system (see below) and then baking it at 300 °C for 3 hours. The temperature is again ramped at 4 ° per minute.

Optical Lithography

A part of the patterns is transferred via optical lithography. The resist that is used for this is AR-U 4040 by Allresist GmbH, a commercially available resist based on novolac with diazonaphthoquinone as photoactive component. This resist is spun onto the titanium at 4000 rpm and baked at 90 °C, forming a layer of about 1400 nm thickness.

The optical exposures for the lithography as well as the exposure of the polyimide are performed with a Suss MJB 3 Mask Aligner with a mercury lamp.

After the exposure the resist is developed in a commercially developer based on tetramethylammonium hydroxide (AR-300-49 by Allresist GmbH) and then rinsed in de-ionized water.

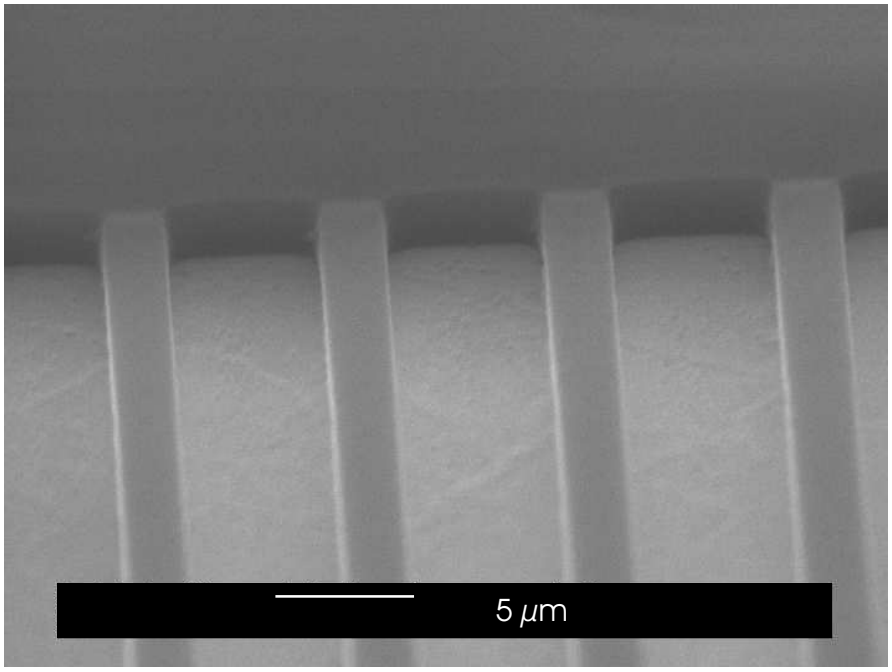

Figure 5.2: Electron-beam resist on titanium after development

Electron-Beam Lithography

The electron-beam lithography is done using a PMMA resist with an average molecular weight of 496,000 g/mol (AR-P 651.04 by Allresist GmbH). When spun at 6000 rpm, this resist gives a layer of about 300 nm thickness. The resist is baked at 175 °C for 5 minutes. After the bake this resist is hard enough, so that another layer can be deposited on top of the first one without dissolving it. Thus, it is possible to create thicker layers by several consecutive coatings. The exposures are done with a Philips SEM XL30 at 20 keV. The resist is developed in a mixture of isopropyl alcohol and methyl isobutyl ketone (AR-600-56 by Allresist GmbH) and then rinsed in isopropyl alcohol. An example for a resist mask after exposure and development is shown in figure 5.2. This process state corresponds to figure 5.1(a).

5.1.3 Reactive Ion Etching

Reactive ion etching (RIE) offers high aspect ratios and a high accuracy in transferring lithographic patterns. Thus, it is a very common tool in the various fields of microtechnology.

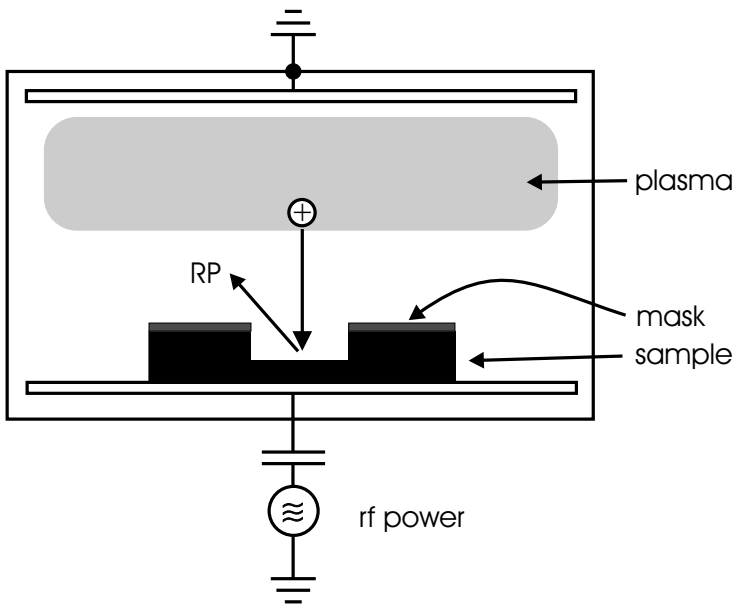

Figure 5.3: Basic RIE reactor. RP denotes the volatile reaction products; rf stands for radio frequency.

A typical RIE reactor is depicted in figure 5.3. Radio frequency (rf) is used to create a plasma from a gas with well defined pressure and flow. The gas or mixture of gases used in a process is chosen so that the ions can react with the solid to be etched and form gaseous products. The ions are accelerated from the plasma towards the negatively charged sample and gather enough energy to initiate chemical reactions.

The characteristics of a process, i. e. the etch rate and degree of anisotropy, are mainly controlled by the pressure of the gas and by the radio frequency power. A low pressure means that the ions are scattered only very little. Since they are highly directed, they chiefly react with the bottom of the structures, which is perpendicular to their direction, and not with the side walls. Thus, this process is highly anisotropic. The rf power influences the energy of the ions reaching the sample. This results in an increase of the anisotropy as well as the etch rate with increasing power. The reactive ion etching described here is performed with a SI 591 by Semtec Instruments GmbH.

The titanium is etched in a sulfur hexafluoride (SF_6) plasma. The parameters can be seen in table 5.1. The structured titanium then serves as an etch mask for the thick resist layer.

The resists are etched in an oxygen plasma with very low pressure to provide a high anisotropy. The exact parameters can be found in table 5.1. Since the etch

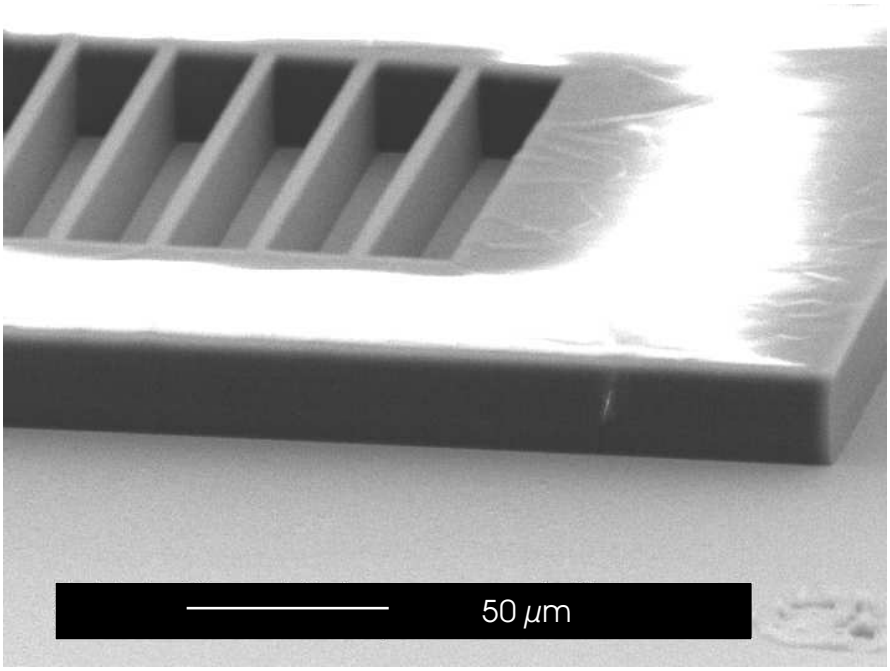

Figure 5.4: Thick resist structure, which serves as negative for electro-plating. The white areas in the picture are caused by charging effects due to the scanning electron microscope.

rates of these processes are very low, it takes up to 18 hours to completely remove the resist. To avoid extensive heating of the sample, the etching is performed in intervals with 20 minutes of etching and 5 minutes pauses.

After the resist etch, the titanium on the bottom of the trenches and on top of the resist is etched with the same parameters that are used before to define the titanium mask. The remaining thick resist structures (cf. fig. 5.1(b)) serve as negatives for the electroplating of gold. An example of a thick resist structure is shown in figure 5.4.

material	plasma	flow [sccm][a]	pressure [Pa]	power [W]
Ti	SF_6	5	1	100
PMMA	O_2	5	0.15	85
Polyimide	O_2	5	0.3	150

Table 5.1: Parameters for reactive ion etching.

[a] ccm per minute at 1.2 Pa

5.1.4 Electroplated gold

The thick gold structures that form the actual x-ray mask are electroplated from a potassium gold cyanide bath (PUR-A-GOLD 401 by Blasberg Oberflächentechnik GmbH). The temperature of the bath is 60 °C and the pH-value 5.8. To guarantee a uniform deposition, the bath is stirred, and the sample together with the cathode is moved parallel to the anode. The typical current density is 5 mA/cm^2, which results the deposition rate of 160 nm/min.

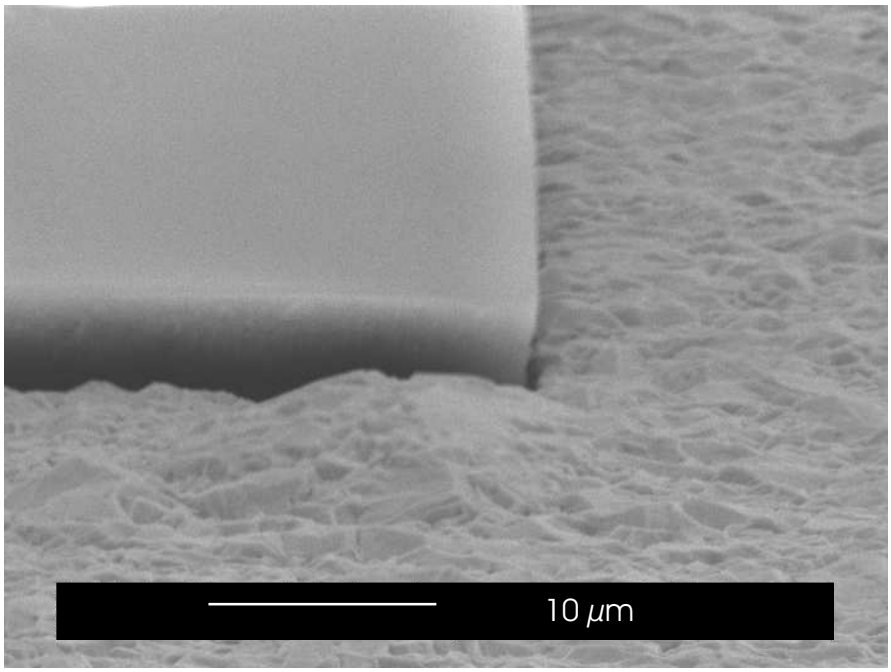

Figure 5.5: Detail of a mask structure right after electroplating. The higher structure is the resist negative, and the lower one with the rough surface is the electroplated gold.

Figure 5.5 shows the micrograph of a mask detail right after the electroplating. The higher structure is the resist negative. The electroplated gold has a rather rough surface, but compared to the total thickness of the gold, differences in the absorption due to this unevenness are negligible.

After the electroplating, the resist negative is removed. The PMMA can easily be removed with organic solvents. It takes 30 minutes in hot n-methyl-2-pyrrolidone (NMP) to remove a PMMA layer of 35 μm thickness. The polyimide, however, is much more stable. To remove it, the sample is left for 24 hours in hot NMP, which dissolves the polyimide into large fragments that partially peel off of the mask. The remains are removed in a high pressure oxygen plasma. In figure 5.6

a gold mask for a Hall bar structure is shown as an example for a completely structured mask.

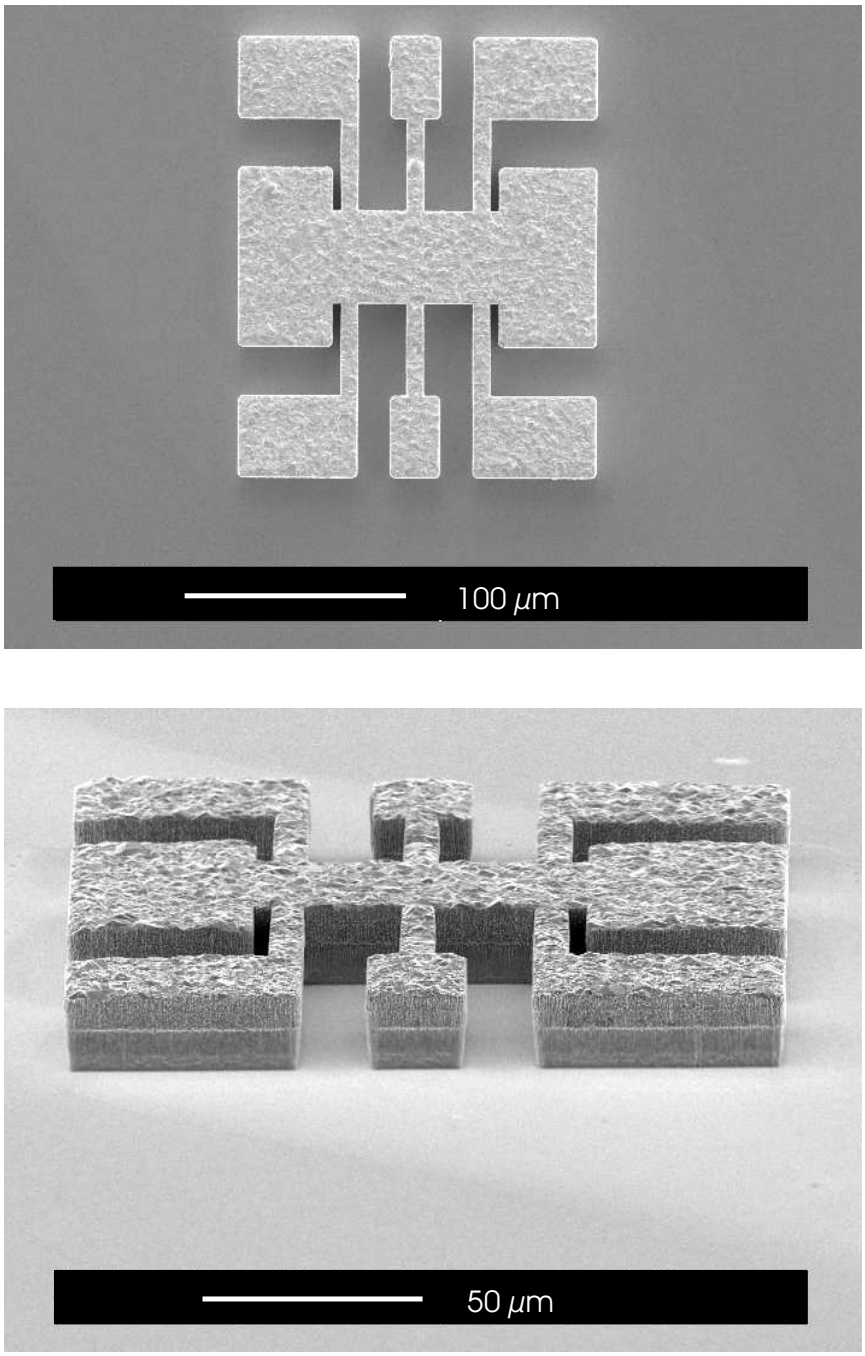

Figure 5.6: Gold mask for a Hall bar structure

5.2 Masks by the IMT

Several masks that were used in the x-ray lithography experiments were provided by the Institut für Mikrostrukturtechnik (IMT) at the Forschungszentrum Karlsruhe, Germany in a collaboration with Dr. S. Achenbach.

These masks have gold absorbers with thicknesses between 22 and 28 μm. The substrates are beryllium wafers of 300 μm thickness. An example of a mask for a wagon wheel that was made by the IMT can be seen in figure 5.7.

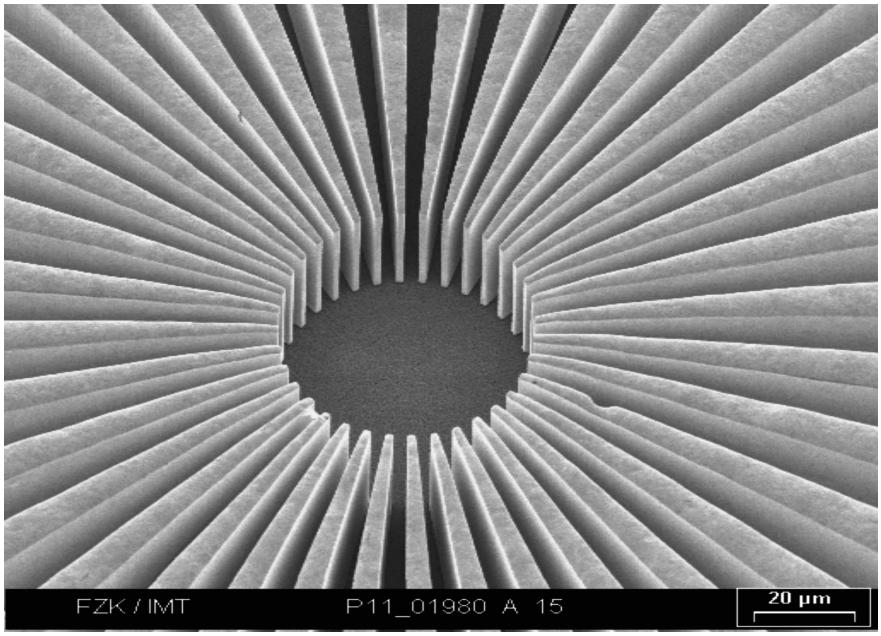

Figure 5.7: Wagon wheel mask by the IMT, by courtesy of S. Achenbach

Chapter 6

Experimental Results

As has been discussed in chapter 3, the parabolic refractive x-ray lenses (PRXL) work well with imaging and microscopy applications [4, 5, 7, 8]. Their mode of operation is similar that of the well-known glass lenses for visible light. In optical lithography, demagnifying imaging systems are often applied to generate patterns with very small feature sizes. Thus, it is obvious that a similar setup for x-ray lithography should be an interesting tool. This is especially true for x-ray lithography with high photon energies, where the mask absorbers have to be rather thick due to the decrease in absorption and are, thus, difficult to produce for small feature sizes.

In the first part of this chapter, the experimental setup will be discussed that is used to generate demagnified images with synchrotron radiation. The tools that are used to enhance the field of view are discussed in greater detail, as well as the camera, which is used for imaging, and the lithographic resist that is used. In the second part, the results of the first demagnifying x-ray lithography experiments are depicted together with the influence of some parameters. At the end of the chapter, the quality of the resist edges that are produced in the lithography experiments will be closer looked upon.

6.1 Setup

The experimental setup is shown schematically in figure 6.1. It is situated roughly 60 meters away from the undulator source. The x-ray lithography experiments were carried out at the beamline ID 22 at the European Synchrotron Radiation Facility (ESRF) in Grenoble. This beamline is primarily specialized in imaging application at a micrometer scale.

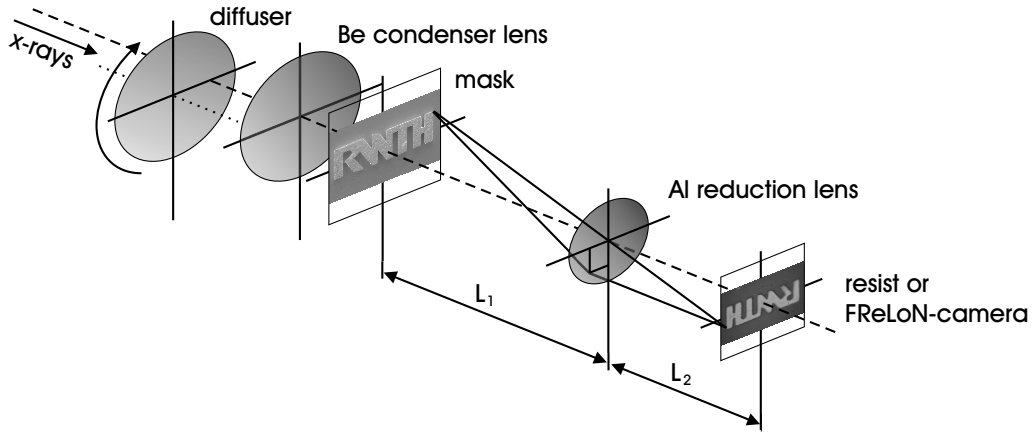

Figure 6.1: Experimental setup

The first elements that the monochromatic or pink beam passes through are a beryllium condenser lens and a rotating diffuser made of boron carbide (B_4C), standing right in front of the mask. These devices will be described in greater detail later on. Their main effect in these experiments is to increase the field of view and to destroy the lateral coherence, so that larger structures can be exposed and interference fringes are suppressed. The distance between these two components is 145 mm, and the distance between the condenser lens and the mask is 187 mm. The condenser lens has not been available before November 2001, so a part of the experiments was carried out with only the diffuser as enhancement. In this case the distance between diffuser and mask is 175 mm.

The mask is made from gold on a silicon or beryllium substrate as described in chapter 5. It typically contains a variety of different structures. The mask carrier stands on a movable stage, so that a specific structure can be moved into the beam at a time.

The aluminium lenses used for imaging are placed about 3600 mm away from the mask. They are described in detail in chapter 3. A typical compound lens consists of more than hundred single lenses, resulting in a focal length between 700 and 1000 mm at photon energies around 20 and 25 keV.

The demagnified image is recorded by means of either a lithographic resist or a so called FReLoN CCD-camera, which will be described later on. The mount for the resist coated samples is attached to the camera so that both are in the same image plane. This makes it possible to use the FReLoN for finding the focus of the imaging lens and for adjusting the mask and then to bring to resist into this focus by simply moving the stage sideways.

6.2 Enhancement of the Field of View

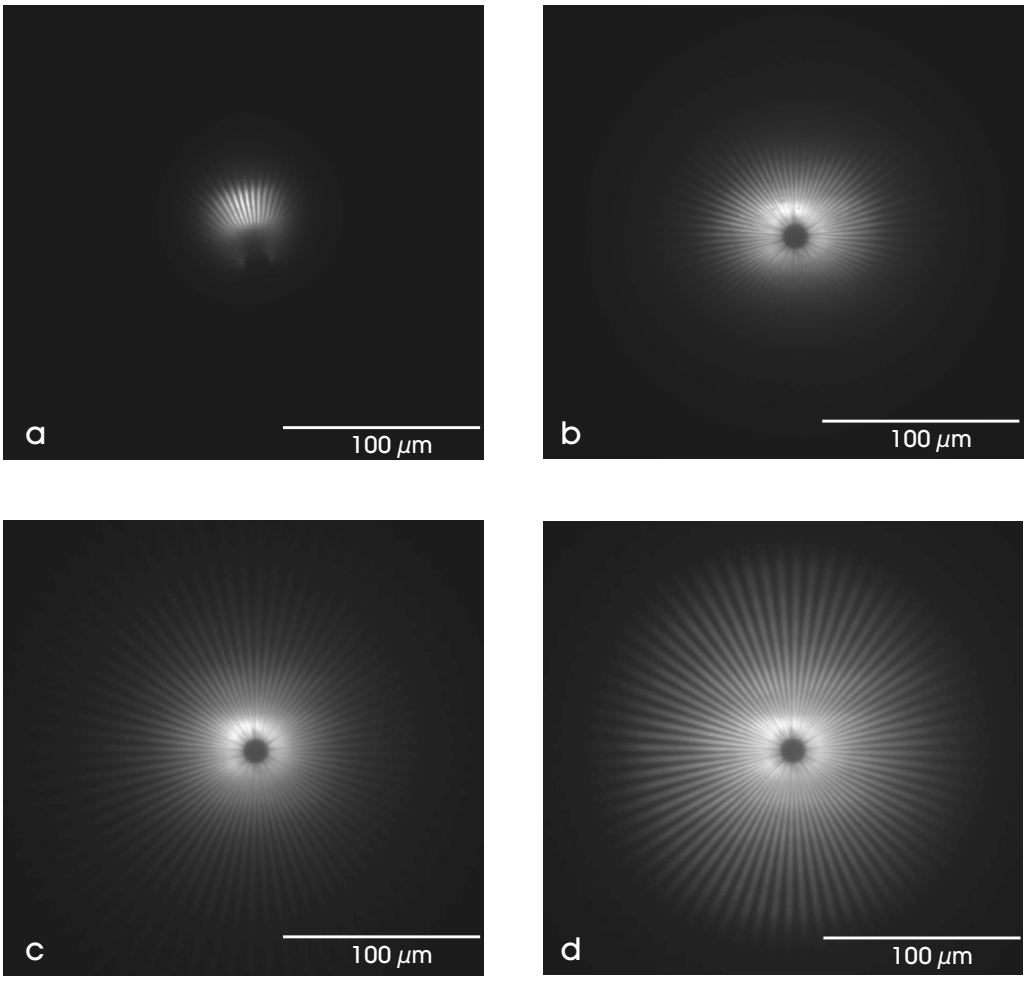

Figure 6.2: Field of view with different experimental settings: (a) without diffuser or condenser lens, (b) with Be condenser lens, (c) with diffuser, and (d) with both diffuser and condenser lens

Starting from a basic setup with mask, imaging lens, and resist coated sample, a way to enlarge the field of view and to enhance the intensity exposing the resist was sought. The results are shown in figure 6.2: It is possible to enlarge the field of view by about a factor of four by using both a diffuser and a condenser lens made of beryllium parabolic lenses.

The mask that is used to create these pictures has a gold absorber of approximately 22 μm thickness and a 300 μm thick beryllium substrate. It is illuminated with a pink beam with an average energy of 19.68 keV. The imaging lens consists

of 108 single aluminium lenses, which results in a focal length of 714 mm at the given energy. The distances (cf. fig. 6.1) are $L_1 = 3600$ mm and $L_2 = 887$ mm, resulting in a demagnification factor of 4.1. The images in figure 6.2 are taken with the FReLoN-camera.

6.2.1 Condenser Lens

In a part of the experiments, a condenser lens made of beryllium is used to enlarge the field of view and to increase the intensity that falls onto the sample. The design of the condenser lens is similar to that of the aluminium imaging lenses described in chapter 5. To prevent corrosion of the beryllium, which can be induced by hard x-rays due to ozone formation in the air, the container of the beryllium lens is sealed with capton foil and flushed with nitrogen. The condenser lens used in the experiments described here consists of 16 single parabolic lenses with an aperture of slightly less than 1 mm.

This lens influences the size of the field of view, as can be seen in the FReLoN images in figure 6.2(a) and (b). The upper left image of a wagon wheel was taken without any optical enhancement, the upper right one with the condenser lens.

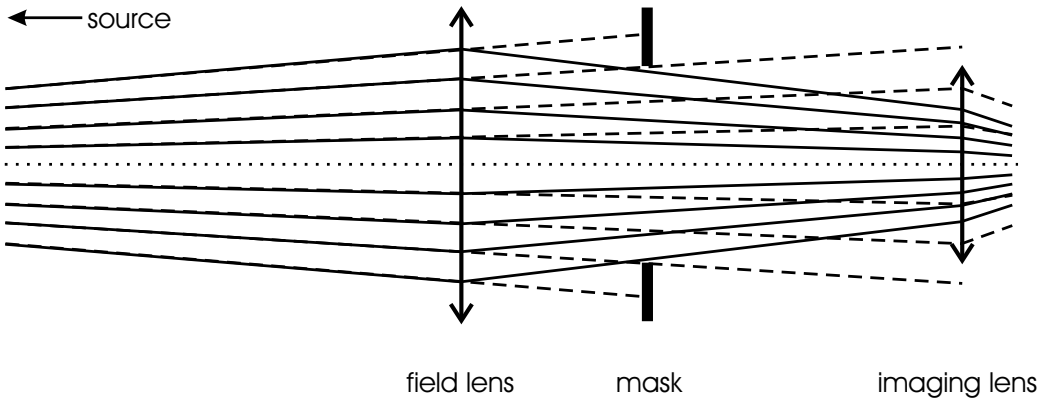

Figure 6.3: Function of the condenser lens. The solid lines show the path of the x-rays, when the field lens is used. The dashed lines show the path without field lens for comparison.

The use of the condenser lens increases both the field of view and the intensity that falls onto the resist. The reason for this behavior is depicted in figure 6.3: The condenser lens directs x-rays that cross the mask at points away from the optical axis towards the aperture of the imaging lens. Since the rays converge behind the condenser lens, the area of the mask that is seen by the aperture of the imaging lens is larger than it would be in the case of parallel or diverging

x-rays. Not only the increase in the field of view is important for the lithography but also the increase in intensity, since the exposure times are up to several hours long, depending on resist and intensity, when high energetic x-rays are used.

6.2.2 Diffuser

The diffuser is made of boron carbide (B_4C) powder between two thin glass plates. The particle size of the powder is in the range from 1 to 7 μm. The layer is 5 mm thick and is rotating with 8.7 Hz. The diffuser is placed eccentrically in the path of the x-rays, so that the illuminated region is permanently changing.

The diffuser partially destroys the lateral coherence of the synchrotron radiation. It, thus, eliminates interference fringes, which would otherwise appear in the images at the borders between the transparent and absorbing areas of the mask. It also broadens the field of view, as can be seen when comparing figure 6.2(c) with 6.2(a).

The best results were achieved, when using both the condenser lens and the diffuser. This can be seen in figure 6.2(d).

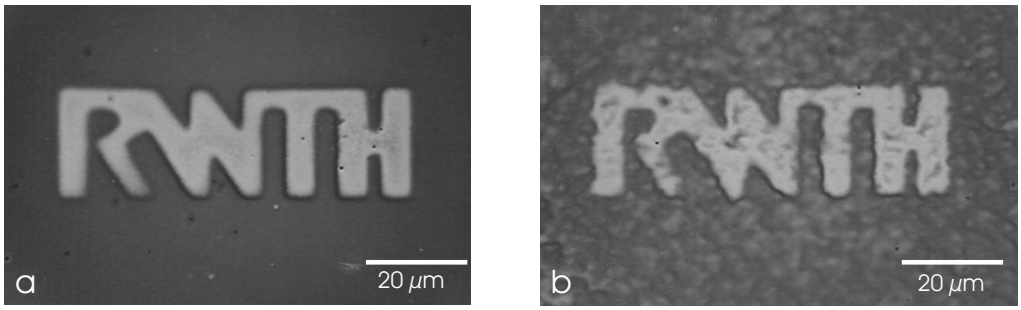

Figure 6.4: Images obtained with the diffuser: (a) diffuser rotating at 8.7 Hz, (b) diffuser standing still

Figure 6.4 shows two images taken to illustrate the influence of the rotation of the diffuser. The images are exposures of the resist AR-N 7700.18 described below on a $In_{0.52}Ga_{0.48}As/InP$ layer. The mask consists of 15 μm thick gold on 375 μm of silicon. It is illuminated by monochromatic x-rays with an energy of 25 keV. The imaging lens consists of 120 single aluminium lenses and has a focal length of 985 mm. The demagnification factor is 2.8, resulting from the distances $L_1 = 3620$ mm and $L_2 = 1283.5$ mm. The exposure time is 25 min in both cases.

Figure 6.4(a) is taken with a rotating diffuser. The rotation speed is 8.7 Hz, which is the typical setting used in our experiments. The second image is taken

while the diffuser is standing still. It shows a clear speckle pattern, which is typical for coherent light passing through a disordered medium. Only when it is rotating, the diffuser is able to destroy the coherence of the incident synchrotron radiation in combination with long exposure times.

6.3 Imaging

The easiest way to test an imaging setup is of course the use of a CCD-camera. Thus, it is also a helpful tool for adjusting a setup. The camera that is used in these experiments will be described here together with the resist that is used for the x-ray lithography.

6.3.1 FReLoN-Camera

This CCD-camera was developed by the "Analog and Transient Electronic" group at the ESRF in Grenoble, France [11]. Its name is an acronym for "Fast Readout, Low Noise". This CCD-camera is typically used with a microscope optic and a single-crystal scintillator.

In the experiments described here the scintillator is a lutetium aluminium garnet crystal with an europium doped layer of 3.5 μm thickness. The microscope used here has an objective with a magnification of 20 and an ocular with a magnification of 2. The pixel size of the 2048 x 2048 CCD-chip is 14 μm. Thus, the magnification described above results in an effective pixel size of 0.35 μm and a total field of view of 716.8 μm squared.

In these experiments, the FReLoN-camera was used for the adjustment of the various components of the setup, for the selection of a specific mask pattern, and for finding the focus of the imaging lens. Examples for pictures that are taken with this camera are shown in figure 6.2.

6.3.2 AR-N 7700.18

AR-N 7700.18 is a commercially available resist by Allresist GmbH. It is a chemically amplified negative resist created for electron-beam lithography. The main components are a mixture of different novolac-resins solved in an organic solvent.

The resist is typically spin-coated onto a substrate with 6000 rpm resulting in a layer thickness of about 260 nm. It is then dried on a hot-plate at 85 °C for one minute to completely drive out the solvent.

A typical exposure time in x-ray lithography is about 25 minutes in a monochromatic beam of 25 keV with a typical flux of about 3×10^{11} photons/(s mm^2). In a pink beam with an average energy of 19.68 keV, where the flux is about 7.5×10^{12} photons/(s mm^2), it takes less than a minute to expose the resist.

A post-exposure bake is done at 110 °C on a hot-plate. It induces a cross-linking process, which reduces the solubility of the resist in the developer. The exposed layers are developed in a commercially available developer adjusted for the use with this resist (AR-300-47 by Allresist GmbH). It is a metal-free developer based on tetramethylammonium hydroxide in a aqueous solution (less than 5 %). The developer can be used undiluted as well as diluted with de-ionized water in different ratios. The dilution of the developer influences not only the time of the development but also the contrast of the resist. Directly after the development, the sample is rinsed in de-ionized water and blown dry with nitrogen. Dose series with electron-beam lithography show a contrast of 1.7 for this resist and the diluted developer.

6.4 Demagnifying Lithography

To demonstrate the demagnifying x-ray lithography, the setup described above is used (cf. fig. 6.1) with a monochromatic beam with a photon energy of 25 keV. One of the first lithographic structures that was produced with this method is shown in figure 6.5(b) together with the mask, which is shown in the micrograph in figure 6.5(a). The demagnification factor is 2.8.

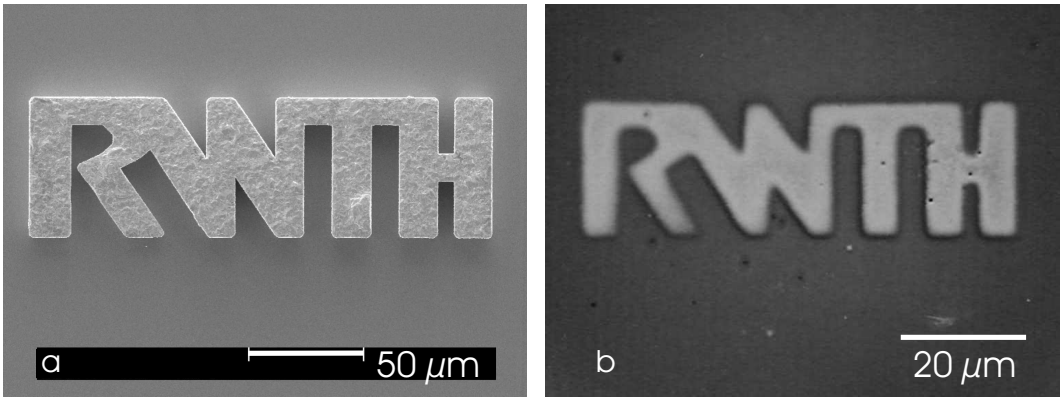

Figure 6.5: Pictures of a gold mask absorber (a) and a resist picture (b). The demagnification factor was 2.8.

The resist used in the sample depicted in figure 6.5(b) is AR-N 7700.18 on a $In_{0.52}Ga_{0.48}As$/InP layer. It was spin-coated at 6000 rpm and baked at 85 °C on a

hot-plate for one minute. The exposure time was 25 minutes in a monochromatic beam at 25 keV with a flux of 3.2×10^{11} photons/(s mm^2). The post-exposure bake was done on a hotplate at 110 °C for 150 seconds. The developer AR-300-47 was diluted with de-ionized water at a ratio of 12:1, and the development time was 80 seconds.

The mask absorber is 15 μm of gold on a 375 μm thick silicon wafer. The imaging lens consisted of 120 single aluminium lenses. This results in a focal length of 985 mm at 25 keV. The object distance was 3620 mm and the image distance was 1283.5 mm. The diffuser but no condenser lens was used.

It is obvious from figure 6.5 that the demagnifying lithography in fact worked quite well in this first test. However, the structures show a strong proximity effect that is mainly caused by the secondary electrons from the substrate. The blurred edges and rounded corners indicate this. This effect is well known in varying strength from all kinds of lithography. Its strength in the experimental setup used here will be discussed in the simulations in the next chapter in greater detail.

6.4.1 Monochromatic versus Pink Beam

Lithographic exposures with a high energetic monochromatic beam, as in the example described above, take a rather long time due to the low absorption at these energies. On way to decrease the exposure time, simply would be to increase the flux that reaches the sample. Since the high energetic resolution of a monochromatic beam is not necessary for lithographic exposures, the easiest way to increase the photon flux in the given setup is to remove the monochromator and to work with a pink beam.

The exposure time for AR-N 7700.18 is about 20 min at a photon energy of 20 keV and a flux of 3×10^{11} photons/(s mm^2). When the setting is changed to pink beam with an average energy of 19.68 keV, the flux increases to 7.5×10^{12} photons/(s mm^2) and the exposure time decreases to about 30 seconds, which significantly helps to increase the throughput of this method. An influence of the chromatic aberration, that could be expected due to the broader energy band of the pink beam ($\Delta E/E \sim 10^{-2}$), could not be seen in these experiments, since the edges of the resist structures are already smeared out over several micrometers due to the strong proximity effect, when a monochromatic beam is used.

6.4.2 Different Doses

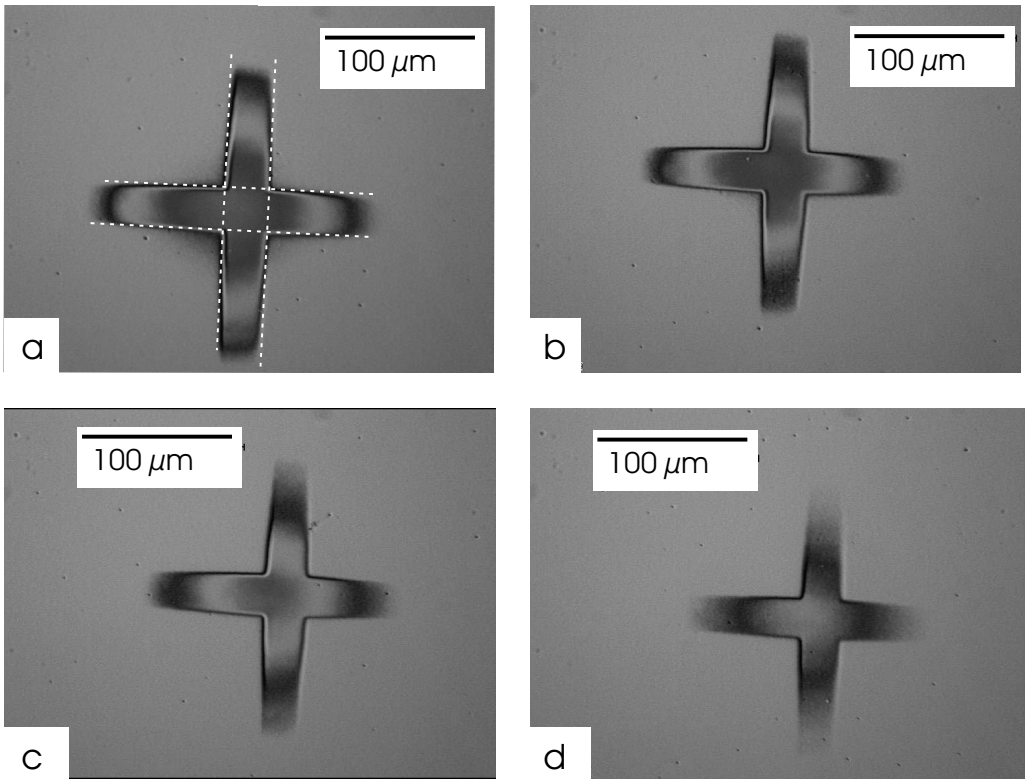

Figure 6.6: Parts of a series of exposures of AR-N 7700.18 with different doses. Exposure times are (a) 60 seconds, (b) 40 seconds, (c) 25 seconds, and (d) 5 seconds in pink beam.

Figure 6.6 shows some parts of a series of exposures with different doses. The exposures are done with a pink beam with an average energy of 19.68 keV and a flux of 7.5×10^{12} photons/(s mm^2). Before the exposure, the resist was spun onto a silicon substrate at a speed of 6000 rounds per minute and then baked at 85 °C on a hotplate for one minute. The post-exposure bake was done at 110 °C on a hotplate for 120 seconds. After this the resist was developed in AR-300-47 diluted with de-ionized water at a ratio of 2:1 for 23 minutes.

The mask absorber is 22 μm of gold on 300 μm beryllium. The width of the arms of the crosses is 120 μm. The imaging lens consists of 108 parabolic aluminium lenses resulting in a focal length of 714 mm at the given energy. The experimental geometry with $L_1 = 3660$ mm and $L_2 = 888$ mm results in a demagnification factor of 4.1. The exposure times were 60, 40, 25, and 5 seconds. Both the

condenser lens made of 16 beryllium lenses and the rotating boron carbide diffusor were used.

Since the mask structure is larger than the spot of synchrotron radiation, it is illuminated neither completely nor uniformly. Due to this situation, the exposed and developed features appear in different colors, which can be seen in figure 6.6 as different shades of gray. The reason for this is the fact that not completely exposed resist is partially removed in the developer. The remaining resist height depends on the applied dose. The profile of the structures reproduces the Gaussian shape of the intensity of the beam. Due to this behavior the crosses are smaller for smaller doses.

The edges of the crosses do not appear as straight lines in the outer regions of the exposure, since the developer attacks the partially exposed resist not only from above but also from the edges, as soon as the unexposed areas around it are completely removed. Thus, areas where the exposure dose is less than the sensitivity are smaller after the development than the fully exposed structures for a negative resist like the one used here. An overexposure of features, on the other hand, can result in a broadening of structures that becomes stronger with increasing dose and exposure time, respectively. The reason for this is the proximity effect: The shadowed areas next to the exposed features are also exposed with a comparatively low dose. When the accumulated dose in this areas is sufficient for a partially exposure, the feature become broader and smear out. In figure 6.6(a), dashed lines have been introduced to indicate expected form of the resist structure. Due to the inhomogeneous illumination of the mask, a compromise has to be found between a strong overexposure of the features in the center of the beam and an underexposure of the features at the edges. Thus, a further increase in the mask absorber thickness may be necessary to compensate the increase in dose that exposes the shadowed areas of the resist in the beam center.

6.4.3 Different Developments

As has been discussed in chapter 4, the different parameters of the development can influence the results of a lithographic process significantly. In the following, the influence of the dilution of the developer will be discussed.

The influence of two different dilutions on the outcome of the lithographic process can be seen in figure 6.7. Sample (b) was developed in undiluted AR-300-47. Sample (a) is taken from the same dose series as shown in figure 6.6 and was developed in a mixture of two parts AR-300-47 and one part de-ionized water.

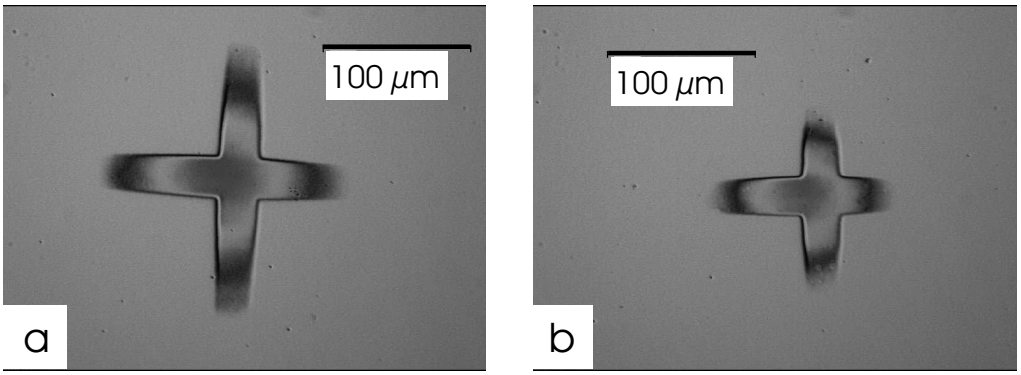

Figure 6.7: Comparison of the effects of different developer dilutions: (a) 1:2 in de-ionized water (b) undiluted. The exposure time was 30 seconds in both cases.

Both samples were spin-coated with AR-N 7700.18 at 6000 rounds per minutes and baked on a hotplate at 85 C for one minute. The post-exposure bake was done on a hotplate at 110 °C for two minutes. The parameters for the exposure are the same for both samples and are described above. The samples shown in figure 6.7 were both exposed for 30 seconds with almost identical fluxes.

As could be expected, the first difference appears at the development times. The diluted developer works at a much slower rate than the undiluted one. The development of sample (a) took 23 minutes, while that of sample (b) took only 59 seconds, since the concentration of the reacting chemicals is higher in the second case.

Figure 6.7 shows clearly that sample (a) is larger than sample (b). Since both samples were exposed with the same dose, this behavior can be explained with the idea, that a lower dose is needed for a complete exposure of the resist, when a diluted developer is used, i. e. that the sensitivity is higher for the resist-developer system with a diluted developer than for the one with an undiluted developer. This is in accordance with what can be found in the literature [43].

6.5 Structure Edges

For use as etch masks or masks for a lift-off process, resist edges after a lithographic exposure and development are expected to be very steep. In our case, unfortunately, the edges are smeared out over a length of 5 μm, as can be seen from the atomic force microscope (AFM) scan in figure 6.8(b).

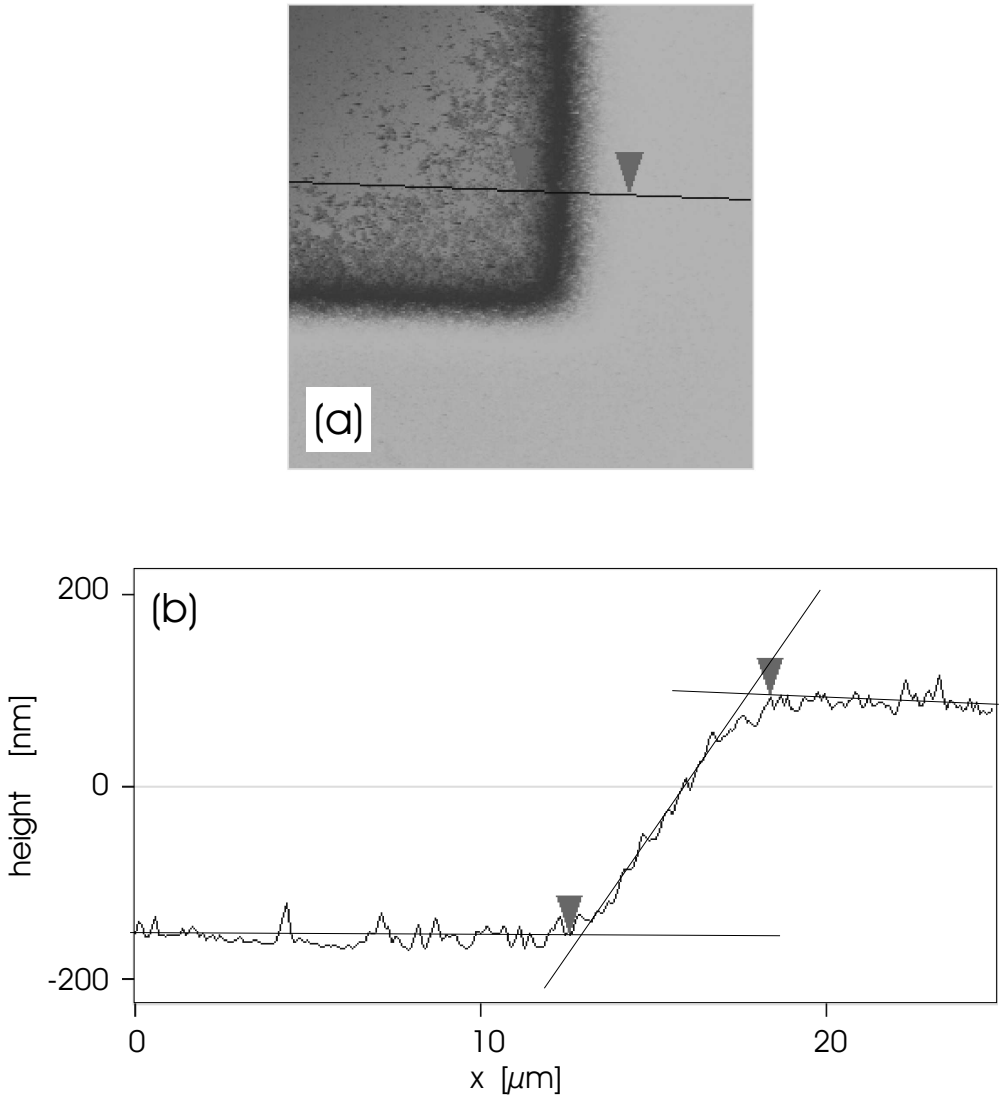

Figure 6.8: AFM scan of an resist edge: (a) detail the sample, which is the same as in figure 6.6(b). The black line in (a) indicates where the cross-section (b) has been taken.

The sample, of which the cross-section has been taken is the same as in figure 6.6(b): The resist was AR-N 7700.18. It was exposed with a pink beam at a photon energy of 19.68 keV and a flux of 7.5×10^{12} photons/(s mm^2) for 40 seconds. It was developed in a mixture of AR-300-47 and de-ionized water with a ratio of 2:1 for 23 minutes. A detail of the sample with a line, where the cross-section is taken, is shown in figure 6.8(a).

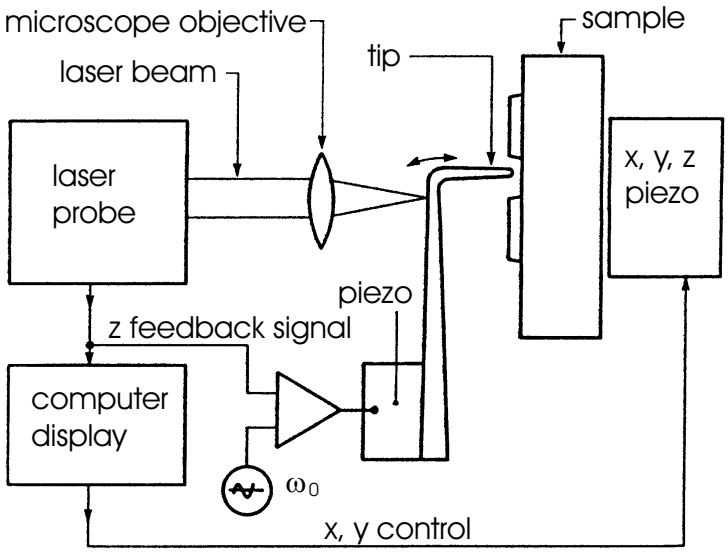

Figure 6.9: Block diagram of an atomic force microscope [44]

A diagram for an atomic force microscope is shown in figure 6.9. It can be used to measure the surface topology of a sample quite accurately. This is done by controlling the forces that act between the surface and tip. Since these forces depend on the distance from the surface, a constant force complies with a constant distance between tip and sample. An unevenness in the surface, thus, results in an up and down movement of the scanning tip that can be measured, e. g. by the reflection of a laser beam.

The tip that was used for the scan in figure 6.8 was a silicon tip with an angle 17° towards the surface normal. This would influence the imaging of an ideal resist step in such a way that a 260 nm high step would appear to be smeared out over 79.5 nm. From this it is obvious that the AFM tip is not responsible for the broadening that is seen in the scan.

In fact, the main reason for this broadening is the scattering of secondary electrons from the substrate. The simulations discussed in the next chapter clearly show this. Other influences such as the imaging quality of the lens, which is discussed in chapter 3, also play only a minor role in the broadening of the edges. The diffraction limited spot size for the given imaging lens, for example, is only about 262 nm in diameter.

Chapter 7

Monte Carlo simulations

The exposure of a resist with x-rays consists of several processes: the absorption of the photons in the sample, the generation of photoelectrons and Auger electrons and their motion through the sample, the generation of fluorescence photons and their absorption in the sample, which can also result in the generation of electrons that behave in the same way as those generated by the primary x-rays. The actual exposure of the resist is due to the moving electrons that deposit their energy in the resist via scattering events, before they come to rest. The individual processes can be described by theoretically and empirically determined probability functions that allow the simulation of the contribution of single photons and electrons. The exposure of the resist can then be described by the summation over a large number of single events. This procedure also permits the separation of the different effects to clarify their contributions.

A common tool for the simulation of statistical processes is the so-called Monte Carlo simulation. It has already been used to simulate the influence of the secondary electrons on x-ray lithography, mainly with soft x-rays, by a number of authors [45–48].

In this chapter, a simulation algorithm will be described that allows one to clarify the influence of the high energetic photoelectrons that are created by hard x-rays and the accompanying Auger electrons and fluorescence photons on the broadening of the resist features. In the first part the simulation model is described, while in the second part the results of these simulations will be shown.

7.1 Simulation model

7.1.1 Algorithms

Stochastic processes can be described by random numbers. The generation of uniformly distributed random numbers is a standard tool in numerical applications [49] and is usually provided as part of the standard routines of a compiler. However, the probability density functions (p.d.f.) that describe physical processes are often non-uniform. Thus, the basic step of a Monte Carlo simulation is the transformation of a set of uniformly distributed random numbers into a set, whose distribution matches the given probability density. Two algorithms that are used in the simulations below are described in the following.

Inversion transform method

For a given p.d.f. a cumulative distribution function (c.d.f.) $F(x)$ can be calculated, i. e. the probability that the value of the variable is not greater than x. It can be written as

$$F(x) = \int_0^x f(x')dx'. \tag{7.1}$$

The c.d.f. is always monotone increasing and therefore an inverse function $F^{-1}(y)$ can be defined as: $F^{-1}(y)$ is the smallest x for which the equation $F(x) \leq y$ is satisfied [50]:

$$F^{-1}(y) = \inf\{x : F(x) \leq y\} \tag{7.2}$$

With this method a set of uniformly distributed random numbers can be transformed directly into a set of random numbers, whose probability density function is f. However, it can only be implemented efficiently, if an analytical expression for $F^{-1}(y)$ exists.

Von Neumann rejection

Another method is the so-called von Neumann rejection that is depicted in figure 7.1. Here, two random numbers from uniform distributions are used to generate a distribution that reflects f: For the first value x_i from the interval $[x_{min}, x_{max}]$ the value for the p.d.f. $f(x_i)$ is calculated. It is then compared to the second value y_i from the interval $[0, f_{max}]$. If the inequality $f(x_i) \geq y_i$ is fulfilled, x_i is accepted for the simulation, otherwise the pair of random numbers is rejected and the procedure is repeated, until a proper pair is found.

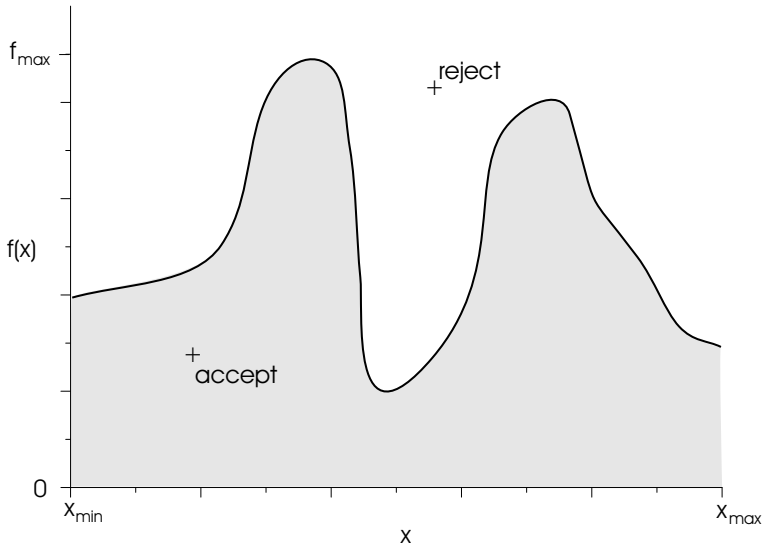

Figure 7.1: Principle of the von Neumann rejection: Pairs of values that belong to points inside the shaded area are accepted, those outside are rejected.

7.1.2 Simulated sample

The schematic drawing of the simulated system is shown in figure 7.2: The sample consists of a thin resist layer on a substrate. It is exposed with an ideally thin line of monochromatic x-rays perpendicular to the sample surface. To obtain the energy that is deposited in a given unit volume, the resist is divided into rods, which are exemplarily shown in the upper left area of the sample in figure 7.2. The energy that the electrons lose on their way through a given rod is stored according to its coordinates. This results in a two-dimensional plot of the energy distribution as the one depicted in figure 7.7.

A photon of the incident beam can be absorbed anywhere on its way through the sample. The absorption results in the generation of a photoelectron at the location of the absorption, whose trajectory and energy deposition are recorded. When the photoelectron has come to rest, either an Auger electron or a fluorescence photon is generated at the location of the absorption of the photon. The Auger electron is treated in the same way as the photoelectron. The fluorescence photon travels on a straight line through the sample, and when it is absorbed, another photoelectron is generated. The three processes can be toggled on and off in the simulation program to separate their effects. This procedure is repeated, until 5,000,000 photons of the primary beam are absorbed.

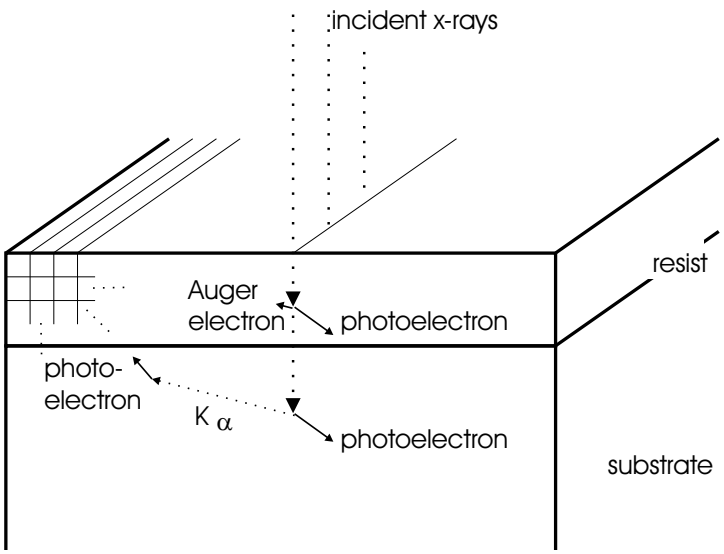

Figure 7.2: Schematic drawing of the simulation setup and the processes taken into consideration. The drawing is not to scale.

Resists

For a resolution of 1 nm, which was used in these simulations, matter can be described in a continuum limit. Thus, the position of the individual atoms will be neglected here, and only the stoichiometrical composition is taken into account. The rods in figure 7.2 have a square section of 1 nm×1 nm. The composition for the resist AR-N 7700.18, which was also used in the experiments described in the previous chapter, is shown in table 7.1 together with two modifications of it, which are designed for special x-ray energies and will be discussed in the next chapter in detail.

Substrates

Different substrates are used in the simulations. Just as the resist, they are described with a continuous distribution and a resolution of 1 nm. A typical substrate thickness in a real experiment is in the range of a few hundred micrometers. The silicon substrates, which are used in the experiments described in the previous chapter, have a thickness of 375 μm. Most of the absorption events in this substrate, however, do not affect the resist, since electrons and fluorescence photons are generated deep inside the substrate and can not reach the resist.

		AR-N 7700.18	AR-N 7700.18 with bromine	AR-N 7700.18 with 16 % Pd-acetate
hydrogen	[at. %]	7.05	7.05	12.32
carbon	[at. %]	72.73	72.73	65.36
nitrogen	[at. %]	2.36	2.36	1.98
oxygen	[at. %]	14.18	14.18	16.18
chlorine	[at. %]	3.68		3.09
bromine	[at. %]		3.68	
palladium	[at. %]			1.07
density	[g/cm^3]	1.14	1.14	1.14
thickness	[nm]	260	260	260

Table 7.1: Composition [51], density and thickness of the resist used in the experiments and two proposed modifications (cf. chapter 9).

The penetration distance of electrons in a solid can be estimated by [52]

$$r = \frac{0.039}{\rho} E^{1.75}, \tag{7.3}$$

where r is in μm, ρ is the density in g/cm^3 and E is the kinetic energy of the electron in keV. This distance is in the range of a few ten or hundred nanometers up to a few micrometers for the energies and substrates of interest.

The mean penetration depth for x-rays in a solid is

$$D = \frac{1}{\mu}, \tag{7.4}$$

where μ is the linear absorption coefficient. This is the characteristic length that describes the absorption of the fluorescence photons in the substrate and is in the range of a few ten micrometers for the substrates examined here. For example, for a silicon K_α photon it is 11.3 μm and for palladium K_α it is 48.3 μm. Since this length is usually longer than the distance for the electrons (eq. 7.3) for the energies of interest here, it is chosen as the substrate thickness for the simulations.

7.1.3 Absorption

As described in chapter 2, the absorption of x-rays follows Lambert-Beer's law:

$$I(x) = I_0 \exp(-\mu x). \tag{7.5}$$

When the photon energy is larger than the K edge of the absorbing atom, a photoelectron is generated as well as either a fluorescence photon or a Auger

electron. Photon scattering in neglected in these simulations. The photons travel on straight lines until they are absorbed. The above equation can be used to generate the position for an absorption event from a random number (*r.n.*) [45,47]. For a beam perpendicular to the resist layer the distance of this position away from the surface is

$$x = \frac{\ln(r.n.)}{\mu_{\text{resist}}}. \tag{7.6}$$

If the distance x exceeds the resist thickness, a new distance, starting from the resist-substrate interface, is calculated with the absorption coefficient of the substrate instead of that of the resist.

The absorption coefficient μ is calculated from tabulated values for the mass absorption coefficient $\frac{\mu}{\rho}$ [53] and the density ρ. For compound material the absorption coefficient is calculated by means of a relative density (cf. equations 2.4 and 2.5).

The probability that the absorption appears at an atom of the component j of a compound, is given by

$$p(j) = \frac{(\mu/\rho)_j \, \rho_j}{\mu} \tag{7.7}$$

with $(\mu/\rho)_j$ being the mass absorption coefficient ρ_i being the relative density (eq. 2.4) of the component i and μ being the linear absorption coefficient of the compound (eq. 2.5). The element that absorbs the photon is, thus, determined by assigning the components that come into question to successive intervals between 0 and 1, whose size depends on $p(j)$ and then comparing a random number with these intervals.

7.1.4 Photoelectrons

In these simulations, only electrons from the K shell are taken into account as photoelectrons, since they contribute most to photoabsorption. The kinetic energy of a photoelectron is determined from the energy of the incident photon and binding energy of the K shell of the absorbing atom

$$E = E_{\text{Photon}} - E_b(\text{K}). \tag{7.8}$$

The angular distribution of the photoelectrons is anisotropic and is given by [54]

$$p(\theta) = \frac{\sin^2\theta}{\left(1 - \frac{v}{c}\cos\theta\right)^4}. \tag{7.9}$$

Here, θ is the angle between the incident beam and the photoelectron, v is the speed of the photoelectron, and c is the speed of light. For non-relativistic electrons, the function in the denominator can be neglected and the distribution

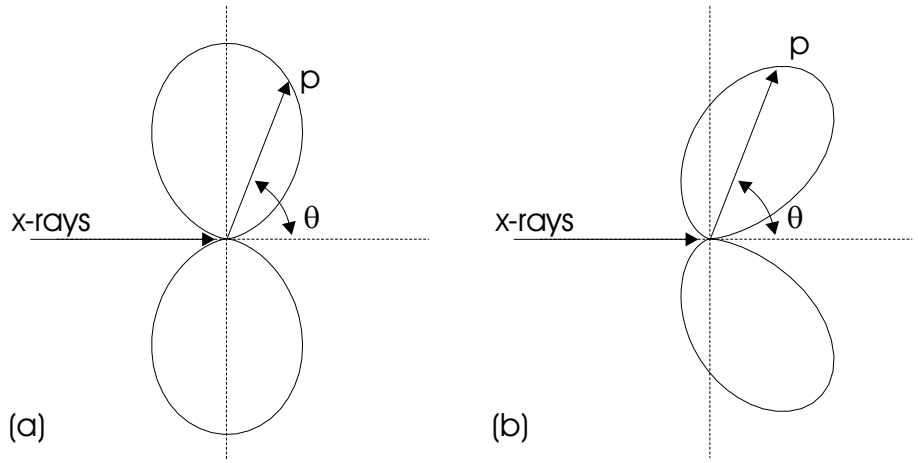

Figure 7.3: Angular distribution of the photoelectrons

is $\sin^2\theta$. This distribution, which is shown in figure 7.3(a), has its maximum perpendicular to the direction of the incident x-rays. However, when the initial energy and, thus, the initial speed of the photoelectrons is relativistic, e. g. due to hard x-rays, the maximum shifts to smaller angles as can be seen in figure 7.3(b). The starting angles of the photoelectrons were determined via van Neumann rejection from equation 7.9.

The electrons travel through the sample on a straight line, which changes direction at random distances due to scattering events. This distance s between two collision is generated from an exponential distribution [47]

$$s = \Lambda_T \cdot \ln(r.n.) \tag{7.10}$$

with $r.n.$ being a random number and $\Lambda_T = \left(\sum n_i \sigma_{T,i}\right)^{-1}$ being the mean free path between collisions, which is calculated from the atomic number densities n_i of the components of the material and the total cross sections $\sigma_{T,i}$ for scattering of a screened Coulomb potential with [47]

$$\sigma_T = \frac{e^2}{64\pi\epsilon_0^2 E^2} \frac{Z(Z+1)}{\chi(\chi+1)} \tag{7.11}$$

and the screening parameter [47]

$$\chi = \frac{e^2 Z^{2/3}}{32\pi\epsilon_0 a_0 E}. \tag{7.12}$$

Here, e is the electron charge, ϵ_0 the electric constant, a_0 the Bohr radius, Z the atomic number and E the electron's energy. The mean free path of the electrons

depends on their kinetic energy and follows a universal curve independent from the elements, as can be seen in figure 7.4. However, since one scattering event is not enough for a high energetic electron to lose all its energy, it can travel a significantly longer distance, until it comes to rest after many scattering events.

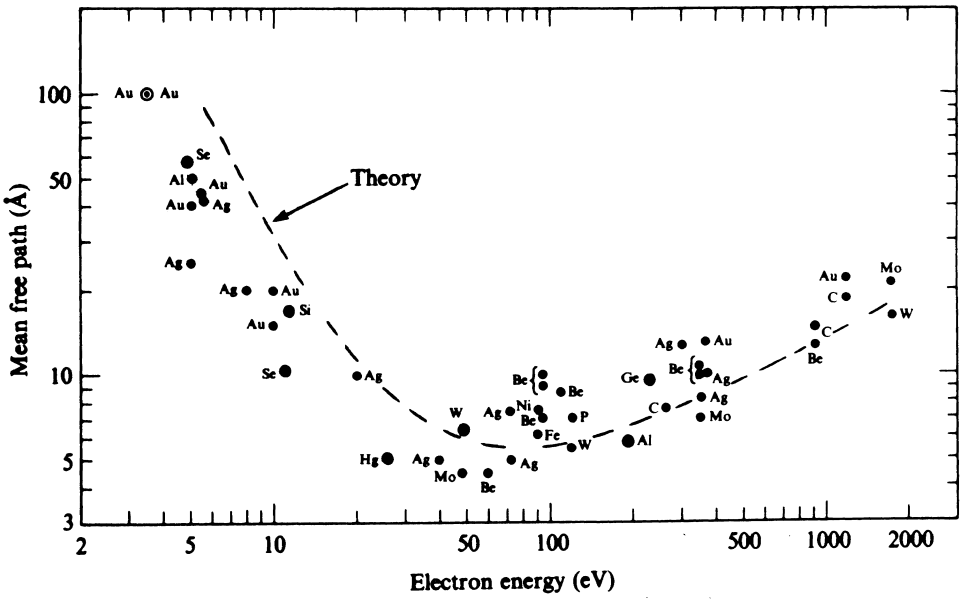

Figure 7.4: Universal curve for the mean free path of electrons in solids [55]

The angle, into which the electron is scattered, is calculated from the Rutherford probability density [47]

$$p_r(\theta) = \frac{2\chi(\chi+1)}{(1-\cos(\theta)+2\chi)^2}. \tag{7.13}$$

The energy loss of the electron on its way through the sample is described by a continuous slowing down approximation (CSDA) [45–47]. Here, a mean energy loss dE is assigned to each section ds of the electron's path. The energy loss was calculated by one of the following two equations, depending on the electron's energy, and stored in the position matrix according to the electron's spatial position. For high energies Bethe's law [56] was used and for lower energies an approximations by Rao-Sahib and Wittry [57]

$$\frac{dE}{ds} = \frac{2\pi e^4 n_i Z}{(4\pi\epsilon_0)^2 E} \ln\left(\frac{1.166E}{J}\right) \quad , \quad E \geq 6.338J \tag{7.14}$$

$$\frac{dE}{ds} = \frac{2\pi e^4 n_i Z}{(4\pi\epsilon_0)^2 1.26\sqrt{EJ}} \quad , \quad \text{otherwise} \tag{7.15}$$

Here, e is the electron's charge, n_i is the atomic number density of the scattering atom, Z is the atomic number of the scattering atom, E is the kinetic energy of the electron. J is the mean ionization potential in eV and can be written as [47, 58, 59]

$$J = \begin{cases} 11.5Z & , \quad Z < 14 \\ 9.76 + \dfrac{58.8}{Z^{.19}} & , \quad \text{otherwise.} \end{cases} \tag{7.16}$$

For compound materials a weighted sum was built to calculate dE/ds.

7.1.5 Fluorescence

For some of the photoabsorption events, a fluorescence photon is generated (cf. fig. 2.6(b)). The probability of this process depends on the absorbing element (cf. fig. 2.7). In these simulations, only K shell fluorescence is taken into account, since these photons have the highest yield. K_α photons have the highest energy. Thus, they can travel over relatively long distances, since their mean absorption length is quite large, and deposit their energy far away from the location of the primary beam. The angular distribution of the generated fluorescence photons is uniform over all angles.

To describe the absorption of the fluorescence photons, the same algorithm is applied that is used for the primary photons. Tabulated values are used for the fluorescence yield [60] and the photon energies [61]. For these photons, only photoelectrons are calculated in the simulations, which behave similar to those generated by the primary photons. Further cascading effects are not considered here. For the fluorescence photons K shell as well as L shell absorption is taken into account to allow reabsorption of the K_α photon in the substrate.

7.1.6 Auger electrons

For those absorption events, where no fluorescence photon is generated, an Auger electron is created (cf. fig. 2.6(c)). In this simulation, only (KLL) Auger electrons are taken into account, i. e., an electron from the L shell fills the hole in the K shell and another electron from the L shell leaves the atom as Auger electron. Thus, the energy of the Auger electrons results from the binding energies of the involved atomic shells. In this simulation is was calculated with

$$E_{\mathrm{KLL}} = E_b(\mathrm{K}) - 2E_b(\mathrm{L}), \tag{7.17}$$

where $E_b(\mathrm{K})$ is the binding energy of the K shell and $E_b(\mathrm{L})$ is the average of the binding energies of the L shell. The angular distribution of the Auger electrons

is uniform over all angles. The motion and the energy dissipation is treated with the same algorithm that is described above for the photoelectrons. The energy loss the collected in the same matrix.

7.2 Simulation results

7.2.1 Electron trajectories

When an electron-beam resist is used for x-ray lithography, the actual exposure is due to photo- and Auger electrons that are generated via photoabsorption in the sample. Since these electrons have a certain amount of energy, they can travel through the sample and deposit their energy via several scattering events.

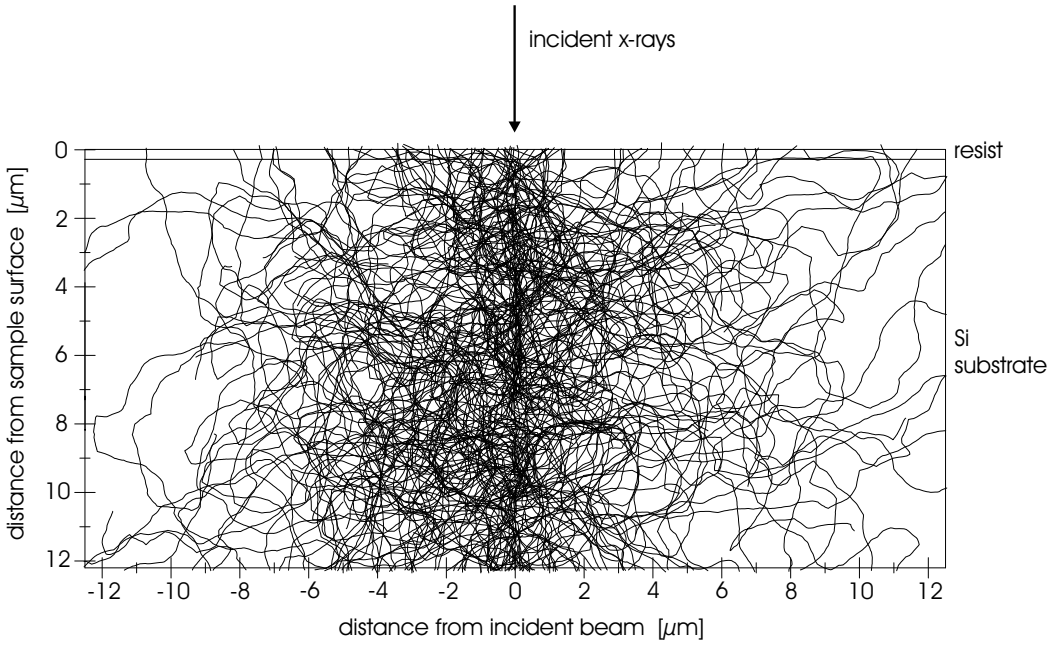

Figure 7.5: Trajectories of 300 photoelectrons from the primary photons in AR-N 7700.18 and silicon. The photon energy is 25 keV.

Figure 7.5 shows the trajectories of photoelectrons that are generated with the simulation model described above. The resist is AR-N 7700.18 with a layer thickness of 260 nm, and the substrate are 12 μm of silicon. The photon energy of the incident x-rays is 25 keV.

Most of the electrons that contribute to the exposure are generated in the substrate, since its absorption is significantly higher than that of the resist. They

have a high initial kinetic energy due to the high x-ray energy and the relatively low binding energy of the the K shell of silicon (1.8 keV). Thus, they can travel a long way through the sample, and even electrons that are generated a few micrometers away from the resist are able to reach and expose it. This often happens far away from the incident x-rays, resulting in a broadening of the features.

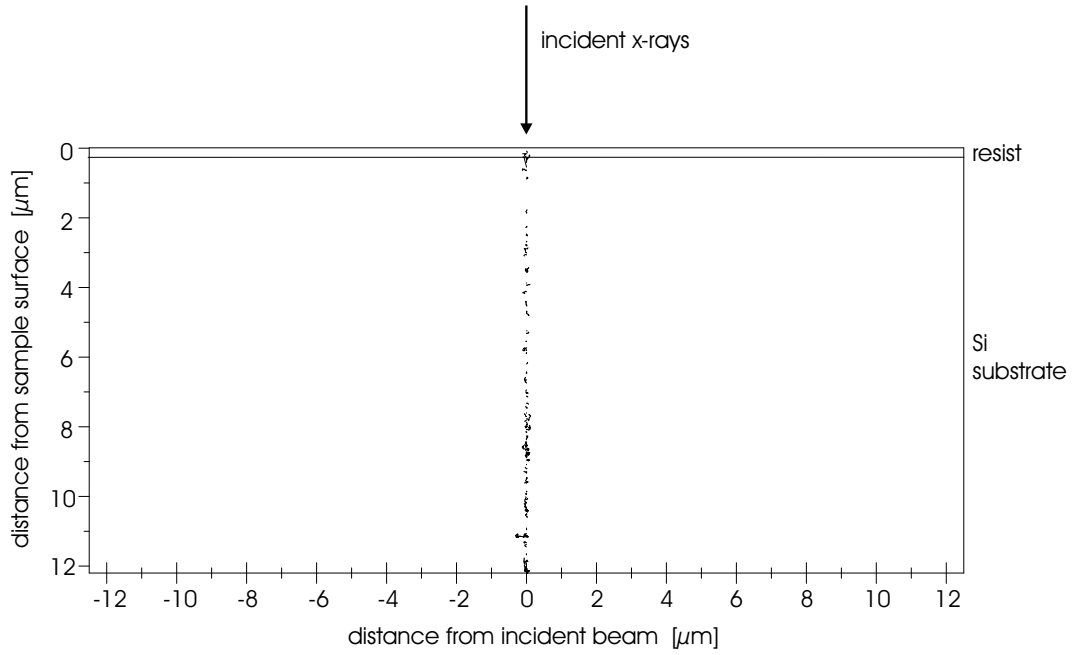

Figure 7.6: Trajectories of Auger electrons from the primary photons in AR-N 7700.18 and silicon. The photon energy was 25 keV.

Figure 7.6 show the Auger electrons that result from the same simulation as figure 7.5. They have a rather low kinetic energy, which is independent of the x-ray energy. They stay close to the point, where they are generated. Thus, they only expose the resist, when they are generated in the resist itself or very close to the surface. Compared to the photoelectrons, they have no noteworthy influence on the broadening of the linewidth.

7.2.2 Dose distribution in the resist

The exposure of the resist depends not only on the distance that the electrons can travel but also on the amount of energy that they deposit on a given spot.

Figure 7.7(b) shows the dose distribution in a resist that results from the electron trajectories shown above. The resist that is used for this simulation is the AR-N 7700.18 with a thickness of 260 nm, which matches the experiments described

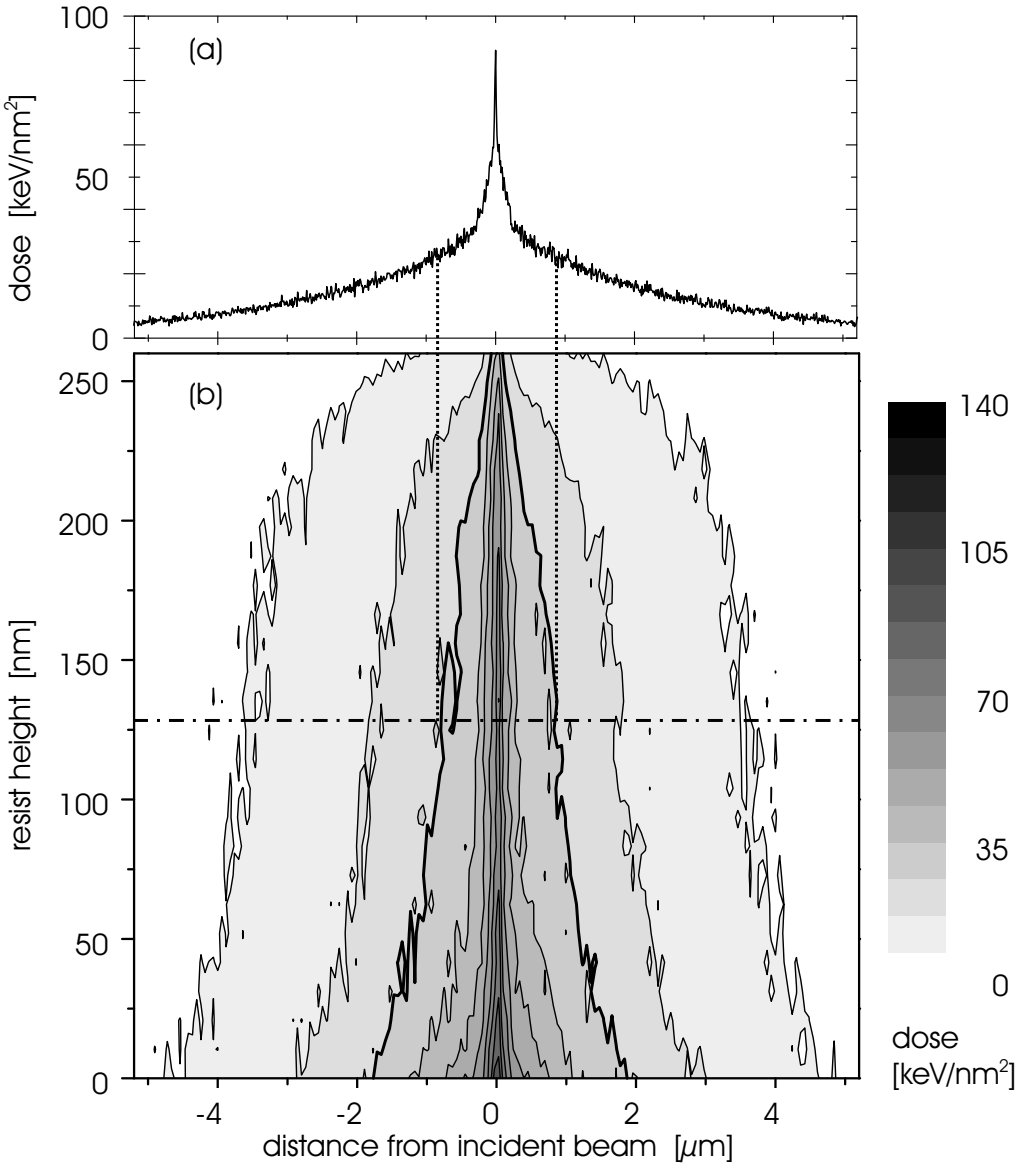

Figure 7.7: Dose distribution due to photoelectrons and Auger electrons which are created by the primary photon and photoelectrons created by fluorescence photons in AR-N 7700.18 as a result of an ideal thin x-ray beam coming from above. Fig. (b) shows a cross section through the resist, which contains the incident x-ray beam coming from above. At the lower end of the resist is a silicon substrate. Note the different scaling along abscissa and ordinate, the scale of the resist height being expanded by a factor of 40. The bold lines give the theoretical shape of the resist flanks after development. Fig. (a) shows the dose distribution along the dash-dotted line in (b). The dotted lines give the linewidth at that height.

in the previous chapter. 12μm of silicon are simulated as substrate. The scale of the resist height is expanded by a factor of 40 to better illustrate the distribution of the dose density over the resist height, since the width of the dose distribution reaches over several micrometers.

The dose distribution is significantly broader than the incident x-ray beam, which is an ideally thin line in this simulation. As can be seen from figure 7.7(a), the dose is largest along the path of the incident x-ray beam. Away from this path, there is still a significant amount of dose stored in the resist. While the dose distribution in figure 7.7(b) is rather uniform over most of the resist height, clear differences can be seen for the top of the resist layer and for its interface with the substrate. The dose at the top of the resist layer is below average, since the electrons that move around in this area have a chance of leaving the sample. Additionally, while in the middle of the resist layer the exposure is due to electrons that are created at this height as well as above and below this height, electrons coming from above can obviously not contribute to the exposure of the top of the layer. The influence of the electrons from the substrate, on the other hand, is most significant at the interface between resist and substrate and, thus, the exposure at the bottom of the resist layer is above average.

To completely expose the resist, the dose must exceed a minimum dose according to the sensitivity anywhere along the path of the incident beam. The bold lines in figure 7.7(b) are the lines of constant dose, which belong to the sensitivity. Thus, the resist between these two lines, where the dose exceeds the sensitivity, remains after the development, since the given resist AR-N 7700.18 is a negative resist. The rest, where the dose is lower than the sensitivity is washed away. Since the exposure is strongest at the interface between the resist and the substrate, the point where the dose exceeds the sensitivity is furthest away from the incident beam in this area. This results in a broadening of the resist features from the top to the bottom. In the case shown in figure 7.7, the 260 nm high resist line is broadened to almost 4 μm at the bottom.

7.2.3 Influence of photoelectrons

As can be seen from the trajectories in figure 7.5 and the dose distribution in figure 7.7, the most significant influence on the broadening of the exposed lines comes from the photoelectrons. The dependence of this influence on different parameters like photon energy or the chosen substrate will be discussed in the following.

In the following figures, the dose distribution is plotted along the interface between the resist and the substrate, since the dose distribution is broadest there due to the influence of the substrate. The curves are normalized to the minimum

dose along the path of the incident beam being 1, which takes the place of the sensitivity. Thus, the resist remains after development everywhere, where the normalized dose exceeds 1.

Energy of incident photons

The energy of the photoelectrons is the difference between the energy of the incident photon and the binding energy of the atomic shell the photoelectrons comes from (cf. eq. 7.8). Thus, it can be expected that the energy of the photoelectrons increases with increasing photon energy, since the binding energies of the involved atomic shells remains the same.

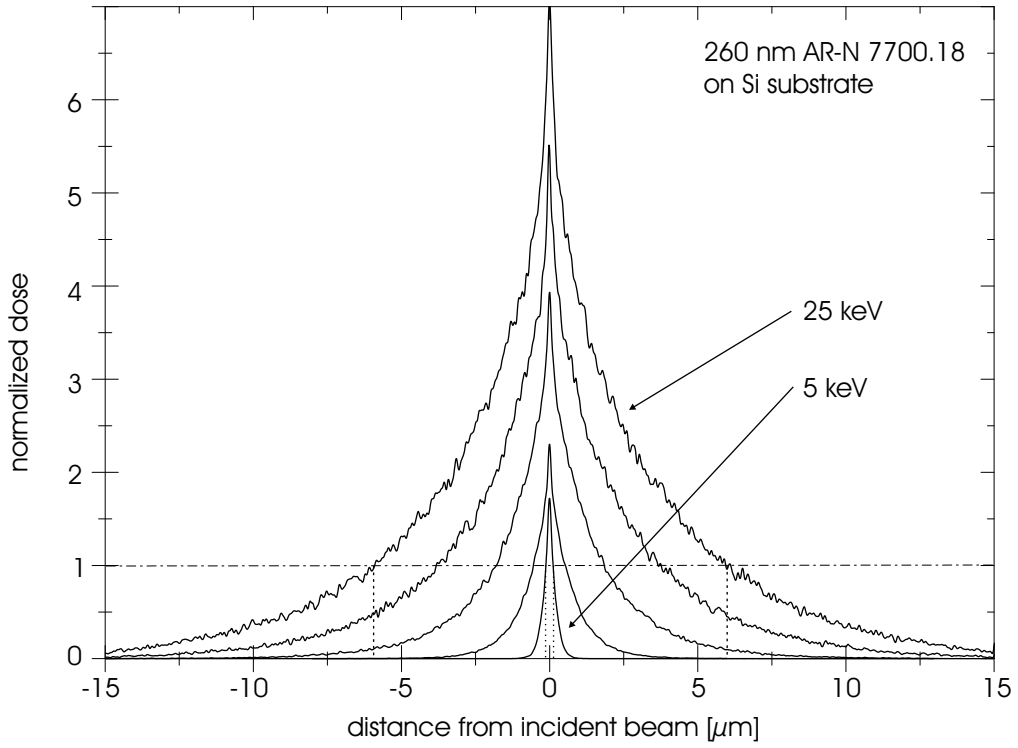

Figure 7.8: The plot shows the dose deposited in the resist at the interface to the substrate versus the distance from the incident photon beam for various photon energies. The photon energies from inside to outside are: 5, 10, 15, 20, and 25 keV. The dash-dotted line is at the sensitivity of the resist. The dashed lines mark the linewidth at 25 keV, the dotted lines at 5 keV.

Figure 7.8 shows the amount of energy that was deposited in a 1 nm thick slice of the resist next to the resist-substrate interface from the photoelectrons, which

are created by an ideal x-ray beam perpendicular to the surface. The dose is normalized to 1 being the minimum dose along the path of the incident beam. This dose must exceed the sensitivity, so that the resist can be exposed completely over its full height. Since the exposure is strongest at the bottom of the resist, the dose at the place of the incident beam is higher than 1 and sinks below 1 at some point away from the beam, which gives the width of the developed resist line at the bottom.

The resist used in these simulations is the AR-N 7700.18, which was used in the experiments described in the previous chapters. The layer thickness is 260 nm, which also corresponds to the experiment, on a silicon substrate with a thickness of 12 μm. The different photon energies are 5, 10, 15, 20, and 25 keV.

The different lines show an increasing maximum height with increasing photon energy due to the fact that the overexposure at the resist-substrate interface increases. The widths for a normalized dose of 1 are 0.2, 1.1, 3.6, 7.5 and 11.8 μm with increasing photon energy.

Thus, the use of lower photon energies would reduce the broadening due to photoelectrons. The main reason, why these high energies were chosen for the experiments described in the previous chapter, was the use of the aluminium PRXL, which work best at energies around 20 or 25 keV. The use of other lens materials, however, could allow the use of lower photon energies, which result in a lower energy of the photoelectrons and, thus, a smaller linewidth and a lower overexposure at the bottom of the resist. Beryllium, for example, would be of interest for energies down to about 8 keV. For low photon energies other optics like Fresnel zone plates are also of interest.

Different substrates

As has been discussed above, the photoelectrons that expose the resist come from the substrate. The influence of different substrate materials will therefore be investigated in the following.

Figure 7.9 shows the dose, which is deposited in a 1 nm thin slice of the resist layer by photoelectrons, with respect to the distance perpendicular to the incident beam. For resist layers, which are on top of a substrate, the slice nearest to the resist-substrate interface is shown, since the dose distribution is broadest there. For the free-standing resist layer without substrate, the dose distribution is broadest in the middle of the layer and is thinner at the top and bottom. The curves are normalized to 1 being the minimum dose along the path of the incident beam. Thus, the resist remains after the development, where the dose is larger than 1, since a negative resist is discussed here, while the rest is taken away.

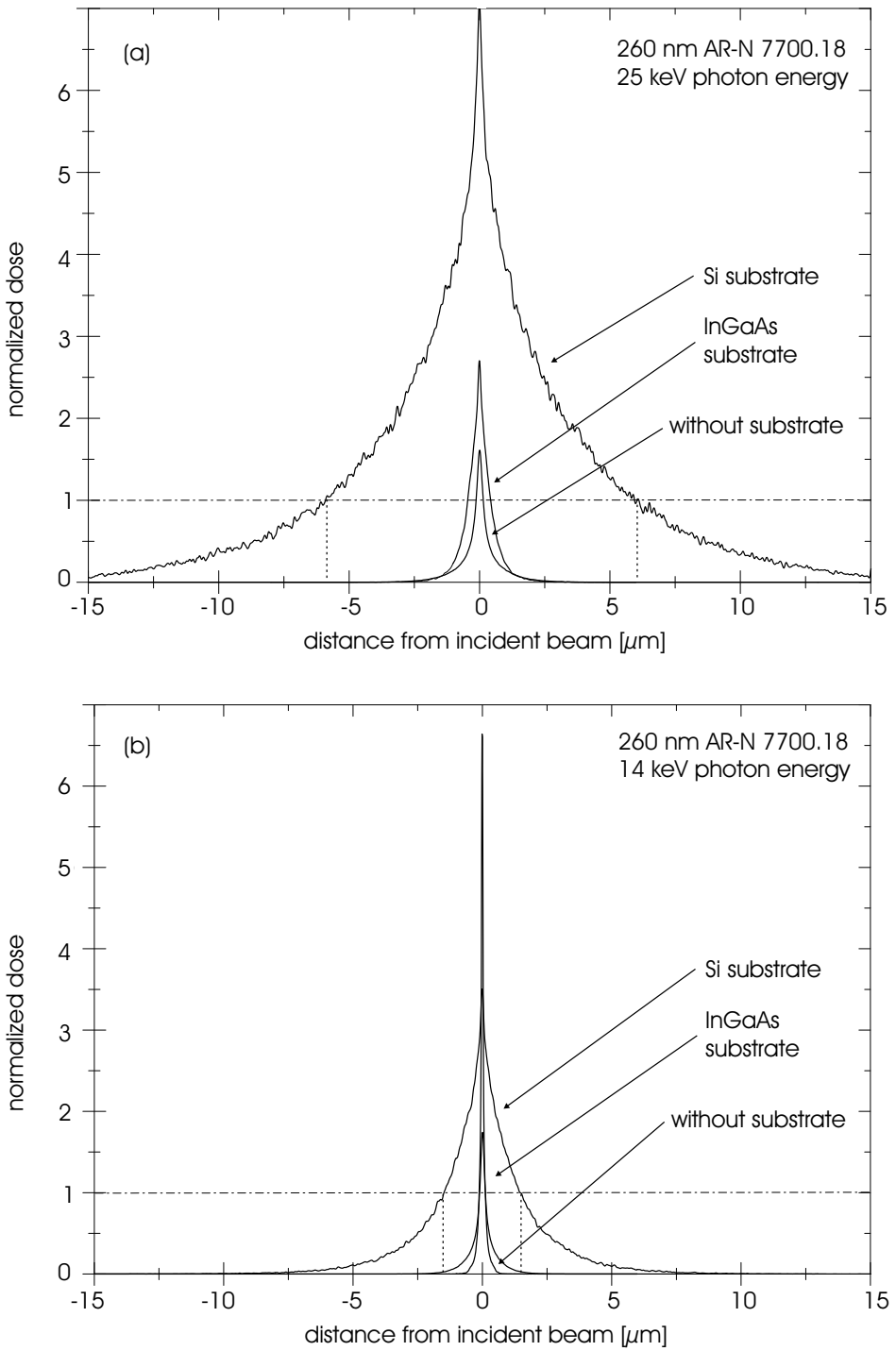

Figure 7.9: The dose deposited at the bottom of the resist layer for different substrates and in the middle of a resist layer without substrate versus the distance from the incident beam (a) for 25 keV and (b) for 14 keV photons. The dash-dotted line gives the sensitivity of the resist; the dashed lines give the width for the Si substrate.

The resist is the AR-N 7700.18 with a thickness of 260 nm. The incident photons have an energy of 25 keV in figure 7.9(a) and and energy of 14 keV in figure 7.9(b). The substrate thicknesses are 12 μm for the silicon substrate and 500 nm for the $In_{0.52}Ga_{0.48}As$ substrate, respectively. In these cases, the dose distribution is broadest at the resist-substrate interface. For comparison, a free-standing resist layer was also simulated. Here, the distribution is broadest in the middle of the layer.

As can be seen in figure 7.9, the different substrates lead to very different linewidths. For 25 keV(cf. fig. 7.9(a)), the linewidths are 11.8 μm for the silicon substrate, 0.87 μm for the $In_{0.52}Ga_{0.48}As$ substrate, and 0.26 μm for the free-standing resist layer. The overexposure due to the Si substrate is significantly larger than that due to the $In_{0.52}Ga_{0.48}As$ substrate. For 14 keV(cf. fig. 7.9(b)), the linewidths are 2.9 μm for the Si substrate, 0.24 μm for the $In_{0.52}Ga_{0.48}As$ substrate, and 0.22 μm for the free-standing resist layer. In this case, the overexposure due to the silicon substrate is lower than that due to the $In_{0.52}Ga_{0.48}As$. The overexposure in the middle of the free-standing resist layer as compared to the exposure at top and bottom is the same in both cases.

This predominant effect of the substrate on the linewidth results from the high absorption in substrate compared to that of the resist. This is due to the fact that a typical resist is composed of rather light elements like carbon and has a mass density of only about 1×10^3 kg/m^3. To reduce the influence of the substrate on the lithographic process, it is, thus, necessary to either increase the absorption of the resist at high photon energies or to decrease the absorption in the substrate. Since the substrate material or a buffer layer between the resist and the actual substrate can not always be chosen freely for a lithographic process, the best choice will be to adjust the resist for a given photon energy. Some examples for this will be shown in the following chapter.

7.2.4 Influence of Auger electrons

As has been described in chapter 2, the generation of a photoelectron is accompanied by the generation of either a fluorescence photon or an Auger electron. Higher orders of the energy cascade are neglected. For elements with a low atomic number Z, the fluorescence yield is negligible and almost only Auger electrons are generated, as can be seen from figure 2.7. The energy of the Auger electrons does not depend on the energy of the absorbed photon, but only on the binding energy of the atomic shells that take part in the process. Thus, it increases with increasing atomic number.

Figure 7.10 shows the exposure of the resist at the resist-substrate interface due to Auger electrons with respect to the distance from the incident beam. The

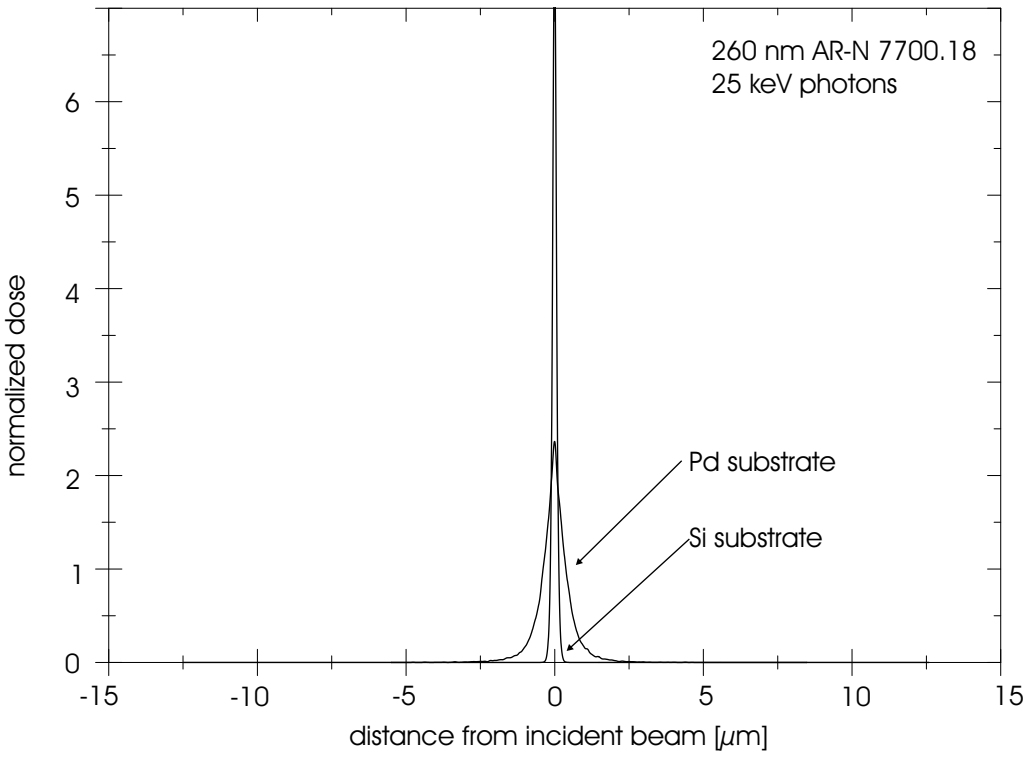

Figure 7.10: Dose distribution due to Auger electrons generated by the primary photons vs. distance from the incident beam for AR-N 7700.18 on a Si and a Pd substrate, respectively.

simulations are done for 260 nm of AR-N 7700.18 on a silicon substrate of 12 μm thickness and a palladium substrate of 500 nm thickness, respectively. The distributions are normalized to 1 being the minimum dose along the path of the incident beam, which has to exceed the sensitivity of the resist to completely expose it.

Since the fluorescence yield in Silicon is only about 5 % and even less in the lighter elements, almost every photoabsorption results in an Auger electron. However, only those Auger electrons can contribute to the exposure of the resist that are generated in the resist itself and in those parts of the substrate that are close to the interface, since their kinetic energy is relatively small. With increasing atomic number Z of the absorber, the kinetic energy of the Auger electrons increases also and with it the dose distribution in the resist, as is shown in figure 7.10 for a palladium substrate as an example. At the same time, the Auger electron yield decreases, as can be seen from figure 2.7. Thus, the Auger electrons from the palladium substrate, which are responsible for the boarder peak in figure 7.10, do

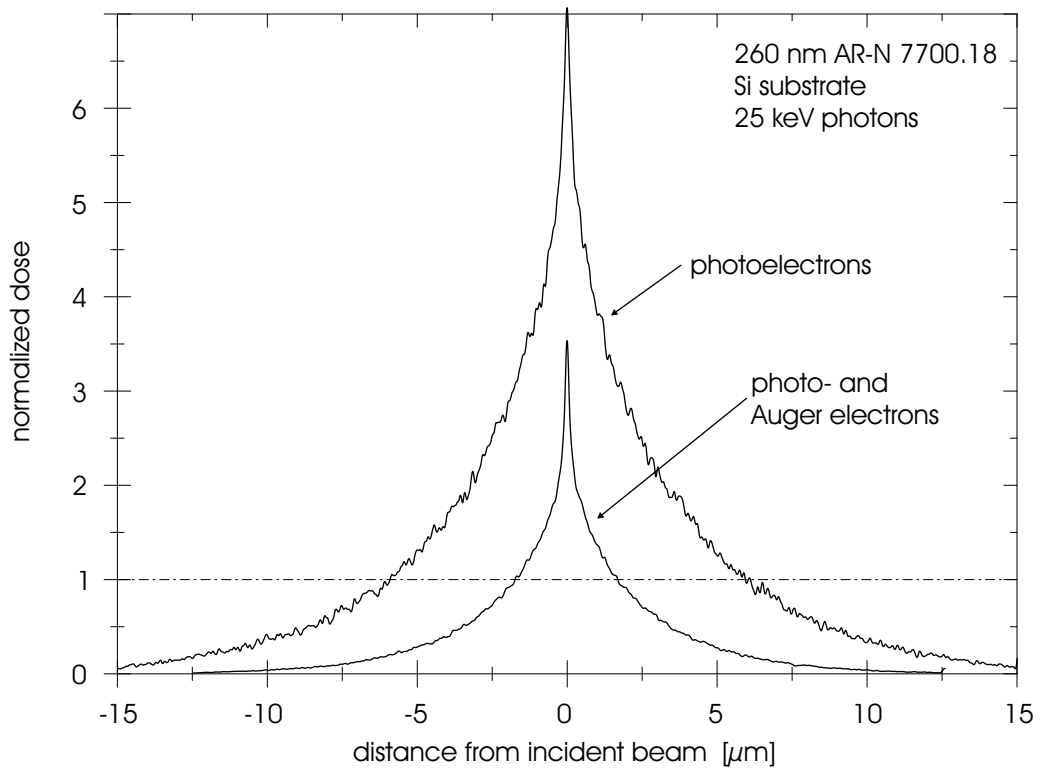

Figure 7.11: Absorbed energy in the resist layer versus the distance from the incident due to photoelectrons only and due to both photo- and Auger electrons. The sample is AR-N 7700.18 on silicon, and the photon energy is 25 keV.

not significantly contribute to the exposure of the resist, since the fluorescence yield for palladium is already over 80 %.

For this reason, only Auger electrons from light absorbers, which have low kinetic energies, contribute to the exposure of the resist. But, since they do not travel far from the incident beam, they increase the exposure in the center of the line and, thus, can counteract the broadening due to the far traveling photoelectrons. This effect is depicted in figure 7.11 for 260 nm of AR-N 7700.18 on 12 μm of silicon. The photon energy is 25 keV. The curves are normalized to 1 being the sensitivity. The linewidths are 11.8 μm, when only photoelectrons are taken into consideration, and 3.4 μm, when both photo- and Auger electrons are taken into account.

7.2.5 Influence of fluorescence

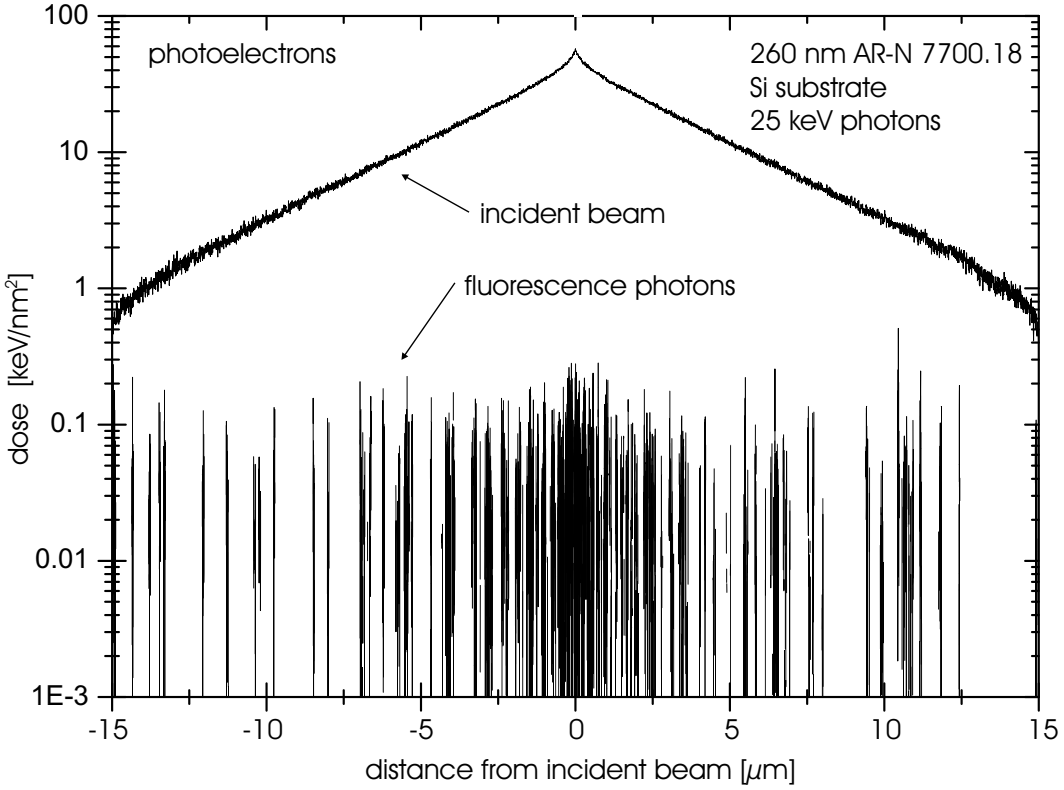

Figure 7.12: Dose distribution by to photoelectrons due to the incident beam and due to fluorescence photons. The doses are summed up over the resist height.

As can be seen from figure 2.7, the fluorescence yield depends on the atomic number Z of the absorbing atom. Light elements show almost no generation of fluorescence photons. The emission of these photons is uniform over all angles. Thus, the amount of fluorescence photons that is absorbed in the resist or close enough to the resist-substrate interface, so that the generated electrons can expose it, is negligible as can be seen from figure 7.12. Here, the dose distributions are shown that result from the photoelectrons due to the incident beam and due to the fluorescence photons. The doses are summed up over the resist height. The exposure due to the photoelectrons from the incident beam is almost three orders of magnitude larger than the exposure due to the fluorescence photons.

Chapter 8

Outlook

As can be seen from the previous chapters, the demagnifying x-ray lithography with parabolic refractive x-ray lenses (PRXL) works in principle. The use of high photon energies is of special interest for the deep x-ray lithography, since the low absorption allows a rather uniform exposure of very thick resist layers. But it also implies thick mask absorbers, which raise problems in the generation of small mask features. The use of a demagnifying optic instead of proximity lithography might be able to ease a further miniaturization in this field. This approach is planned for further investigation in a collaboration with Dr. S. Achenbach of the Forschungszentrum Karlsruhe. The limitations in the field of view that arise from the small spot size of an undulator source can be addressed by a mixture of stepping and scanning, as it is also discussed for the EUV lithography. In EUV lithography, however, the field of view to start with is significantly larger.

But the first tests of the demagnifying x-ray lithography with PRXL showed significant problems, mainly due to the use of high energy photons and the photoelectrons generated by them. In this chapter some improvements will be described, that will be applied in the near future.

8.1 Different lenses

The aluminium lenses, that are described in chapter 3 and are used in these experiments, work best at about 20 or 25 keV. Another material, which is interesting for parabolic refractive x-ray lenses, is beryllium. Here, photon energies between 10 and 15 keV are of interest, which would result in a higher absorption of the resist and, thus, would reduce the exposure times as well as the needed thickness of the mask absorber.

Since the mass absorption coefficient μ/ρ of beryllium is smaller than that of aluminium, these lenses will have a higher transmission and with that a larger field of view and a higher resolution [62]. Due to the higher transmission the exposure times would be reduced further.

8.2 Adjusting the resists

As has been shown in the previous chapter, the secondary electrons from the substrate have a great influence on the quality of the lithographic structures due to the proximity effect.

A drawback of the use of commercially available electron-beam resists in the x-ray lithography with high energy photons is the poor sensitivity of these resists, which results in long exposure times. The reason for this behavior is the typical composition of these resists, which primarily consist of light elements like carbon, hydrogen, and oxygen that have a very low absorption at high photon energies.

The major role of the secondary electrons from the substrate in exposing the resist is directly connected with the very poor absorption of the resist itself. Thus, increasing the absorption of the resist would be a way to reduce the influence of the substrate. This can be done by adding heavier atoms to the resist [63].

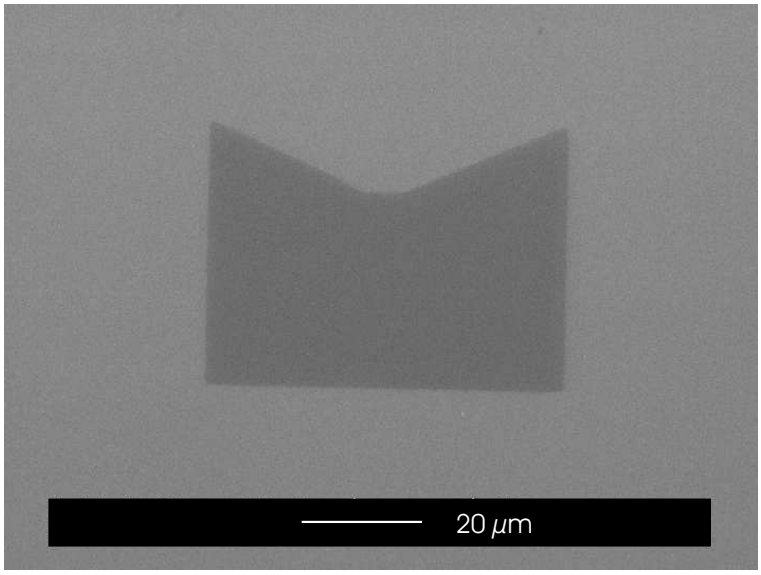

Figure 8.1: Micrograph of a electron beam lithography test structure on a silicon substrate generated in AR-N 7700.18 with 16 % palladium acetate

One possibility of adding heavier atoms to a resist is to mix a normal resist with an organic salt of a metal. For the use with 25 keV photons, palladium is an interesting candidate, since its K absorption edge is at 24.35 keV. A mixture of a standard electron beam resist with palladium acetate has already been produced in collaboration with Allresist, GmbH. So far, it only has been tested successfully in electron beam lithography, of which an example is shown in figure 8.1. The micrograph shows a resist structure on a silicon substrate, which was generated via electron-beam lithography. In this situation, it works similar to the undoped resist. Simulations show indeed that this concept is promising for the use with x-ray lithography.

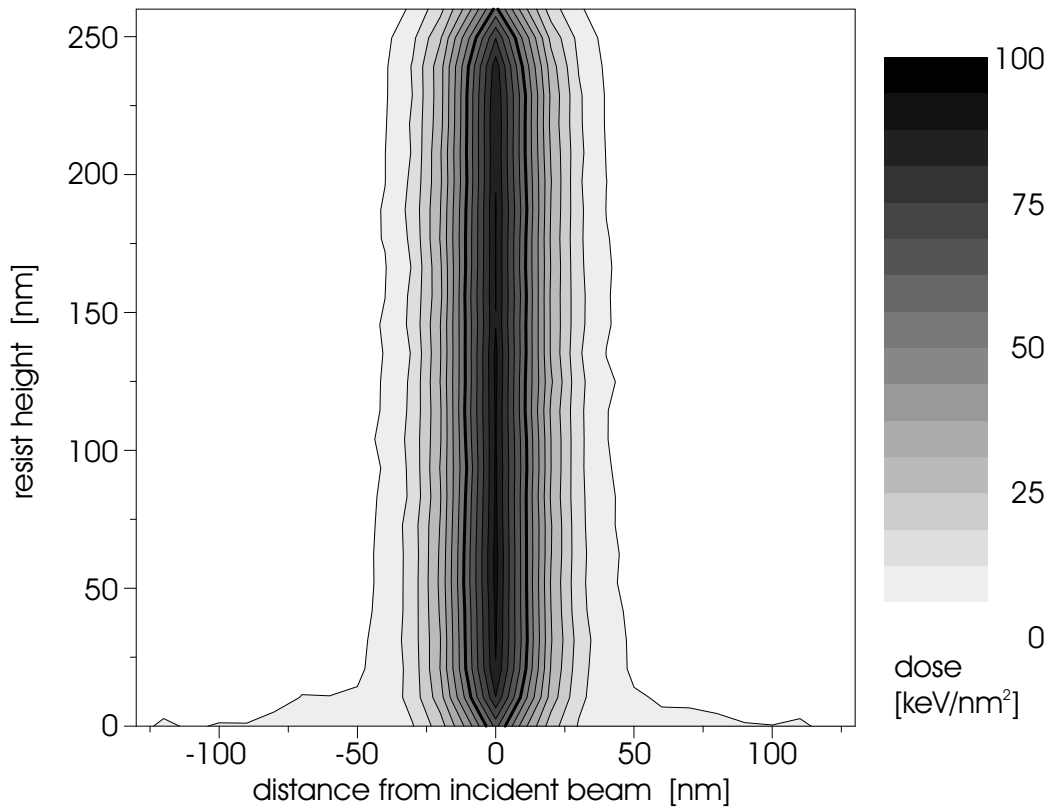

Figure 8.2: Dose distribution in the palladium doped AR-N 7700.18 on a silicon substrate for a photon energy of 25 keV. The shown section is 260 nm×260 nm. The bold lines give the theoretical shape of the resist flanks after the development.

Figure 8.2 shows a cross-section of the dose distribution in the palladium doped AR-N 7700.18 on 12 μm silicon. The photon energy is 25 keV. The exposure is rather uniform over the resist height. The bold lines in this plot are lines of constant dose belonging to the minimum dose, which is necessary to exposure

the resist. This dose must be exceeded everywhere along the path of the incident beam to completely expose the resist over its full height. These lines give the theoretical shape of the resist line after the development. Since it is difficult for the developer to underetch the resist at the bottom of the structures, the real shape will probably not follow the bold lines in this area, since the theoretical line gets narrower at the resist-substrate interface. The broadening due to substrate can only be seen at the bottom of the resist and is of a significantly lower intensity than the line itself. The higher absorption of the resist also reduces the exposure time, since the dose generated from the same number of photons is higher than in the undoped resist.

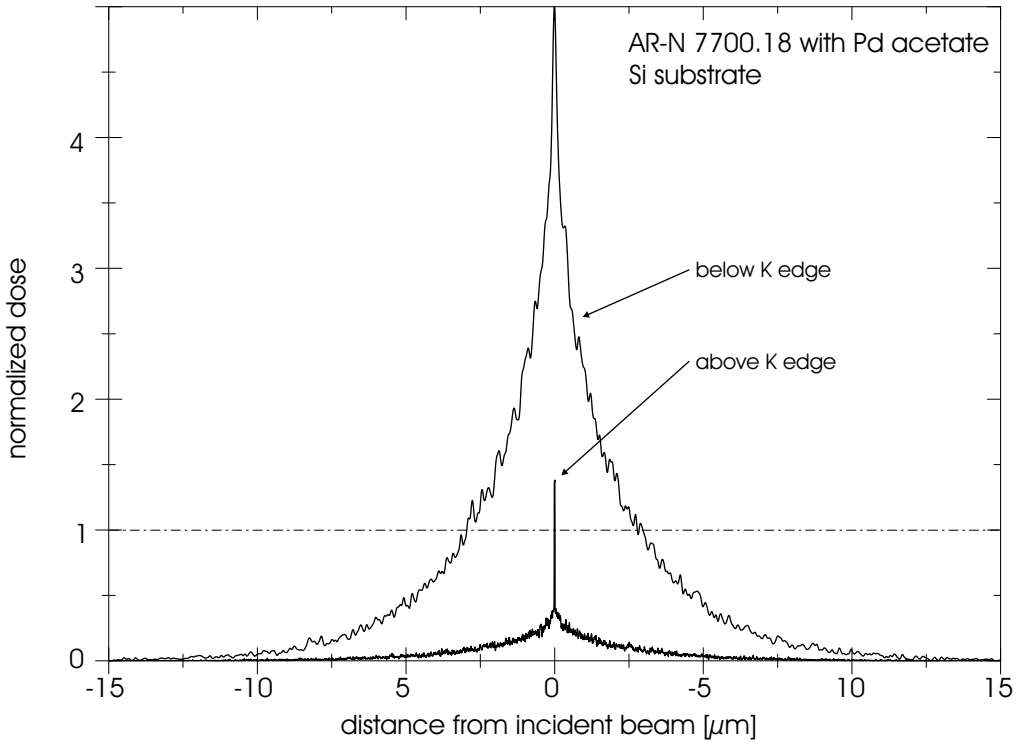

Figure 8.3: Dose distribution due to photoelectrons at the bottom of the resist structure in the palladium doped resist for photon energies of 50 eV above and below the palladium K edge. The dash-dotted line gives the sensitivity of the resist.

Figure 8.3 clarifies the influence that the low energetic photoelectrons from the palladium have on the broadening of the linewidth. The simulations show the dose distribution due to photoelectrons for photon energies of 50 eV above and below the palladium K-edge (24.35 keV), respectively. The simulated resist was a 260 nm thick layer of AR-N 7700.18 with 16 % palladium acetate, as it is

described above. The substrate is silicon with a thickness of 12 μm. The curves are normalized to 1 being the minimum dose along the path of the incident beam. The linewidths that result from the fact that the resist is removed in the developer at those points ,where the normalized dose is smaller than 1, are 5.7 μm for the exposure below the K-edge and 13 nm above the K-edge, respectively. The reason for the extreme difference is that the palladium does barely absorb x-rays with energies below its K-edge and, thus, the high energetic electrons from the other elements in the resist and substrate lead to the broadening of the line. For photon energies above the K-edge, however, the palladium dominates the absorption and, thus, its low energetic photoelectrons define the linewidth.

Figure 8.4(a) compares simulations of the dose distribution at the bottom of the resist layer for the standard resist and a mixture of the same resist with 16 % palladium acetate. The resist parameters are the ones for the AR-N 7700.18 by Allresist GmbH, which was used for the experiments in the prior chapters. The substrate is silicon with a thickness of 12 μm. The photon energy is 25 keV. The curves have been normalized to 1 on being the minimum dose along the path of the incident beam so that the resist will be exposed completely along the path of the incident beam. The linewidth for the standard resist is 11.8 μm, while it is only 54 nm in the palladium doped resist.

Another way of increasing the absorption of the resist would be to directly include elements with interesting absorption edges into the manufacturing process and, thus, into the resist polymers themselves. AR-N 7700.18 contains chlorine, which could be substituted by any other halogen. Bromine, for example, has its K-edge at 13.47 keV, and is, thus, interesting for the use with the beryllium lenses described above.

Figure 8.4(b) shows the dose distribution at the bottom of the layer for this bromine doped AR-N 7700.18 in comparison to the undoped resist at a photon energy of 14 keV. A silicon substrate with a thickness of 12 μm is simulated, the resist layers have a thickness of 260 nm. The curves are normalized to 1 being the minimum dose along the path of the incident beam. The linewidth at the bottom of the resist structure is 2.9 μm for the standard resist, while it is 27 nm for the bromine doped resist.

The main advantage of a resist with a high absorption is the reduction of the influence of the secondary electrons from the substrate, as can be seen in figure 8.5 for the palladium doped and the bromine doped AR-N 7700.18 described above on different substrates. The substrates are silicon with a thickness of 12 μm and $In_{0.52}Ga_{0.48}As$ with a thickness of 500 nm. A free-standing resist layer is given for comparison. The curves are normalized to 1 being the minimum dose along the path of the incident beam.

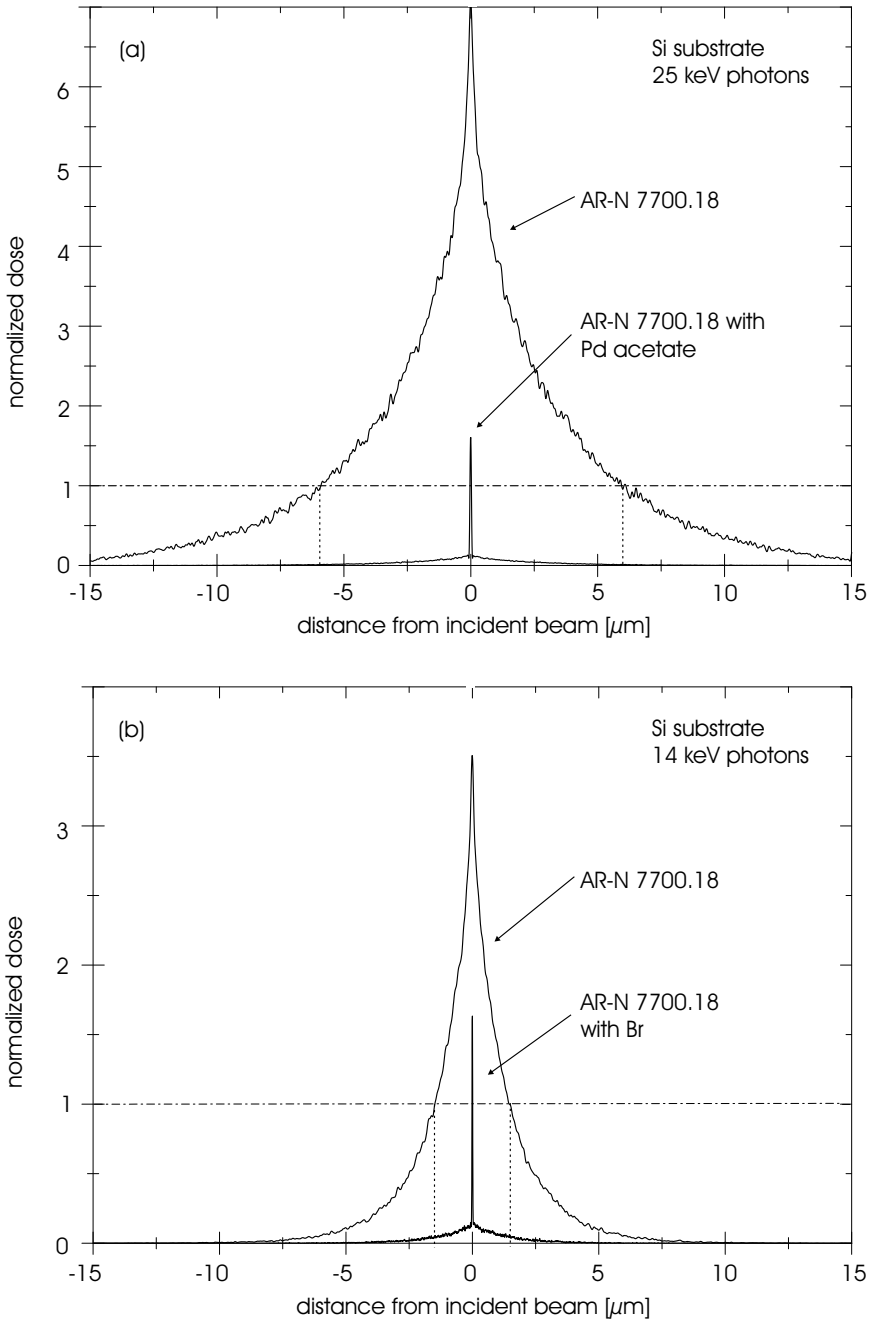

Figure 8.4: Dose distributions due to photoelectrons at the bottom of the resist structure for (a) the AR-N 7700.18 with Pd acetate at 25 keV and (b) the AR-N 7700.18 with Br at 14 keV. The curves for the undoped AR-N 7700.18 are given for the respective energies for comparison. The curves are normalized to one being the sensitivity of the resist.

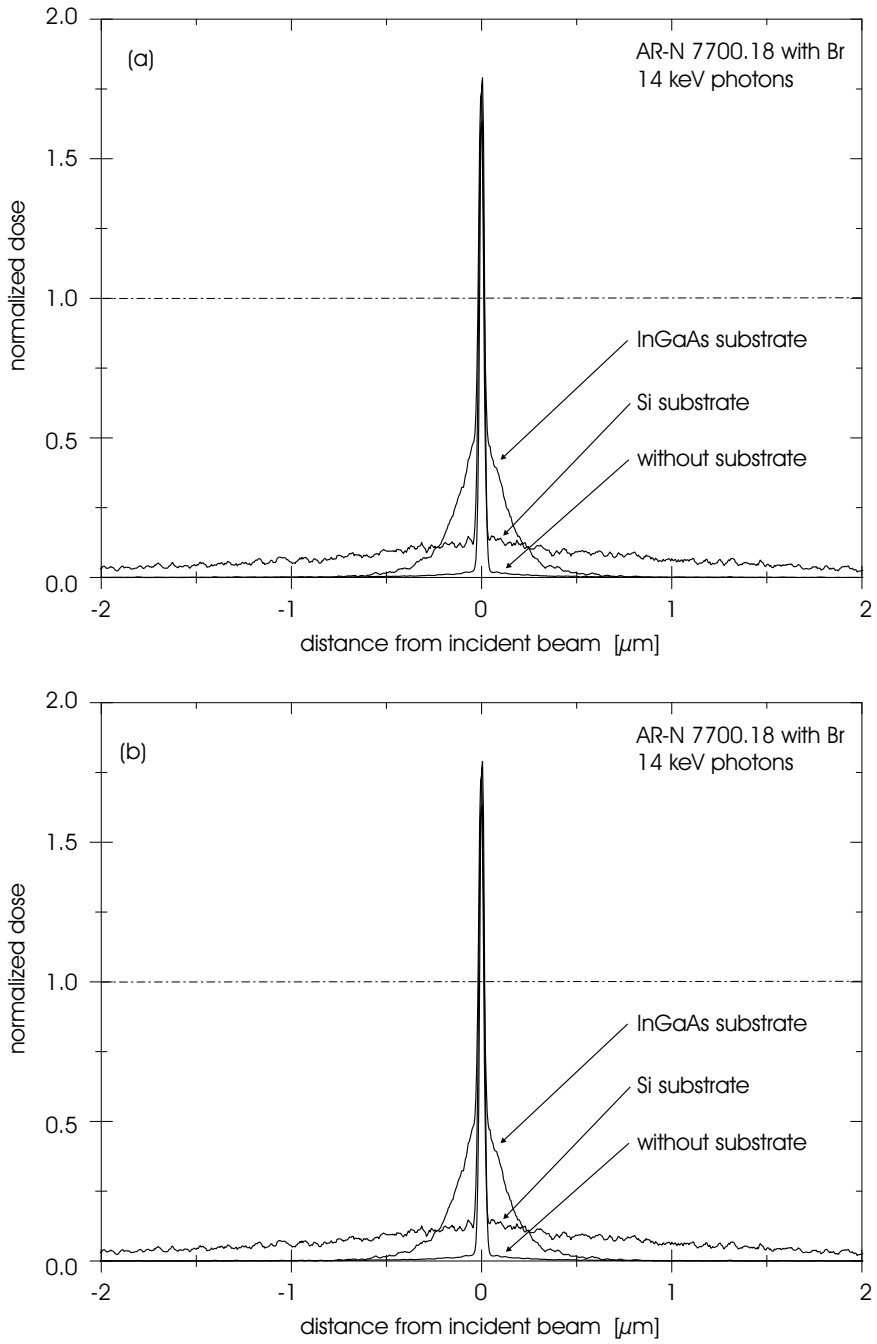

Figure 8.5: The amount of absorbed energy in the resist layer versus the distance from the incident beam for (a) a palladium doped resist on different substrates at a photon energy of 25 keV and (b) a bromine containing resist on different substrates at a photon energy of 14 keV.

Figure 8.5(a) shows the simulations for the palladium doped AR-N 7700.18, which are done at photon energies of 25 keV. The linewidths are 29 nm for the free-standing resist layer, 54 nm for the silicon substrate, and 67 nm for the $In_{0.52}Ga_{0.48}As$ substrate. The curves in figure 8.5(b) show the simulations for the bromine doped resist and are done at photon energies of 14 keV. The linewidths are 26 nm for the free-standing resist layer, 27 nm for the silicon substrate, and 34 nm for the $In_{0.52}Ga_{0.48}As$ substrate. The respective curves for the undoped resist can be seen in figure 7.9.

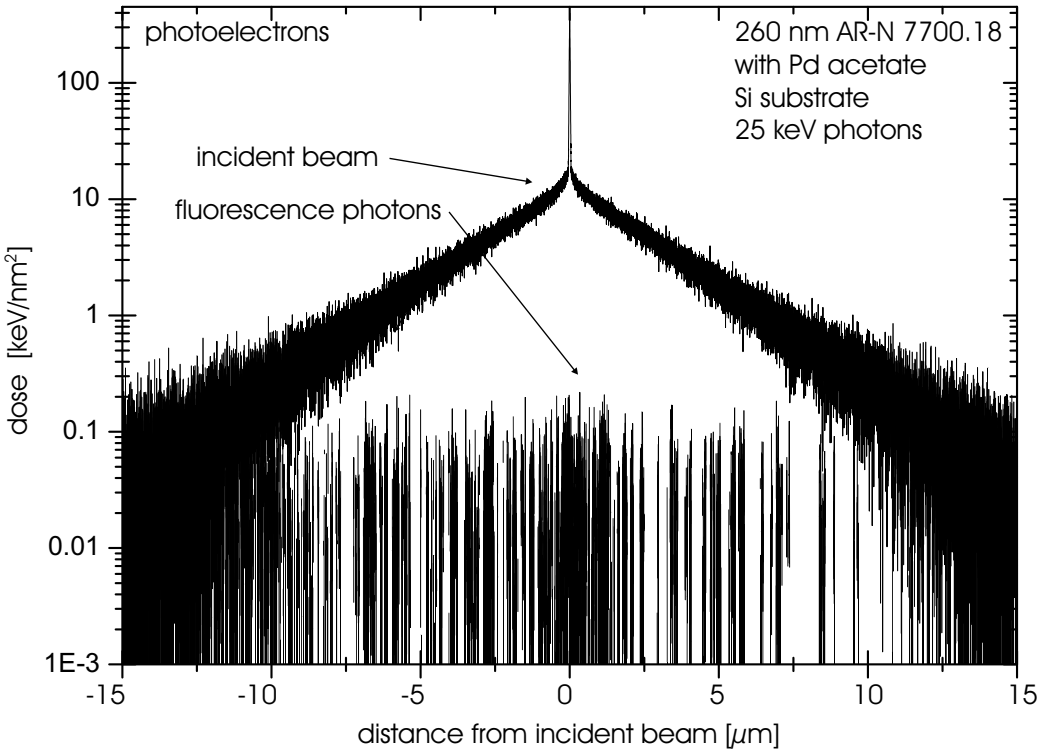

Figure 8.6: Dose distribution in the palladium doped AR-N 7700.18 by photoelectrons due to the incident beam and due to fluorescence photons at a photon energy of 25 keV. The dose is summed up over the resist height.

When atoms with a high atomic number Z are contained within the sample, the number of generated fluorescence photons increases, as can be seen in figure 2.7. Figure 8.6 compares the dose distribution due to photoelectrons generated by the incident beam with the distribution due to photoelectrons generated by fluorescence photons. The doses are summed up over the resist height. Since the doses that result from the fluorescence photons are significantly lower than the peak due to the incident beam, which is responsible for the exposure of the resist, the contribution of the fluorescence photons can be neglected.

Thus, the simulation results are very promising concerning the generation of thin resist patterns. These very thin linewidths, however, will be superposed in the demagnifying experiments with the diffraction limited spot size, which is about 80 nm for the beryllium lenses described above [6].

Chapter 9

Summary

In this thesis, a concept for a demagnifying lithography setup using hard x-rays was presented. The parabolic refractive x-ray lenses (PRXL) that have so far been applied to a wide variety of imaging tasks are used to generate demagnified images not only on a CCD camera but also in lithographic resists. The demagnification factors realized in these experiments were 2.8 and 4.1, but larger values are also easily achievable with this setup.

In a first experiment at the ESRF in Grenoble, the demagnifying lithography with hard x-rays was demonstrated. A commercially available negative tone electron beam resist was used for the exposures. The experiments showed

- that lithography works in principle (Fig. 6.5, p. 49),
- that the Gaussian profile of the beam also appears in the resist profile (Fig. 6.6, p. 51), so that larger structures have to be exposed with a scanning setup to achieve a homogeneous exposure,
- that the development parameters influence the contrast of the lithography (Fig. 6.7, p. 53),
- but that the resist edges smear out over several micrometers (Fig. 6.8, p. 54).

This last item is a major problem when it comes to the application of this method for small feature sizes. Using Monte Carlo simulations, it was shown that these effects are due to the generation of high energy photoelectrons in the substrate.

The simulations showed

- that the features are broadened most at the interface between resist and substrate (Fig. 7.7, p. 68),

- that the broadening increases with increasing photon energy up to several micrometers (Fig. 7.8, p. 70),
- that the broadening varies with the chosen substrate material, since the absorption in the resist itself is very weak (Fig. 7.9, p. 72),
- and that the influence of Auger electrons (Fig. 7.6, p. 67) and fluorescence photons (Fig. 7.12, p. 76) can be neglected compared to the broadening due to photoelectrons from the primary beam (Fig. 7.5, p. 66).

Based on these results, design concepts for resists especially for the use with hard x-rays are discussed. Adding heavy atoms, whose K-edge is just below the photon energy of the x-rays, to the resist increases the absorption in the resist. The simulations of these new resist designs showed

- that the resist patterns become considerably smaller and more uniform over the resist height (Fig. 8.2, p. 79)
- and that the influence of the substrate material disappears (Fig. 8.5, p. 83).

Thus, the influence of photoelectrons from the substrate is significantly reduced. Furthermore, the energy of the photoelectrons from these heavy atoms is very low compared to those from light atoms. This results in linewidths down to a few 10 nm, since the range of the photoelectrons is reduced to this order of magnitude.

For a future performance increase, it is planned to use a variety of resists that are doped with different heavy atoms for different photon energy regimes. One example, a mixture of a commercial electron-beam resist with palladium acetate, has already been made and tested in electron-beam lithography. It is designed for the use with photon energies around 25 keV. Furthermore, the use of beryllium lenses is planned, which have a larger aperture and a higher transmission. This results in a larger field of view and a shorter exposure time due to a higher flux on the sample.

List of Figures

Bibliography

[1] International roadmap for semiconductors, public.itrs.net.

[2] W. C. Röntgen. Ueber eine Neue Art Von Strahlen (3. Mittheilung). *Annalen der Physik und Chemie Neue Folge*, 64:1, 1898.

[3] A. Snigirev, V. Kohn, I. Snigireva, and B. Lengeler. A compound refractive lens for focusing high-energy x-rays. *Nature*, 384:49 – 51, 1996.

[4] B. Lengeler, C. G. Schroer, M. Richwin, J. Tümmler, M. Drakopoulos, A. Snigirev, and I. Snigireva. A microscope for hard x rays based on parabolic compound refractive lenses. *Applied Physics Letters*, 74(26):3924 – 3926, 1999.

[5] B. Lengeler, C. Schroer, J. Tümmler, B. Benner, M. Richwin, A. Snigirev, I. Snigireva, and M. Drakopoulos. Imaging by parabolic refractive lenses in the hard x-ray range. *Journal of Synchrotron Radiation*, 6:1153 – 1167, 1999.

[6] J. Tümmler. *Development of Compound Refractive Lenses for Hard X-Rays.* PhD thesis, University of Technology Aachen, 2000.

[7] B. Lengeler, C. G. Schroer, B. Benner, T. F. Günzler, M. Kuhlmann, J. Tümmler, A. S. Simionovici, M. Drakopoulos, A. Snigirev, and I. Snigireva. Parabolic refractive x-ray lenses: A breakthrough in x-ray optics. *Nuclear Instruments and Methods on Physics Research A*, 467 – 468:944 – 950, 2001.

[8] C. G. Schroer, T. F. Günzler, B. Benner, M. Kuhlmann, J. Tümmler, B. Lengeler, C. Rau, T. Weitkamp, A. Snigirev, and I. Snigireva. Hard x-ray full field microscopy and magnifying microtomography using compound refractive lenses. *Nuclear Instruments and Methods in Physics Research A*, 467 – 468:966 – 969, 2001.

[9] C. G. Schroer, B. Benner, T. F. Günzler, M. Kuhlmann, C. Zimprich, B. Lengeler, C. Rau, T. Weitkamp, A. Snigirev, I. Snigireva, and J. Ap-

penzeller. High resolution imaging and lithography with hard x rays using parabolic compound refractive lenses. *Review of Scientific Instruments*, 73(3):1640 – 1642, 2002.

[10] C. G. Schroer, J. Meyer, M. Kuhlmann, B. Benner, T. F. Günzler, B. Lengeler, C. Rau, T. Weitkamp, A. Snigirev, and I. Snigireva. Nanotomography based on hard x-ray microscopy with refractive lenses. *Applied Physics Letters*, 81(8):1527 – 1529, 2002.

[11] Homepage of the ESRF in Grenoble, France (www.esrf.fr).

[12] K. Wille. *Physik der Teilchenbeschleuniger und Synchrotronstrahlungsquellen*. Teubner Studienbücher, 1996.

[13] B. Lengeler. European synchrotron radiation facility ESRF, Grenoble. In *27. IFF-Ferienkurs*. FZ Jülich, 1996.

[14] C. Rau, T. Weitkamp, A. Snigirev, C. G. Schroer, J. Tümmler, and B. Lengeler. Recent developments in hard x-ray tomography. *Nuclear Instruments and Methods in Physics Research A*, 467 – 468:929 – 931, 2001.

[15] W. J. Veigele. Mass attenuation and absorption cross sections for 94 elements; 0.1 keV to 1 MeV. In J. W. Robinson, editor, *Vol. I of Handbook of Spectroscopy*, volume I, chapter 3, pages 28 — 154. CRC Press, Inc., Boca Raton, Florida 33431, USA, 1980.

[16] I. S. Girgoriev and E. Z. Meilikhov, editors. *Handbook of Physical Quantities*. CRC Press, Boca Raton, New York, London, Tokyo, 1997.

[17] R. W. James. *The Optical Priciples of the Diffraction of X-Rays*. Cornell University Press, 1967.

[18] A. Gerhardus. Entwicklung refraktiver röntgenlinsen für photonen bis 100 keV. Master's thesis, RWTH Aachen, 2001.

[19] E. Hecht and A. Zajac. *Optics*. Addison-Wesley Publishing Company, 2nd edition, 1987.

[20] B. Lengeler, J. Tümmler, A. Snigirev, I. Snigireva, and C. Raven. Transmission and gain of singly and doubly focusing refractive x-ray lenses. *Journal of Applied Physics*, 84(11):5855 – 5861, 1998.

[21] T. F. Günzler. Mikrotomographie mit hilfe refraktiver röntgenoptiken. Master's thesis, RWTH Aachen, 2000.

[22] R. L. Clough. High-energy radiation and polymers: A review of commercial processes and emerging applications. *Nuclear Instruments and Methods in Physics Research b*, 185:8 – 33, 2001.

[23] D. Widmann, H. Mader, and H. Friedrich. *Technologie hochintegrierter Schaltungen*. Springer-Verlag, Berlin, Heidelberg, New York, 1996.

[24] W. Chen and H. Ahmed. Fabrication of 5 – 7 nm wide etched lines in silicon using 100 keV electron-beam lithography and polymethylmethacrylate resist. *Applied Physics Letters*, 62(13):1499 – 1501, 1992.

[25] E. A. Dobisz, S. L. Brandow, R. Bass, and J. Mitterender. Effects of molecular properties on nanolithography in polymethyl methacrylate. *Journal of Vacuum Science & Technology B*, 18(1):107 – 111, 2000.

[26] P. M. Dentinger and J. W. Taylor. Quantification of the extent of reaction in a negative, novolac-based, chemically amplified resist. *Journal of Vacuum Science & Technology B*, 15(6):2632 – 2638, 1997.

[27] G. P. Watson, L. A . Fetter, and J. A. Liddle. Dose modification proximity effect correction scheme with inherent forward scattering corrections. *Journal of Vacuum Science & Technology B*, 15(6):2309 – 2312, 1997.

[28] K. Tsudaka, K. Furumi, H. Ohnuma, and H. Kawahira. Simulation-based automatic optical proximity effect correction adaptive for device fabrication. *Japanese Journal of Applied Physics*, 36:7477 – 7481, 1997.

[29] Homepage of Suss MicroTech, www.suss.com.

[30] H. J. Levinson and A. Arnold. Optical lithography. In *Handbook of Microlithography, Micromachining, and Microfabrication. Volume 1: Microlithography*, chapter 1. SPIE - The International Society for Optical Engineering, 1997.

[31] G. Simon, A. M. Haghiri-Gosnet, J. Bourneix, D. Decanini, Y. Chen, F. Rousseaux, H. Launois, and B. Vidal. Sub-20 nm x-ray lithography using conventional mask techologies on monochromatized syncrotron radiation. *Journal of Vacuum Science & Technology B*, 15(6):2489 – 2494, 1997.

[32] H. Guckel. LIGA and LIGA-like processing with high energy photons. *Microsystem Technologies*, 2:153 – 156, 1996.

[33] F. De Carlo, J. J. Song, and D. C. Mancini. Enhanced adhesion buffer layer for deep x-ray lithography using hard x-rays. *Journal of Vacuum Science and Technology B*, 16(6):3539 – 3542, 1998.

[34] E. W. Becker, W. Ehrfeld, P. Hagmann, A. Maner, and D. Münchmeyer. Fabrication of microstructures with high aspect ratios and great structural heights by synchrotron radiation lithography, galvanoforming, and plastic moulding (LIGA process). *Microelectronic Engineering*, 4:35 – 56, 1986.

[35] D. C. Flanders and H. I. Smith. Polyimide membrane x-ray lithography masks — fabrication and distortion measurements. *Journal of Vacuum Science & Technology*, 15(3):995 – 997, 1978.

[36] T. Ono and A. Ozawa. High contrast x-ray mask preparation. *Journal of Vacuum Science & Technology B*, 2(1):68 – 72, 1984.

[37] E. H. Anderson, D. P. Kern, and H. I. Smith. Fabrication by tri-level electron beam lithography of x-ray masks with 50 nm linewidths, and replication by x-ray nanolithography. *Microelectronic Engineering*, 6:541 – 546, 1987.

[38] G. J. Berry, J. A. Cairns, M. R. Davidson, D. R. G. Rodley, J. Thomson, I. C. E. Turcu, and W. Shaikh. 1 nm x-ray lithography using novel mask fabrication technique. *Review of Scientific Instruments*, 69(9):3350 – 3352, 1998.

[39] J. N. Randall and J. C. Wolfe. Preparation of x-ray lithography masks using a tungsten reactive ion etching process. *Applied Physics Letters*, 41(3):247 – 248, 1982.

[40] J. Klein, H. Guckel, D. P. Siddons, and E. D. Johnson. X-ray masks for very deep x-ray lithography. *Microsystem Technologies*, 4:70 – 73, 1998.

[41] H. Okuyama, Y. Hirata, and H. Takeda. Microfabrication of thick tungsten films for use as absorbers of deep x-ray lithography masks. *Microsystem Technologies*, 7:80 – 04, 2001.

[42] K. Fischer, B. Chaudhuri, E. Stiers, and H. Guckel. Large area, cost effective x-ray masks for high energy photons. *Microsystem Technologies*, 6:117 – 120, 2000.

[43] Homepage of Allresist GmbH: www.allresist.de.

[44] Y. Martin and H. K. Wickramasinghe. Toward accurate metrology with scanning force microscopies. *Journal of Vacuum Science & Technology B*, 13(6):2335 – 2339, 1995.

[45] K. Murata, M. Kotera, K. Nagami, and Namba S. Monte Carlo modeling of the photo and Auger electron production in x-ray lithography with synchrotron radiation. *IEEE Transactions on electron devices*, ED-32(9):1694 – 1703, 1985.

[46] K. Murata. Theoretical studies of the electron scattering effect on developed pattern profiles on x-ray lithography. *Journal of Applied Physics*, 57(2):575 – 580, 1985.

[47] H. Zumaqué, G. A. Kohring, and J. Hormes. Simulational studies of energy deposition and secondary processes in deep x-ray lithography. *Journal of Micromechanics and Microengineering*, 7:79 – 88, 1997.

[48] G. Feiertag, W. Ehrfeld, H. Lehr, A. Schmidt, and M. Schmidt. Calculation and experimental determination of the structure transfer accuracy in deep x-ray lithography. *Journal of Micromechanics and Microengineering*, 7:323 – 331, 1997.

[49] W. H. Press, S. A. Teukolsky, W. T. Vetterling, and B. P. Flannery. *Numerical Recipes in*. Cambridge University Press, 1992.

[50] R. Y. Rubinstein. *Simulation and the Monte Carlo Method*. John Wiley & Sons, New York, Chichester, Brisbane, Toronto, 1981.

[51] M. Schirmer, Allresist GmbH, priv. comm.

[52] T. E. Everhart and P. H. Hoff. Determination of kilovolt electron energy dissipation vs penetration distancen solid materials. *Journal of Applied Physics*, 42(13):5837 – 5846, 1971.

[53] C. T. Chantler. Theoretical form factor, attenuation, and scattering tabulation for z = 1 -92 from e = 1 - 10 eV to e = 0.4 - 1.0 MeV. *Journal of Physical and Chemical Reference Data*, 24:71, 1995.

[54] B. K. Agarwal. *X-Ray Spectroscopy*. Springer, Berlin, Heidelberg, 2nd edition, 1991.

[55] A. Zangwill. *Physics at Surfaces.* Cambridge University Press, 1988.

[56] H. Bethe. Zur Theorie des Durchgangs schneller Korpuskularstrahlen durch Materie. *Annalen der Physik*, 5:325 – 400, 1930.

[57] T. S. Rao-Sahib and D. B. Wittry. X-ray continuum from thick elemental targets for 10–50-keV electrons. *Journal of Applied Physics*, 45(11):5060 – 5068, 1974.

[58] K. Murata, T. Matsukawa, and R. Shimizu. Monte carlo calculations on electron scattering in a solid target. *Japanese Journal of Applied Physics*, 10(6):678 – 686, 1971.

[59] M. J. Berger and S. M. Seltzer. Studies in penetration of charged particles in matter. In *Nucl. Sci. Ser. Report No. 39, NAS-NCR Publ. No.1133*, volume 39, pages 205 – 268. Nat. Acad. Sci., Washington, 1964.

[60] M. O. Krause. Atomic radiative and radiationless yields for K and L shells. *Journal of Physical and Chemical Reference Data*, 8:303 – 327, 1979.

[61] J. A. Bearden. X-ray wavelengths. *Review of Modern Physics*, 39:78 – 124, 1967.

[62] B. Lengeler, C. G. Schroer, B. Benner, A. Gerhardus, T. F. Günzler, M. Kuhlmann, J. Meyer, and C. Zimprich. Parabolic refractive x-ray lenses. *Journal of Synchrotron Radiation*, 9:119 – 124, 2002.

[63] K. Murata, M. Yasuda, H. Kawata, and T. Matsuda. Effects of heavy atoms added into a resist on energy absorption in x-ray lithography. *Journal of Vacuum Science & Technology B*, 13(3):821 – 825, 1995.

Acknowledgements

I wish to acknowledge with gratitude

Prof. Dr. Lengeler, for the acceptance in the group and the opportunity to work on this interesting topic.

Prof. Dr. Lüth for undertaking the Koreferat and for the opportunity to use various equipment at the ISG.

the 'x-ray group': Christian Schroer for a lot of support and helpful discussions on anything and everything; Marion Kuhlmann for the superb lenses, the *Schnupperstudium* and a lot of active help; Boris Benner for the diffuser; Florian Günzler and Jannik Meyer for beam time sessions; Olga Kurapova for bringing order and flowers in our office and for carrying on the lithography project; and all the others (Johannes Tümmmler, Matthias Richwin, Achim Gerhardus, Fatima Frehse, Jens Patommel, Sebastian Feste, and Mario Schweitzer) for a great atmosphere.

the 'meso group': Thomas Hunger and Joachim Knoch for good times in our office and lots of discussions; Jörg Appenzeller, Heiko Stahl, Markus Jakob, and Hartmut Schittko for discussions and a lot of fun (Once upon a time ...).

our technical staff: Klaus Schäfer and Dieter Schulte for electronical bits and pieces; Mr. Roeger for his constructions; Martin Janus and Alexander Simons for many helping hands; Mr. Kordt and the rest of the mechanical workshop for their fast response to our emergencies.

our secretaries Ms. Weinkauf, Ms. Schüren, Ms. Dahl, and Ms. Zimmermann for their kindness and support.

Sven Achenbach of the FZ Karlsruhe for the masks, many helpful discussions, and an interesting beam time session.

our collegues from the FZ Jülich: Jürgen Stock and Alfred Fox for help and hospitality in the electroplating lab; Jürgen Moers and Thomas Schaepers for helpful discussions; the clean room staff from Jülich (A. Steffen, J. Müller, A. Pracht, M. Nonn) for a lot of support.

the ERSF group (A. Snigirev, I. Snigireva, A. Simionovici, C. Rau, and many others) for the possibility to perform the experiments and a steady support.

Mr. Schirmer of Allresist GmbH for many informative discussions about resist technology and an open mind for strange ideas.

Alex Henrici for the AFM.

Michael, Tanja, Tim, and the rest of the crowd for a lot of fun, exellent food, and for reminding me that there are quite a few worlds outside a physicist's lab.

last but not least, my familiy for their patience and their support.

and, of course, everybody and everything I forgot.

Curriculum Vitae

Name:	Christiane Zimprich
Date of Birth:	17.06.1972
Place of Birth:	Schwalmstadt, Germany

1978 – 1982	Attendance at the Grundschule Neukirchen/Knüll.
1982 – 1991	Attendance at the Melanchthon-Schule, Willingshausen-Steinatal.
June 1991	Allgemeine Hochschulreife school leaving examination)
1991 – 1997	Study of physics at the Philipps-Universität, Marburg/Lahn.
1996 – 1997	Diploma thesis at the Wissenschafliches Zentrum für Materialwissenschaften, Philipps-Universität, Marburg/Lahn.
September 1997	Diploma degree.
since January 1998	Ph.D. student and research staff member at the 2nd Institute of Physics at the RWTH Aachen.